Electronic structure of strongly correlated cerium intermetallics

Rafał Kurleto

Supervisor: dr. hab. Paweł Starowicz

Marian Smoluchowski Institute of Physics
Jagiellonian University in Kraków

This dissertation is submitted for the degree of Doctor of Philosophy

March 2020

Wydział Fizyki, Astronomii i Informatyki Stosowanej
Uniwersytet Jagielloński

Oświadczenie

Ja niżej podpisany Rafał Kurleto (nr indeksu: 1064992) doktorant Wydziału Fizyki, Astronomii i Informatyki Stosowanej Uniwersytetu Jagiellońskiego oświadczam, że przedłożona przeze mnie rozprawa doktorska pt. *Electronic structure of strongly correlated cerium intermetallics* jest oryginalna i przedstawia wyniki badań wykonanych przeze mnie osobiście, pod kierunkiem dra hab. Pawła Starowicza. Pracę napisałem samodzielnie.

Oświadczam, że moja rozprawa doktorska została opracowana zgodnie z Ustawą o prawie autorskim i prawach pokrewnych z dnia 4 lutego 1994 r. (Dziennik Ustaw 1994 nr 24 poz. 83 wraz z późniejszymi zmianami).

Jestem świadom, że niezgodność niniejszego oświadczenia z prawdą ujawnioną w dowolnym czasie, niezależnie od skutków prawnych wynikających z ww. ustawy, może spowodować unieważnienie stopnia nabytego na podstawie tej rozprawy.

Kraków, dnia .....

Rafał Kurleto

Acknowledgment

I would like to thank my supervisor dr. hab. Paweł Starowicz. He introduced me into a fascinating world of condensed matter physics and shared with me his broad experience concerning photoelectron spectroscopy.

I am also grateful to prof. dr. hab. Andrzej Szytuła for his help during my PhD studies and his valuable advice concerning data interpretation.

I would like to express my gratitude to prof. dr. hab. Józef Spałek for his support and objective analysis of obtained results.

The support of my parents, sister and brother should not be omitted. I am grateful to them for their patience and understanding during preparation of the thesis.

The help of dr. eng. Bogusław Penc and Marcin Rosmus, MSc. during experiments and data analysis is acknowledged. I am also grateful to dr. Maciej Fidrysiak for explanation of some theoretical aspects. I would like also to thank all my officemates for many interesting discussions, not always related to physics.

The support of the National Science Centre, Poland within the Grant no. 2016/23/N/ST3/02012 is acknowledged.

Abstract

Many cerium intermetallic compounds host such interesting states as heavy fermions, mixed valence, Kondo insulator and non Fermi liquid. Heavy fermions, which are a subject of investigation in a large part of the thesis, behave like quasiparticles with masses many times greater than the mass of a free electron. Such a strong renormalization of electron mass is evidenced i.a. in specific heat at low temperature. Indeed, the thermodynamic measurements can capture the subtle effects related to change of density of states in a close vicinity of the Fermi level. However, the description of fine features of the electronic structure close to the Fermi energy is still a demanding task for direct methods such as photoelectron spectroscopy. On the other hand, recent decades witness the tremendous development of angle resolved photoelectron spectroscopy.

The main aim of this thesis is to provide new insights on the physics of f electron systems. The new information about the hybridization between 4f electrons and conduction band is extracted from the photoelectron spectroscopy data obtained for different cerium compounds. The evolution of an electronic structure of $CeRhSb_{1-x}Sn_x$ system as a function of hole doping x observed in data collected by means of ultraviolet photoelectron spectroscopy without angular resolution (PES) seems to agree with the realization of quantum critical point in this system. Moreover, performed ab initio calculations suggest that hole doping induces a series of Lifshitz transitions in $CeRhSb_{1-x}Sn_x$. The $CeCu_9In_2$ compound appeared to be a new system, which displays Kondo lattice state. The hybridization effects have been studied thoroughly in the heavy fermion superconductor $CeCoIn_5$. The intrinsic image of hybridization between 4f electrons and conduction band carriers in momentum space has been extracted from the data obtained by angle-resolved photoelectron spectroscopy (ARPES) and verified with the aid of ab initio calculations and tight binding method. In case of Ce_3PdIn_{11}, which is also a heavy fermion superconductor, we provide the first ARPES measurements of the electronic structure. Moreover, consequences of presence of two independent Ce sublattices in this compound are analyzed. Using ab initio calculations we were able to identify features in electronic structure which appear due to the hybridization of conduction band carriers with particular Ce sublattices. In case of both compounds, $CeCoIn_5$ and Ce_3PdIn_{11}, a heavy fermion band at low temperature has been observed.

Streszczenie

W wielu międzymetalicznych związkach ceru występują tak interesujące stany, jak faza ciężkich fermionów, mieszana walencyjność, izolator Kondo i nielandauowska ciecz Fermiego. Materiały ciężkofermionowe, które są przedmiotem badań w znacznej części pracy, posiadają nośniki ładunku elektrycznego o masach wielokrotnie większych od masy swobodnego elektronu. Efekty tzw. renormalizacji masy są widoczne m.in. w cieple właciwym w niskich temperaturach. Pomiary termodynamiczny pozwalają na badanie zmian gęstości stanów w niewielkim obszarze przy energii Fermiego. Jednak, badanie subtelnych struktur w pasmach przy samej energii Fermiego jest ciągle poważnym wyzwaniem dla bezposrednich metod, takich jak spektroskopia fotoelektronów. Z drugiej strony, ostatnie dekady były czasem gwałtownego rozwoju metody kątoworozdzielczej spektroskopii fotoelektronów (ARPES).

Głównym celem niniejszej pracy jest dostarczenie nowych wyników, które będą stanowić wkład do rozwoju fizyki układów zawierających elektrony f. Nowe informacje dotyczące hybrydyzacji elektronów f z pasmem przewodnictwa uzyskiwane są z pomiarów metodą spektroskopii fotoelektronów dla różnych związków międzymetalicznych ceru. Ewolucja struktury pasmowej układu $CeRhSb_{1-x}Sn_x$ w funkcji domieszkowania dziurami x obserwowana za pomocą metody spektroskopii fotoelektronów bez rozdzielczości kątowej wydaje się być zgodna z realizacją kwantowego punktu krytycznego w układzie. Dodatkowo, wykonane obliczenia ab initio sugerują, że domieszkowanie dziurami indukuje serię przejść Lifszyca w $CeRhSb_{1-x}Sn_x$. W związku $CeCu_9In_2$ odkryto istnienie stanu sieci Kondo. W nadprzewodniku ciężkofermionowym $CeCoIn_5$ przeanalizowano efekty hybrydyzacji widoczne w strukturze pasmowej. Rzeczywisty obraz hybrydyzacji pomiędzy elektronami 4f a nośnikami z pasma przewodnictwa został wyznaczony z danych ARPES i zweryfikowany przy pomocy obliczeń ab initio i metody ciasnego wiązania. W przypadku związku Ce_3PdIn_{11}, który również jest nadprzewodnikiem ciężkofermionowym, wyznaczono po raz pierwszy strukturę elektronową tego układu. Dodatkowo, przeanalizowano konsekwencje obecności dwóch nierównoważnych podsieci atomów ceru w strukturze krystalicznej. Z pomocą obliczeń ab initio zidentyfikowano cechy struktury elektronowej pojawiające się w wyniku hybrydyzacji nośników z pasma przewodnictwa z poszczególnymi podsieciami Ce. W przypadku obu związków ($CeCoIn_5$, Ce_3PdIn_{11}) zaobserwowano pasmo ciężkofermionowe w niskich temperaturach.

Preface

The quantum description of electronic states in a periodic system is one of the most important issues of condensed matter physics. This formidable task involves taking into account a rich variety of forces acting on charge carriers trapped in a crystal lattice. Among them one can list the electron-electron interaction or coupling to the lattice vibrations. The successful attempt to solve this problem was made in 1929 by Felix Bloch (Bloch, 1929). Nowadays, the so called Bloch theory is an element of the paradigm in condensed matter physics. It provides the single particle description of an electronic structure of periodic systems. In this approach, the states of a system consisting of many electrons are represented by the states of one electron moving in a periodic potential originating from a rigid lattice and from the rest of electrons.

The great success of the single particle description based on Bloch theory and Fermi-Dirac statistics is testified by the perfect agreement with numbers of experiments. For example one can refer to the band structure of alkali or selected noble metals. However, there exists a class of materials with strong correlations in which the single particle description is not sufficient. Namely, these are systems in which the Coulomb energy dominates over the kinetic energy of electrons. In many cases, single particle description can be recovered by introduction of the notion of the quasiparticles. This genuine idea was coined by Lev Davidovich Landau in 1957 (Landau, 1956, 1957). The ground state of such many electron system, the Fermi liquid, and its collective excitations, are governed by the same rules as in the one particle description with the renormalized parameters. The systems which fall beyond the validity of the Fermi liquid theory are a subject of intense studies, nowadays.

The arrangement of electronic states of a given material is reflected in its physical properties. However, the most pronounced contribution comes from the states with the energy which is close to the Fermi energy. Indeed, specific heat can be related to the density of states at the Fermi level. Hence, the direct determination of the electronic structure in a close vicinity of the Fermi energy is of peculiar interest. One of the most direct method allowing studies of band structure is a photoemission spectroscopy. Its variation, angle-resolved photoemission spectroscopy (ARPES), is a powerful technique allowing for mapping of general overview of the electronic structure and to study subtle effects of collective excitations in crystalline materials. These last effects are reflected in the shape of the spectral function determined from photoemission experiment.

Recent decades show intensified interest in studies of electronic structure of correlated electron systems. Particular position, in such a class of materials, is occupied by intermetallic compounds of cerium. The complex orbital symmetry of Ce 4f electrons leads to many unusual phenomena reflected in anomalous behavior of physical properties. The electronic structure of cerium intermetallics is a result of the interplay between Kondo scattering (Kondo, 1964), indirect exchange Ruderman-Kittel-Kasuya-Yosida (RKKY) (Kasuya, 1956; Ruderman and Kittel, 1954) interaction and crystalline electric field. As a result, the complex magnetic phase diagrams are obtained. Among a variety of emerging states, one can list: Kondo lattice, mixed valency or Kondo insulators. The insight on the electronic structure of these unusual states of matter by means of photoemission spectroscopy is the primary goal of this work. Moreover, the correspondence between the electronic structure and physical properties is studied with application of specific heat and electrical resistivity measurements.

The structure of this thesis is following. This dissertation is divided into three parts. The first, introductory part, consists of four chapters. In the first chapter general description of properties of systems is provided. The second chapter deals with the theoretical description of these systems. The third chapter is devoted to discussion of crystal structures and physical properties of selected cerium intermetallics. The general ideas lying under the ab initio calculations are briefly sketched in the fourth chapter. The second part is an experimental section. It contains some theoretical aspects of the photoemission process, as well as, details of performed experiments (i.e. descriptions of experimental setups, etc.). The third part is devoted to obtained results. Each chapter of this section has a form of a preprint of article intended for publication in a journal (or already published article). The first chapter

of this part deals with the description of the Kondo lattice state in $CeCu_9In_2$ compound. These results are confronted with those available for isostructural $CeNi_9In_2$, which hosts a mixed valency state. The second chapter describes the evolution of the band structure in the $CeRhSb_{1-x}Sn_x$ as a function of relative content of Sn and Sb. The obtained results are interpreted in the light of quantum phase transition, which is encountered in the system at $x = 0.13$. The two subsequent chapters deal with the electronic structure of two heavy fermion superconductors from famous $Ce_nT_mIn_{3n+2m}$ family (T - transition metal). Namely, we have studied $CeCoIn_5$ and Ce_3PdIn_{11}. The fine structures of the spectral function related to low energy excitations originating from mixing between Ce 4f electrons and carriers from conduction band are collated with theoretical calculations based on tight binding approximation or density functional theory.

Bibliography

Bloch, F. (1929). *Z. Phys.*, 52(7-8):555 – 600.

Kasuya, T. (1956). *Prog. Theor. Phys.*, 16(1):45–57.

Kondo, J. (1964). *Prog. Theor. Phys.*, 32(1):37–49.

Landau, L. D. (1956). *J. Exptl. Theoret. Phys. (U.S.S.R.)*, 30:1058–1064.

Landau, L. D. (1957). *J. Exptl. Theoret. Phys. (U.S.S.R.)*, 32:59–60.

Ruderman, M. A. and Kittel, C. (1954). *Phys. Rev.*, 96:99–102.

Author's contribution to the published articles

The thesis consists of articles already published in scientific journals and preprints intended for publication. The list of already published papers with bibliographical information and description of contribution of the author of this dissertation is provided. The contribution to the results presented in chapters, which have not been published is also discussed.

1. ***Kondo lattice behavior observed in the $CeCu_9In_2$ compound***

   R. Kurleto, A. Szytuła, J. Goraus, S. Baran, Yu. Tyvanchuk, Ya. M. Kalychak, and P. Starowicz, Journal of Alloys and Compounds **803**, 576-584 (2019). doi: 10.1016/j.jallcom.2019.06.140

   The author of this thesis (R. K.) is the first author of the paper as well as the corresponding author together with his supervisor (P. S.). He performed the photoelectron spectroscopy measurements. His work involved also sample preparation prior to the electrical resistivity and specific heat measurement as well as the assistance during experiments. He analyzed obtained data and the results of theoretical calculations obtained by theoretician. The figures were prepared by him. He also wrote the first version of the manuscript and discussed the manuscript with coauthors.

2. ***Studies of Electronic Structure across a Quantum Phase Transition in $CeRhSb_{1-x}Sn_x$***

   R. Kurleto, J. Goraus, M. Rosmus, A. Ślebarski, and P. Starowicz, The European Physical Journal B **92**, 192 (2019). doi: 10.1140/epjb/e2019-100157-3

   R. K. performed photoelectron spectroscopy measurements with help of other coauthors. He also analyzed the experimental data and the result of theoretical calculations obtained by J. G. He prepared the first version of the manuscript and all figures. R. K. took part in the discussion of the manuscript.

3. ***Direct observation of f-electron hybridization effects in $CeCoIn_5$***

   R. Kurleto, M. Firysiak, L. Nicolaï, M. Rosmus, Ł. Walczak, A. Tejeda, K. Kissner, J. E. Rault, F. Bertran, D. Gnida, D. Kaczorowski, J. Minar, F. Reinert, J. Spałek, and P. Starowicz, intended for publication

   R. K. performed photoelectron spectroscopy measurements together with P. S., M. R., Ł. W., A. T., K. K., J. E. R., and F. B. He also oriented the samples (Laue x-ray diffraction) obtained by D. G. and D. K. He analyzed the experimental data and the theoretical results obtained by M. F., L. N., J. S. and J. M. He prepared the figures. The text was written by R. K. and P. S.

4. ***Electronic Structure of the Ce_3PdIn_{11} Heavy Fermion Compound Studied by Means of Angle-resolved Photoelectron Spectroscopy***

   R. Kurleto, M. Rosmus, L. Nicolaï, Ł. Walczak, A. Tejeda, D. Gnida, J. E. Rault, F. Bertran, D. Kaczorowski, J. Minar, and P. Starowicz, intended for publication

   R. K. performed photoelectron spectroscopy experiments together with P. S., M. R., Ł. W., A. T., J. E. R., and F. B. R. K. oriented the samples (Laue x-ray diffraction) obtained by D. G. and D. K. He performed data analysis. He also analyzed and discussed theoretical results obtained by L. N. and J. M. He prepared the figures, wrote the manuscript and consulted it with P. S.

Part I

Introduction

Chapter 1

Ce 4f electrons

Among all elements, the f-block of periodic table seems to be the most intriguing from the viewpoint of the electronic properties. The varying number of f electrons as a function of atomic number (Z) makes lanthanides and actinides an ideal playground in studies of many electron phenomena. The cerium, which is in center of interest of this work, is the lightest element from the f-block which has f electron. The configuration of atomic Ce is anomalous:

$$[^{58}\mathrm{Ce}] = [^{54}\mathrm{Xe}]4f^1 5d^1 6s^2,$$

the Madelung rule is not obeyed in this case (Kramida et al., 2018). It is proven, that in chemical reactions, firstly 6s and 5d electrons are conveyed into ionic bonding, resulting in pure f^1 valence configuration of Ce^{3+} ion (Kettle, 1996). High values of Z number suggest the significance of the relativistic effects for the elements from f-block of the periodic table. Indeed, the spin-orbit interaction has a crucial impact on electronic structure of Ce and its compounds. The ^{2}F spectroscopic (notation: $^{2S+1}\mathrm{L}_J$) term is split by this interaction into two multiplets: $^2\mathrm{F}_{5/2}$ and $^2\mathrm{F}_{7/2}$. The $^2\mathrm{F}_{5/2}$ is a ground state according to the Hund's rules. The complex structure of 4f orbital is reflected in constant charge density surfaces presented in the Fig. 1.1 together with 4f radial function [1]. As we can see the radial density of probability reaches zero exactly at the position of the center of mass (approximately at the position of the atomic nucleus) and has got a peak-like shape at some distance from nucleus. The behavior of f electron in Ce can resemble that encountered in systems with one electron in s valence shell, to some extent. One should have in mind, that orbitals presented in Fig. 1.1, are valid in case of spherical symmetry (e.g. free Ce^{3+} ion) or in case of octahedral symmetry (e.g. complexes of Ce with ligands in the octahedral bipiramid arrangement). The crystalline electric field influences the electronic structure of Ce^{3+} (Bauer and Rotter, 2009). Namely, the $^2\mathrm{F}_{5/2}$ is further split. In systems with cubic symmetry of the Ce sites the doublet-quartet configuration is obtained. Any other type of point symmetry of Ce^{3+} site results in configuration of energy levels which consists of three doublets. The Ce^{4+} configuration, is obtained by subsequent ionization, which is nonmagnetic in contrast to the former Ce^{3+}.

The usefulness of CEF theory is undeniable in systems with the permanent magnetic moments. However, the value of magnetic moment on Ce atom immersed in a solid is usually reduced. Thus, one should expect the behavior betwixt Ce^{3+} and Ce^{4+}.

It is noteworthy that the electronic properties of a system with Ce can be related with these in system to Ce changed by Yb (Kettle, 1996). The valence configuration of [Yb^{3+}] is $4f^{13}$, so instead of one electron occupying the 4f shell we deal with one hole. Hence, one may expect that physics of Yb systems is somehow related by a mirror symmetry with that of with Ce.

[1] Plots of orbitals adapted from internet portal: *https://chem.libretexts.org*

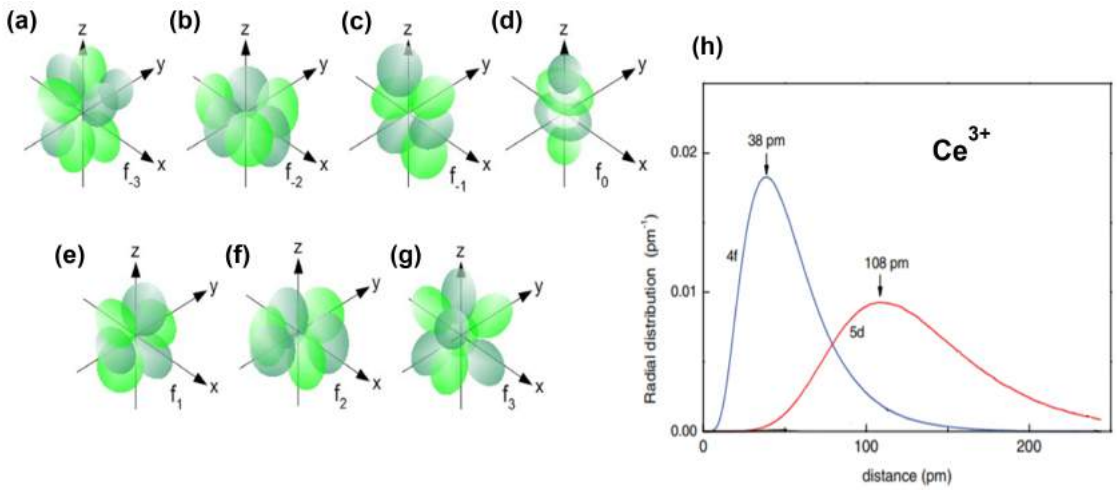

Figure 1.1: The atomic 4f orbitals (a)-(g) and 4f radial function (h) (Dorenbos, 2012). 4f radial function of Ce^{3+} ion is compared to 5d radial function.

The Kondo scattering is usually identified as a microscopic origin of quenching of local moments in cerium intermetallics (Matar, 2013; Stewart, 1984). A considerable mixing between f states and conduction band together with strong Coulomb repulsion between electrons on the f shell lead to ambiguous electronic configuration of Ce in a solid. Beyond a Kondo effect (Kondo, 1964), in systems with many sites occupied by Ce atom, the RKKY interaction is observed (Kasuya, 1956; Ruderman and Kittel, 1954). This is an indirect exchange interaction between magnetic moments at different vertices of a lattice mediated by carriers from conduction band. It supports a long range magnetic order. The ground state of the cerium intermetallic compound is interpreted as a result of the competition between two forces: Kondo scattering and RKKY interaction.

The intuitive description of the behavior of such systems is provided by means of so called Doniach diagram (Fig. 1.2), albeit it is intended only for one dimensional systems and does not represent exact solution of the problem (Doniach, 1977). The diagram provides the representation of the characteristic energies in coupling constant (J_{cf}) - temperature plane. The mutual ratio of the strength of Kondo and RKKY interaction can be tuned by f-c coupling constant (J_{cf}). The strength of RKKY exchange is represented by the characteristic temperature T_{RKKY} (red dotted line), while the strength of the Kondo scattering is given by the Kondo temperature T_K (blue dashed line). Beyond them, the Neel temperature as a function of temperature is plotted (black line). The Kondo temperature T_K is given by the equation:

$$T_K = We^{\frac{1}{D(\varepsilon_F)J_{cf}}}, \tag{1.1}$$

where $D(\varepsilon_F)$ denotes the density of states at the Fermi level and W is a width of conduction band. The formula describing T_{RKKY} is following:

$$T_{RKKY} \sim J_{cf}^2 D(\varepsilon_F) \tag{1.2}$$

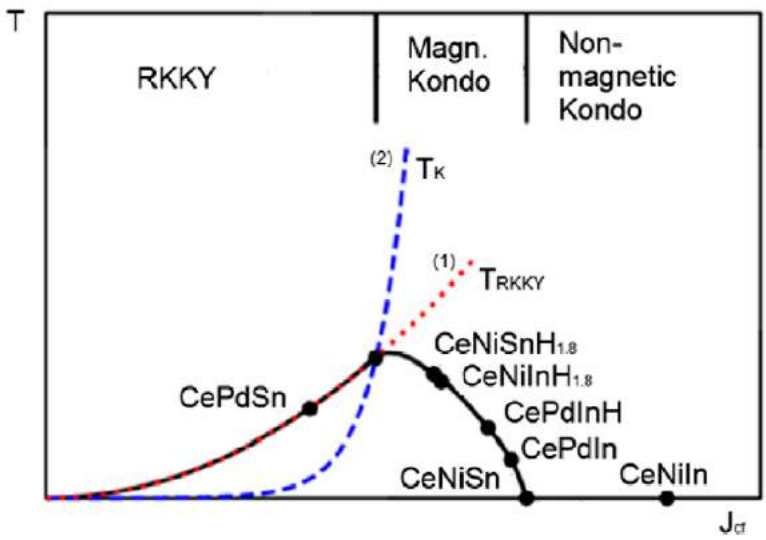

Figure 1.2: The schematic representation of the Doniach diagram. Taken from (Matar, 2013).

The region of the Doniach diagram between the Neel line and the horizontal axis represents antiferromagnetic state. In the region denoted as "RKKY" regime magnetic moments prevail at Ce atoms. This is a case of quite weak correlation with Curie-Weiss like behavior observed in a system. The point of the diagram at which the Neel temperature reaches 0 K (the point assigned to the CeNiSn compound) represents the quantum critical point (the instability of an antiferromagnetic phase at 0 K). The value of J_{cf} depends on the interatomic distances and the overlap between orbitals (Matar, 2013). Hence, several techniques exist which allow for manipulation in c-f coupling strength. The application of external pressure, in general, increases the value of J_{cf}. The value of J_{cf} can be reduced by expanding the unit cell, for example by "isoelectronic" substitution of element with greater atomic radius instead of that present in the structure (e.g. substitution of Pd in place of Ni) or by a hydrogenation. However, the influence of adsorbed H into a crystal structure of a host compound can be more complex, because H atom donates electron and can participate in a chemical bonding formation (Matar, 2013).

The Doniach phase diagram provides a good image of behavior of systems with Kondo-type interaction. However, in many cases it is insufficient to cover complexity of such systems. Thus, the extensions have been developed so far (Doradziński and Spałek, 1998). The idea of similarity between phase diagram of heavy fermions and cuprates or iron pnictides has been explored as well (Weng et al., 2016). Nowadays, it is believed that the proper description of systems with Kondo scattering is obtained by means of periodic Anderson model (Anderson, 1961). Thorough studies of such a model in a parameter space revealed different states. Among them, one can list: Kondo lattice[2], mixed valency, Kondo insulator state or heavy fermion superconductivity. The brief description of some of them is provided in subsequent sections.

[2]**Remark** The attention should be paid to the used nomenclature, which can be a source of ambiguity. The term "Kondo lattice" is often used (mainly by experimentalists) in order to describe a system in which the f sites cannot be treated independently. On the other hand, a paramagnetic solution of the Periodic Anderson Model which has Fermi liquid ground state is treated as a true "Kondo lattice" (mainly by theoreticians). Such a state is sometimes called a heavy fermion state in some works.

Bibliography

Anderson, P. W. (1961). *Phys. Rev.*, 124:41–53.

Bauer, E. and Rotter, M. (2009). *Magnetism of Complex Metallic Alloys: Crystalline Elelctric Field Effects*, pages 183–248. World Scientific.

Doniach, S. (1977). *Physica B & C*, 91:231–234.

Doradziński, R. and Spałek, J. (1998). *Phys. Rev. B*, 58:3293–3301.

Dorenbos, P. (2012). *ECS J. Solid State S. T.*, 2(2):R3001–R3011.

Kasuya, T. (1956). *Prog. Theor. Phys.*, 16(1):45–57.

Kettle, S. F. A. (1996). *f electron systems: the lanthanides and actinides*, pages 238–268. Springer Berlin Heidelberg.

Kondo, J. (1964). *Prog. Theor. Phys.*, 32(1):37–49.

Kramida, A., Yu. Ralchenko, Reader, J., and NIST ASD Team (2018). NIST Atomic Spectra Database (ver. 5.6.1), [Online]. Available: `https://physics.nist.gov/asd` [2019, May 4]. National Institute of Standards and Technology, Gaithersburg, MD.

Matar, S. F. (2013). *Prog. Solid State Ch.*, 41(3):55 – 85.

Ruderman, M. A. and Kittel, C. (1954). *Phys. Rev.*, 96:99–102.

Stewart, G. R. (1984). *Rev. Mod. Phys.*, 56:755–787.

Weng, Z. F., Smidman, M., Jiao, L., Lu, X., and Yuan, H. Q. (2016). *Rep. Prog. Phys.*, 79(9):094503.

Chapter 2

Kondo effect and heavy fermion physics

Anomalous properties of systems composed of magnetic atoms immersed in a nonmagnetic crystalline matrix have attracted attention in area of experimental studies as well as in theoretical modeling. Nowadays, it is believed that the broad range of physical phenomena in such systems is well covered within the scope of the Periodic Anderson Model (PAM). It describes the system in terms of the effective Coulomb repulsion between electrons on magnetic impurity shell (f or d shell, in this thesis we deal exclusively with f electron systems). However, solving of eigenproblem of PAM is a tremendous task (Hewson, 1993). Thus, simpler models, valid for some narrower range of phenomena have been developed. For example in case of small amount of magnetic atoms which are well separated from each other in diamagnetic matrix, one can use a single impurity Anderson model. Subsequently this model can be mapped for some subset of parameters on the *s-d* exchange model (a Kondo model). Here we would like to sketch some theoretical aspects of physical phenomena encountered in f - electron systems. Some intuitive description has been provided in the preceding section.

In case of one impurity with two internal degrees of freedom ($\sigma = \pm\frac{1}{2}$) the single impurity Anderson model (SIAM) is used (Anderson, 1961). The Hamiltonian has got a following form:

$$H_{SIAM} = \sum_{k,\sigma} \varepsilon_k n_{k\sigma} + \sum_{\sigma} \varepsilon_f n_{f\sigma} + U n_{f\uparrow} n_{f\downarrow} + \sum_{k,\sigma} \{V_{kf} c^{\dagger}_{k\sigma} f_{\sigma} + V^{\star}_{kf} f^{\dagger}_{\sigma} c_{k\sigma}\}, \tag{2.1}$$

where the first part denotes the energy of conduction band electrons, the second one is the energy of f shell, the third gives the Coulomb repulsive interaction with effective strength U. The last part describes the mixing between f level and conduction band with the V_{kf} strength. The standard second quantization notation is used: f_{σ} and $f^{\dagger}_{\sigma}$ are creation and annihilation operators for f electron with spin σ. Similarly: $c_{k\sigma}$ and $c^{\dagger}_{k\sigma}$ are creation and annihilation operators for a conduction band carrier with momentum k and spin σ. The electron number operators are: $n_{k\sigma}$ and $n_{f\sigma}$, for conduction band and f shell, respectively.

It turns out that the single impurity Anderson model (SIAM) in the limit of small mixing between conduction band with dispersion ε_k and the impurity level with energy ε_f is equivalent to the Kondo model. The effective Hamiltonian H_{eff} in such a regime is obtained by elimination of first order terms in V_{kf} in original hamiltonian (Schrieffer and Wolff, 1966). This is realized by application of a canonical transformation:

$$H_{eff} = e^{S} H e^{-S} \tag{2.2}$$

together with a condition:

$$[H_0, S] = H_1, \tag{2.3}$$

where H_0 is a hybridization independent part of H, H_1 represents the first order therm in V_{kf} and S is

a generator of transformation. The generator S has got a form:

$$S = \sum_{k,\sigma} V_{kf} \left(\frac{1}{\varepsilon_k - \varepsilon_f - U} n_{f,\bar{\sigma}} + \frac{1}{\varepsilon_k - \varepsilon_f} (1 - n_{f\bar{\sigma}}) \right) c^{\dagger}_{k\sigma} f_{\sigma} - h.c. \tag{2.4}$$

The spin dependent part of effective hamiltonian obtained by Schrieffer and Wolff, in a subspace with forbidden double occupancies of f shell is as follows:

$$H_{sd} = -\sum_{k,k'} J_{k,k'} (\Psi^{\dagger}_{k'} \vec{S} \Psi_k) \cdot (\Psi^{\dagger}_{f} \vec{S} \Psi_f), \tag{2.5}$$

where the field operators (Ψ_f and Ψ_k) have been introduced:

$$\Psi_k = \begin{pmatrix} c_{k,\uparrow} \\ c_{k,\downarrow} \end{pmatrix}, \qquad \Psi_f = \begin{pmatrix} f_{\uparrow} \\ f_{\downarrow} \end{pmatrix}.$$

The symbol $\vec{S}$ in equation (2.5) refers to spin operator $\vec{S} = \frac{\vec{\sigma}}{2}$ ($\vec{\sigma}$ is a column matrix composed of Pauli matrices). H_{sd} has got the similar form as in the model investigated by J. Kondo (Kondo, 1964). In general the *s-d* exchange coupling strength ($J_{kk'}$) is energy dependent what is visible in formula:

$$J_{kk'} = V_{k'f} V^{\star}_{kf} \left(\frac{1}{\varepsilon_k - \varepsilon_f - U} + \frac{1}{\varepsilon_{k'} - \varepsilon_f - U} - \frac{1}{\varepsilon_k - \varepsilon_f} - \frac{1}{\varepsilon_{k'} - \varepsilon_f} \right). \tag{2.6}$$

However, assuming that the dominating contribution comes from the excitations from vicinity of the Fermi surface (i.e. k, $k' \approx k_F$; k_F - Fermi wave vector) the strength of the $s-d$ exchange can be represented by the antiferromagnetic coupling constant:

$$J_{kk'} \approx J_0 = 2|V_{k_F f}|^2 \frac{U}{\varepsilon_f(\varepsilon_f + U)} \tag{2.7}$$

The *s-d* exchange model in slightly modified form than that presented in equation (2.5) has been introduced by J. Kondo in order to describe the anomalous behavior of low temperature electrical resistivity of a simple diamagnetic metal (eg. Au or Ag) which contains small amount of magnetic impurities (eg. Fe)(Kondo, 1964). His approach relied on perturbation theory (second order Born approximation). He showed that the part of electrical resistivity related to the scattering on the spin degrees of freedom is proportional to the logarithm of temperature. Hence, the total resistivity $\rho(T)$ can be described by the formula:

$$\rho(T) = \rho_0 + aT^5 + c\rho_1 \ln T, \tag{2.8}$$

where the term $\sim T^5$ represents the lattice contribution at low T and ρ_0 stands for the temperature independent part. The magnetic contribution is proportional to concentration of magnetic atoms (c), ρ_1 is some constant which is proportional to exchange integral J_0. One can check, that for antiferromagnetic coupling (viz. $J_0, \rho_1 < 0$) the function $\rho(T)$ displays a minimum at temperature T_{min}:

$$T_{min} = \left(\frac{-c\rho_1}{5a} \right)^{\frac{1}{5}}. \tag{2.9}$$

Such a minimum is a fingerprint of presence of Kondo effect in a metallic system. The remark on the behavior of $\rho(T)$ at very low temperature should be made. Namely, the formula (2.8) predicts the divergence of resistivity in the limit $T \to 0$ K, instead of experimentally observed saturation. Such a divergence is an artifact related to the breakdown of perturbation theory. Indeed, below some temperature (i.e. Kondo temperature T_K) the effective screening of magnetic moment by conduction electrons

is large and cannot be described perturbatively. The magnetic moment can be fully quenched. The antiferromagnetic interaction between conduction electrons and impurity spin results in a singlet and triplet many-body states. The first one is a ground state, while the second one has got energy by about U higher (U is a measure of strength of effective Coulomb repulsion on impurity shell). The singlet state is reflected in the narrow resonance peak at the Fermi energy in the spectral function (so called Kondo peak).

Exact solution of the Kondo problem can be obtained with the aid of numerical methods. However, some compact analytic formulas were proposed in order to provide approximate description of physical properties (Frota, 1992). It turns out that the Kondo resonance encountered in the spectral function as a result of formation of a singlet state can be modeled well by the simple formula for a density of states $D(\varepsilon)$ (ε - energy, here the Fermi energy is put to zero):

$$D(\varepsilon) = \frac{2}{\pi\Gamma_A}\mathrm{Re}\left(\frac{i\Gamma_K}{\varepsilon + i\Gamma_K}\right)^{\frac{1}{2}}, \tag{2.10}$$

where Γ_K is proportional to the Kondo temperature T_K and Γ_K parameter is related to the Friedel sum rule. The magnetic susceptibility $\chi(T)$ at low temperatures can be expressed as:

$$\chi(T) = \chi(0)\left(1 - \frac{\pi^2}{8}\frac{k_B^2 T^2}{\Gamma_K^2}\right), \tag{2.11}$$

with the susceptibility at 0 K equal to:

$$\chi(0) = \frac{g^2\mu_B^2}{\pi\Gamma_A}, \tag{2.12}$$

(g is the Lande magnetic factor, μ_B - the Bohr magneton). Similar dependency as for $\chi(T)$ is followed by electrical resistivity $\rho(T)$ at low temperature (here the reduced quantity is presented):

$$\frac{\rho(T) - \rho_0}{\rho(0) - \rho_0} = 1 - \frac{\pi^2}{8}\frac{k_B^2 T^2}{\Gamma_K^2}. \tag{2.13}$$

The coefficient $\rho(0)$ in equation (2.13) is a value of resistivity at 0 K, while ρ_0 is given by the formula:

$$\rho_0 = \frac{m}{n_0 e^2 \tau_0}, \tag{2.14}$$

where n_0 is density of conduction electrons, τ_0 is a relaxation time related to non-resonant scattering, m and e describe mass and charge of electron, respectively. The specific heat (c) calculated within this approach is linear at low T:

$$c = \frac{\pi}{3}\frac{k_B T}{\Gamma_K} \tag{2.15}$$

and the entropy (ΔS) related to the Kondo resonance is equal to:

$$\Delta S = k_B \ln 2, \tag{2.16}$$

which agree with the result of exact calculations. It is noteworthy, that expressions: (2.11), (2.13) and (2.15) are universal functions of T/Γ_K variable. One can calculate the so called Wilson ratio using the magnetic susceptibility and linear coefficient of specific heat at low T, i.e.:

$$R_W = \frac{3g^2\mu_B^2}{k_B\pi^2}\frac{C}{T\chi(0)} = \frac{\Gamma_A}{\Gamma_K}. \tag{2.17}$$

One obtains $R_W = 2$ after taking $\Gamma_A = 2\Gamma_K$. This result is consistent with that of Wilson (Wilson, 1975) renormalization group theory for a Kondo problem. In case of free electron gas one gets $R_W = 1$. Of course, the presented description of physical properties is not exact, because the temperature dependency of a Kondo resonance is not taken into account. However, good agreement with the exact results is expected at low temperature (for $T << T_K$).

The crucial experimental aspects of single ion Kondo effect, i.e. its scaling properties together with the resonance peak in spectral function, were described above within the simple theory provided by H. O. Frota. However, they are not preserved in case of dense Kondo system, i.e. this means that magnetic atoms cannot be treated as isolated impurities. The minimal variant of the Anderson model, which is able to capture main aspects of a Kondo lattice, can be expressed as:

$$H_{KL} = \sum_{k,\sigma} \varepsilon_k c^{\dagger}_{k\sigma} c_{k\sigma} + J_0 \sum_j \vec{S}_j \cdot (c^{\dagger}_{j\alpha} \vec{\sigma}_{\alpha\beta} c_{j\beta}), \tag{2.18}$$

where the first part is given in momentum ($\vec{k}$) space, while the second part is represented in real space, in distinction to equation (2.5), consists of summation over whole lattice of magnetic ions with spin $\vec{S}_j$. Indeed, the neighboring magnetic atoms can interact by the exchange mediated by conduction band electrons what is reflected in RKKY interaction, which can be derived from the model (2.18). Oscillating character of RKKY interaction is visible in its static spin polarization function ($\Pi(r)$), which can be presented in the form:

$$\Pi(r) \sim \frac{\sin(2k_F r) - 2k_F r \cdot \cos(2k_F r)}{k_F^4 r^4}, \tag{2.19}$$

where k_F denotes the Fermi wave vector and r is a distance from the arbitrary chosen lattice point. The presence of such oscillating interaction opens a possibility for magnetic order at low temperature. However, when the RKKY interaction does not dominate over Kondo demagnetization, the heavy fermion behavior is observed in the simplest case. In the diluted regime (Kondo regime), the Kondo scattering between f electrons and conduction band carriers occurs with random phases (the phase of the wave function of scattered electron was random). However, for a periodic arrangement of f orbitals the Bloch theorem must be fulfilled. As a result the Fermi liquid ground state emerges in the system. The resistivity at low temperatures drops rapidly as a consequence of coherence (Bloch state formation) and beyond the minimum, the maximum can be also observed. In such a case the system is paramagnetic and magnetic susceptibility obeys the simple Curie-Weiss behavior at high temperature, while at low temperature saturation is observed to the value of $\chi(0)$:

$$\chi(0) = g^2 \mu_B^2 \frac{D(\varepsilon_F)}{1 + F_0^a} \cdot \frac{m^\star}{m}, \tag{2.20}$$

where $m^\star$ is an effective mass of charge carrier, while F_o^a is a coefficient related to the strength of interaction between quasiparticles (Landau parameter). The specific heat is linear with Sommerfeld coefficient γ equal to:

$$\gamma = \frac{\pi^2 k_B^2}{3} \cdot \frac{m^\star}{m} \tag{2.21}$$

The Wilson ration defined in equation (2.17) is equal to:

$$R_W = 1 + F_o^a \tag{2.22}$$

and points directly to the strength of interaction between quasiparticles. Presence of heavy quasiparticle band with mostly f orbital character is another aspect of the heavy fermion state. Such a band has got a width of order of T_K and is developed at low temperature, namely below the coherence temperature (T_{coh}), which is another characteristic of the heavy fermion system. Thus, the f moments

participate in the Fermi surface at low T, while at above T_{coh} they are expelled from it. Hence, one should observe a significant change of the volume of the Fermi surface as a function of temperature, what is sometimes called as a Fermi surface collapse. The sketched scenario is the simplest one. Other more complex states can be encountered, as for example Kondo insulator state (eg. as in CeRhSb or $Ce_3Bi_4Pt_3$). In such systems the formation of the Kondo singlet is accompanied by the emergence of narrow gap in a band structure. Such a gap opens at low temperature due to mixing between f states and conduction band. The temperature evolution of the width of a gap is different that those encountered in the Bloch or Mott insulators.

The competition between RKKY interaction and Kondo scattering can be studied by means of alloying in a physical system (e.g. by substitution of magnetic elements in place of non-magnetic ones). It allows to observe the transition from the single impurity Kondo regime to the coherent Fermi liquid state (e.g. in $Ce_xLa_{1-x}Cu_6$). On the other hand it opens a possibility for studies of the magnetic instability at 0 K and the associated breakdown of Fermi liquid theory. There are several theoretical scenarios of such a quantum phase transition and the subject is still controversial up to know. In the vicinity of either, ferromagnetic or antiferromagnetic zero temperature instability, the ground state of many electron system is described in terms of the non Fermi liquid behavior (Coleman et al., 2001). The simple description of physical properties provided above for the Fermi liquid is not obeyed. The crucial observation is the fact, that in the quantum critical point, the mass renormalization factor diverges: $\frac{m^\star}{m} \to \infty$. This is reflected in the behavior of the specific heat at low temperature. Namely, in case of many systems with quantum critical point the specific heat evolves with the temperature according to the logarithmic law:

$$c(T) \sim T \ln\left(\frac{T_0}{T}\right), \tag{2.23}$$

where T_0 is some constant in units of temperature. The electrical resistivity follows the power law:

$$\rho \sim T^{1+\varepsilon} \tag{2.24}$$

with $0 < \varepsilon < 0.6$, instead of characteristic quadratic dependency observed for the Fermi liquid. The Curie-Weiss law describing the magnetic susceptibility is replaced by the formula:

$$\frac{1}{\chi(t)} = \frac{1}{\chi_0} + cT^a, \tag{2.25}$$

where the relation $a < 1$ was observed in experiments. The quantum phase transition is also visible in a dynamic susceptibility measured by inelastic neutron scattering measurements or in a hall coefficient R_H. The measurement of R_H as a function of a parameter which drives the quantum critical transition can be used in assessment of the realized scenario of the transition in a system.

Bibliography

Anderson, P. W. (1961). *Phys. Rev.*, 124:41–53.

Coleman, P., Pépin, C., Si, Q., and Ramazashvili, R. (2001). *J. Phys. Condens. Matter*, 13(35):R723–R738.

Frota, H. O. (1992). *Phys. Rev. B*, 45:1096–1099.

Hewson, A. C. (1993). *The Kondo Problem to Heavy Fermions*. Cambridge Studies in Magnetism. Cambridge University Press.

Kondo, J. (1964). *Prog. Theor. Phys.*, 32(1):37–49.

Schrieffer, J. R. and Wolff, P. A. (1966). *Phys. Rev.*, 149:491–492.

Wilson, K. G. (1975). *Rev. Mod. Phys.*, 47:773–840.

Chapter 3

Cerium intermetallics

The number of intermetallic compounds of cerium is huge and they display a rich variety of crystal structures. In the propounded thesis we do not even try to face up the problem of systematic description of these systems. However, in subsequent sections, we provide a brief description of selected representatives. The choice is dictated by the reference to the results presented in Part 3 and due to historical reasons. The brief description of the phase diagram of elemental Ce is provided at the beginning.

3.1 Metallic Ce - phase diagram

The pressure-temperature phase diagram for elemental Ce is quite complex (Fig. 3.1) (Schiwek et al., 2002). Usually the discussion of phase diagram is limited to five solid phases under a melting curve denoted as: α, α', β, γ, δ. The hexagonal β phase is the most stable at room temperature at ambient pressure conditions. However, both β and γ type structures can exist at room temperature at standard pressure. It should be mentioned that transition pressures and temperatures depend on the mechanical treatment and significant effects of hysteresis were observed. The bcc structure is encountered at high temperature in δ phase. The phase diagram displays two fcc phases: γ and α, in neighborhood of β phase. The high pressure phase is an α phase. The isostructural transition from γ to α Ce, encountered at about 8 kbar at room temperature, is accompanied by the volume collapse of order of 15% (Allen and Martin, 1982). It is believed that the main driving force of the transition is a delocalization of 4f electrons due to the presence of Kondo effect. The monoclinic α'' (C2/m space group) and orthorombic α' (Cmcm space group) phases are also present. Beyond them, the bct-type (body centered tetragonal) ε phase exists under high pressure (>7 GPa).

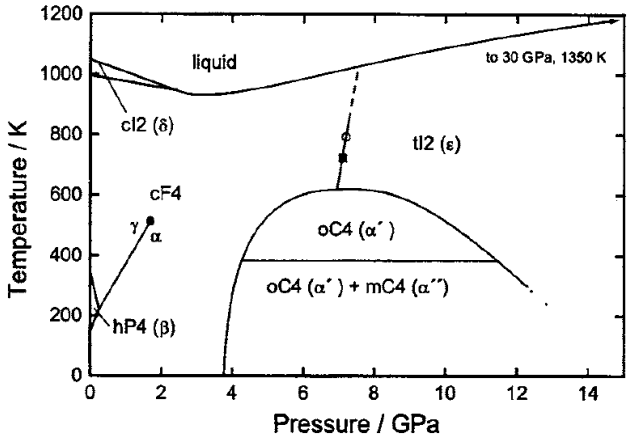

Figure 3.1: Phase diagram of cerium. Symmetry of the system is indicated by Pearson space group symbols. Taken from (Schiwek et al., 2002).

The γ phase displays the Curie-Weiss-like magnetism characteristic of a presence of local moments (Hamlin, 2015). The cerium in the collapsed α phase is a Pauli-paramagnetic metal, characterized by large value of magnetic susceptibility. A superconducting state with T_c lower than 0.05 K at pressure of 2 GPa emerges in this phase. Above 5 GPa the superconductivity in the α' phase below 1.7 K was also observed (Wittig, 1968). The decrease of the pressure from 5 GPa to 3.6 GPa leads to increase in T_c to 1.9 K (Loa et al., 2012). However, there is no conclusive information which phase is characterized by that number, both α' and α'' should be considered.

3.2 RT_9In_2 compounds

Ternary indidies from R-T-In (R - rare earth element, T - transition metal) system display many interesting properties from the viewpoint of crystal chemistry and physics. Beyond the possibility of studies of crucial issues of condensed matter physics (e.g. heavy fermion physics, unconventional superconductivity, etc.), they can be considered as promising materials for hydrogen storage (Kalychak et al., 2004).

Among the whole family of R-T-In compounds, intermetallics crystallizing in tetragonal structure of YNi_9In_2-type (space group: P4/mbm) draw particular attention (Kalychak et al., 2004). The YNi_9In_2-type structure is an ordered superstructure of $CeMn_6Ni_5$-type structure (Fig. 3.2). The high coordination numbers are typical of this structure. Each rare earth atom has got 22 nearest neighbors, while 15 and 12 atoms surround each In and Ni (transition metal site) atom, respectively (Bigun et al., 2013). The arrangement of Ni and In atoms can be considered as the 3D Ni_9In_2-net with channels along c-axis which are filled by rare earth atoms. A strong bond between indium atoms is testified by very low distance between them in all known representatives.

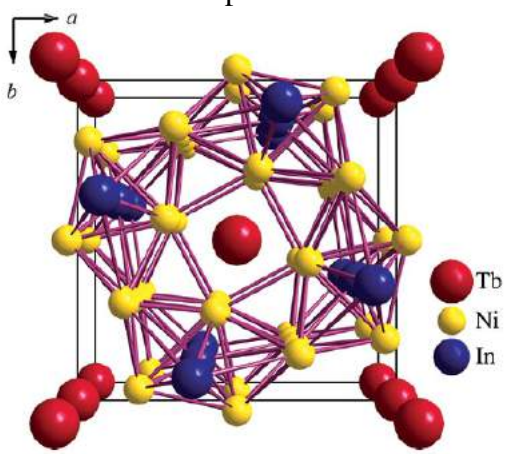

Figure 3.2: The structure of $TbNi_9In_2$ with visible Ni_9In_2 3D net filled by Ce atoms. Taken from (Bigun et al., 2014).

So far, magnetic properties of RCu_9In_2 and RNi_9In_2 systems have been studied thoroughly (Baran et al., 2016; Bigun et al., 2014). $LaCu_9In_2$, $LaNi_9In_2$ and YNi_9In_2 are Pauli-paramagnetic metals without f electrons. Magnetism of $PrNi_9In_2$ and $NdNi_9In_2$ as well as of their Cu counterparts is dominated by Curie-Weiss-like behavior between 20 and 300 K. The obtained values of paramagnetic Curie-Weiss temperature (θ_p) are negative. This suggests the presence of antiferromagnetism in the system. For $PrNi_9In_2$, $PrCu_9In_2$ and $NdNi_9In_2$ the phase transition was not encountered down to 2 K. In case of $NdCu_9In_2$, the metamagnetic transition was observed at temperature equal to 4.3 K. In case of $EuNi_9In_2$ there is no conclusive information, if either ferromagnetic order or intermediate valency state is realized. The interpretation of the data for $EuCu_9In_2$ is also not clear, although the

antiferromagnetic ground state is anticipated. It is noteworthy, that RT_9In_2 compounds with T=Cu are more prone to exhibit magnetic order at low temperature than these with Ni.

Known representatives of CeT_9In_2 display fingerprints of heavy fermion physics. $CeNi_9In_2$ is considered as a realization of mixed valence state (Kurleto et al., 2015; Moze et al., 1995; Szytuła et al., 2014; Tran et al., 2020), while the presence of the coherent Kondo lattice phase in $CeCu_9In_2$ is discussed further in the text of this thesis. The substitution of Cu in the place of Ni in $CeNi_9In_2$ leads to significant change in electronic structure, what can be explained as follows. The electronic configuration of Cu atom is [Ar] $3d^{10}$ $4s^1$, while for Ni we have [Ar] $3d^8$ $4s^2$. Thus, 3d electrons in Cu form a closed shell. The maximum of the Cu 3d density of states is expected to locate well below the Fermi level. Hence, one can expect that mixing between f level and 3d shell is suppressed and coupling between 4s and 4f levels is dominating. On the contrary, in case of Ni the 3d-4f mixing is considered as dominating, because of suspected large density of states at the Fermi level. Additionally, the lattice parameters of $CeNi_9In_2$ are smaller than in case of its counterpart with Cu. This is in line with the smaller atomic radius of Ni than that of Cu. Therefore, the higher inter-atomic distances in $CeCu_9In_2$ result in weaker overlap between Ce 4f states with the states originating from other atoms. As a consequence valence fluctuations are suppressed, while the strength of exchange interaction is not affected significantly (the strength of RKKY interaction is proportional to J_{cf}^2, while the strength of Kondo scattering is given by exponential function of J_{cf}). This reasoning should also apply in the case of the rest of RT_9In_2 compounds with light lanthanides.

3.3 CeTX compounds

The ternary equiatomic CeTX (T - transition metal, X - element from p-block of the periodic table) compounds are considered as the largest family of cerium intermetallics. The great interest in this systems can be explained by the rich variety of phenomena related to presence of f electrons e.g.: valence fluctuations, Kondo insulating state or quantum phase transitions. Representatives of CeTX family crystallize in orthorombic or hexagonal structures which are superstructures of a simple AlB_2-type structure (Matar, 2013). Here, we would like to focus mainly on ternary stannides and ternary antimonides. The magnetic and transport compounds of representatives of this subfamilies are very interesting. The compounds: CeCuSn, CeAgSn, CePdSn (Ślebarski et al., 2001), CePtSn (Matar, 2013) exhibits antiferromagnetism at low temperature. The ferromagnetic state was observed in: CePdSb, CePtSb and CeAuSn. CeRhSb and CeNiSn are Kondo insulators. Partial substitution of Sn in a position of Sb in CeRhSb results in solid solution $CeRhSb_{1-x}Sn_x$ ($0<x<0.2$) and induces the transition from the Kondo insulator to the non Fermi liquid (Janka et al., 2016; Ślebarski and Spałek, 2005; Spałek et al., 2005). The $CeRhSb_{1-x}Sn_x$ crystallizes in orthorombic ε-TiNiSi-type structure (space group: Pnma) for $0<x<0.2$. For $0.2<x<0.8$ the system is a mixture of CeRhSb and CeRhSn. The hegaxonal ZrNiAl-type (space group: P62) is observed for $0.2<x<1.0$. The common feature of many CeTX compounds is an existence of polyanionic network in the crystal structure. The cerium atom is strongly electropositive and the negative charge is partially transferred to the T and X atoms (Pöttgen, 2006), which are arranged in a 2D (e.g. CeAuSn) or 3D net (e.g. CeRhSn, CeRhSb). Indeed, the 3D RhSb net is present in $CeRhSb_{1-x}Sn_x$ (Chevalier et al., 2007). This network creates the channels, which are filled with Ce atoms. In case of ε-TiNiSi-type structure, each channel contains two Ce chains, while in case of ZrNiAl-type structure there is only one Ce chain inside each channel.

Figure 3.3: Common structures of CeTX compounds (X=Sb, Sn). The 3D TX networks characteristic of CeRhSb and CePtSn (a) or CeRhSn (b) and 2D network realized in case of CeAuSn (c). Gray circles denote Ce atoms. Empty circles stand for p-element, while the black ones are for transition metal. Adapted from (Pöttgen, 2006).

The quantum critical point is encountered in $CeRhSb_{1-x}Sn_x$ at x=0.13 (Ślebarski and Spałek, 2005). It is manifested by a singular behavior of physical properties, e.g. magnetic susceptibility. The critical behavior arises probably due to the change of carrier concentrations, the Sn substitution is equivalent to the hole doping. The scaling law between magnetic susceptibility (χ) and electrical resistivity (ρ):

$$\rho \cdot \chi = \text{const},$$

is obeyed in the Kondo insulator state (i.e. for $x < 0.13$). The CeRhSn compound hosts the Griffiths phase which arises as a result of valence instability of f shell in presence of atomic disorder (Ślebarski et al., 2002).

3.4 $Ce_nT_mIn_{3n+2m}$ family

The $Ce_nT_mIn_{3n+2m}$ (T - transition metal) family of cerium intermetallics has been a subject of extensive studies, so far. It provides a natural platform for studies of many body physics in reduced (spatial) dimensions (close to the quantum critical point) (Shimozawa et al., 2016), what can be one reason for such a great interest.

The parent compound (m=0, n=∞) is a heavy fermion $CeIn_3$ which crystallizes in a simple cubic structure ($AuCu_3$ type unit cell). It exhibits antiferromagnetic ordering below Neel temperature equal to 10.1 K. The pressure-temperature phase diagram of such a system has been thoroughly studied (Lengyel, 2008). It reveals superconducting dome. The maximum T_C equal to about 0.25 K is displayed at the external pressure of 2.6 GPa. Beyond the antiferromagnetic and superconducting phase the non Fermi liquid formation is encountered in pressure-temperature phase diagram.

The representatives of the described family with more complicated structures are build from $CeIn_3$ and TIn_2 ($PtHg_2$-type) blocks. Namely, in general the unit cell of $Ce_nT_mIn_{3n+2m}$ consists of n layers of $CeIn_3$ stacked along c axis, which alternate with m layers of TIn_2. The symmetry of the system is tetragonal for all representatives apart from parental $CeIn_3$. The m layers of TIn_2 can be treated as spacers separating the Ce-In planes. Thus, the anisotropy can be controlled by the change in m and n parameters. Therefore, some analogy with the cuprates can be sketched. For $m = n = 1$ the unit cell is of $HoCoGa_5$ type, while for $n = 2$ and $m = 1$ (i.e. for Ce_2TIn_8) it has got Ho_2CoGa_8-type. In case of $n = 3$ and $m = 1$ Ce_3PdIn_{11}-type structure is observed. The space group of mentioned systems is P4/mmm. However, it is not the case of all $Ce_nT_mIn_{3n+2m}$ compounds, because space group of $CePt_2In_7$ is I4/mmm. It is noteworthy that, rare earth element occupies only one site (2g) in case of Ho_2CoGa_8 and $HoCoGa_5$-type structures, while in Ce_3PdIn_{11} two independent positions of Ce are

encountered (2g, 1a). This fact is reflected in physical properties and can be linkeed with possible interplay between two Kondo scales in the system.

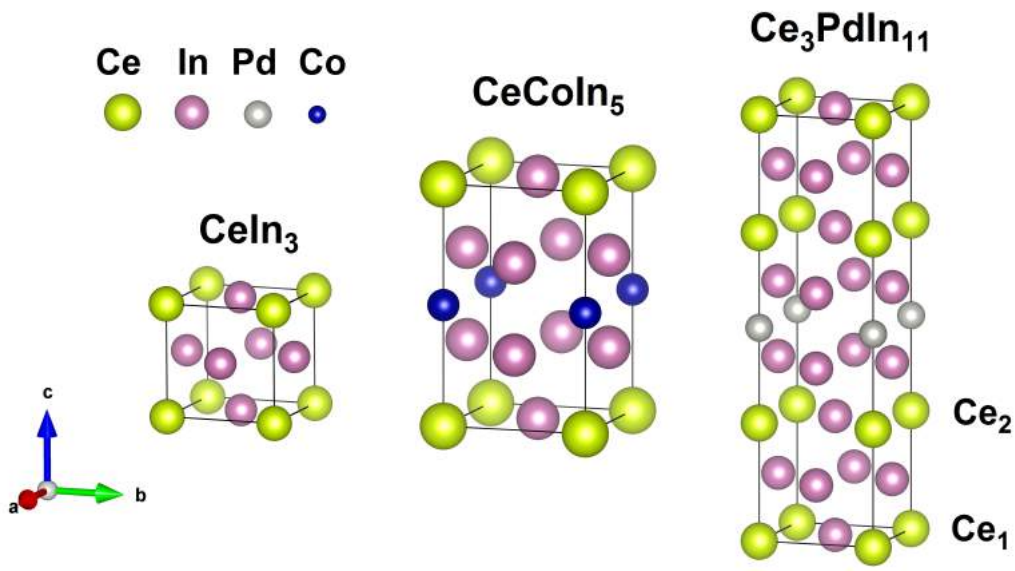

Figure 3.4: Crystal structure of representatives of $Ce_nT_mIn_{3n+2m}$ family. Two independent position of Ce atoms are marked in case of Ce_3PdIn_{11}. Symbols Ce_1 and Ce_2 correspond to Ce 1a and Ce 2g sites, respectively.

The relations between crystal structures of representatives of $Ce_nT_mIn_{3n+2m}$ family to their building blocks can be schematically written in a form of following "equations":

$$Ce_nT_mIn_{3n+2m} = n \times CeIn_3 + m \times TIn_2$$
$$3\times CeIn_3 + PdIn_2 = Ce_3PdIn_{11}$$
$$CeCoIn_5 = 1\times CeIn_3 + 1\times CoIn_2$$
$$Ce_2PdIn_8 = 2\times CeIn_3 + 1\times PdIn_2.$$

Some theoretical results (Haga et al., 2001)] based on density functional theory (DFT) suggest that conductivity of $CeIn_3$ layer is greater than that of TIn_2. Therefore, the electronic structure of $Ce_nT_mIn_{3n+2m}$ should have some two-dimensional features related to Ce-In planes, which are to some extent separated from the rest of a system. Among $CeTIn_5$, Ce_3PdIn_{11} and Ce_2TIn_8, $CeTIn_5$ subfamily seems to be the closest to 2D system. In this case, the Ce-In planes are better separated from themselves than in the two other subfamilies. On the other hand, experimental results point mainly to 3D character of the system, albeit some 2D features were identified (Koitzsch et al., 2013). Pronounced effects of isoelectronic substitution in transition metal site for $CeTIn_5$ compounds were observed. The heavy fermion compound $CeCoIn_5$ turns out to be an ambient pressure superconductor with T_c equal to 2.3 K. It has the highest T_c among Ce based heavy fermion compounds, according to the knowledge of the author. The highest observed T_c among the whole class of heavy fermions belongs to the radioactive $PuCoIn_5$. Similarly as for $CeCoIn_5$, the heavy fermion $CeIrIn_5$ displays the transition to the superconducting state at T_c equal to 0.4 K at ambient pressure. However, $CeRhIn_5$ displays antiferromagnetic ordering below Neel temperature equal to 3.8 K. The superconducting state appears in this compound under application of hydrostatic pressure equal to at least 15 kbar. Distinctiveness of physical properties of $CeTIn_5$ compounds representing isoelectronic substitution has to be related to the significant differences in electronic structure, especially close to the Fermi level, as well as reflects the importance of quantum fluctuations.

Indeed, the $CeCoIn_5$ system lies on the verge of the magnetic instability what was proven by studies of physical properties of $CeCo(In_{1-x}Cd_x)_5$ system (Pham et al., 2006). The partial substitution of Cd in place of In seems to play a role of negative pressure (p electrons are removed from the system with almost unchanged unit cell volume). The small substitution (about 5%) induces the antiferromagnetic order at low temperature. Thus the external hydrostatic pressure cannot be used in order to induce AFM phase. The physics of $CeCoIn_5$ turns out to follow the behavior of $CeRhIn_5$ at high pressure. Indeed, variation of T_c as a function of pressure reproduces that for $CeCoIn_5$ at pressures lower by 1.6 GPa ($CeCoIn_5$=$CeRhIn_5$@1.6 GPa). The normal state of $CeCoIn_5$ (i.e. non-superconducting) displays significant deviations from the Fermi liquid theory. Among them, one can list the linear dependency of the resistivity near T_c, logarithmic divergence of c/T, and divergent magnetic susceptibility at low temperature. The standard Fermi liquid properties are observed after application of external pressure. The application of external magnetic field plays a similar role. However, beyond the Fermi liquid state, the FFLO phase or/and incommensurate AFM state are expected at high magnetic fields. The superconducting phase of $CeCoIn_5$ is believed to emerge as a result of pairing of heavy quasiparticles in a spin-singlet state. Experiments point to $d_{x^2-y^2}$ gap symmetry.

The rich phase diagram is also expected for Ce_3PdIn_{11}. As it was mentioned above, the crystal structure of this compound is characterized by the presence of two inequivalent Ce sublattices. Different local chemical environment of Ce ions can be reflected in different strength of Kondo scattering. Indeed, the interplay between the Kondo interaction in both sublattices, when respective coupling constants are significantly different, changes generally the original phase diagram for a dense Kondo system provided by Doniach (Benlagra et al., 2011). The system is characterized by two Kondo temperatures: T_1 and T_2, which are related to the independent sublattices, and the coherence temperature T_{coh} ($T_{coh} < T_2 < T_1$). Below T_{coh} the Fermi liquid theory is obeyed, while for $T_2 < T < T_1$ the partial screening is observed. If the intersite exchange interaction is sufficiently large, AFM phase emerges. In partially screened magnetic phase, the sublattice associated with smaller Kondo temperature T_2 is magnetically ordered, while the magnetic moments in the second sublattice are well screened and carriers give rise to a heavy fermion band. The subsequent increase in strength of the RKKY interaction induces the magnetic order in the second sublattice. It is noteworthy, that the arrangements of magnetic moments in both sublattices can be different. Hence, the multiple phase transitions, within the AFM phase, are expected. In fact, such a scenario was proven experimentally (Das et al., 2019; Kratochvilova et al., 2015). The magnetic order appears in Ce_3PdIn_{11} below 1.68 K and the second phase transition within AFM phase was encountered at 1.56 K. Below T_c equal to 0.58 K the system undergoes the transition to the superconducting state. Similarly as in the case of $CeCoIn_5$ the Cooper pairs are believed to arise from heavy quasiparticles, although the pairing symmetry has not been established so far. Significant mass enhancement is predicted for charge carriers in Ce_3PdIn_{11} on the basis of specific heat measurements. However, it is difficult to provide conclusive value of Sommerfeld coefficient using results obtained so far. The Kondo temperature averaged over independent Ce sublattices is estimated as 12 K (Kratochvilova et al., 2015).

Bibliography

Allen, J. W. and Martin, R. M. (1982). *Phys. Rev. Lett.*, 49:1106–1110.

Baran, S., Przewoźnik, J., Kalychak, Ya. M., Tyvanchuk, Yu., and Szytuła, A. (2016). *J. Magn. Magn. Mater.*, 410:156–164.

Benlagra, A., Fritz, L., and Vojta, M. (2011). *Phys. Rev. B*, 84:075126.

Bigun, I., Dzevenko, M., Havela, L., and Kalychak, Ya. M. (2013). In *Solid Compounds of Transition Elements II*, volume 194 of *Solid State Phenomena*, pages 45–49. Trans Tech Publications.

Bigun, I., Dzevenko, M., Havela, L., and Kalychak, Ya. M. (2014). *Eur. J. Inorg. Chem.*, 16:2631–2642.

Chevalier, B., Decourt, R., Heying, B., Schappacher, F. M., Rodewald, U. C., Hoffmann, R.-D., Pöttgen, R., Eger, R., and Simon, A. (2007). *Chem. Mater.*, 19(1):28–35.

Das, D., Gnida, D., and Kaczorowski, D. (2019). *Phys. Rev. B*, 99:054425.

Haga, Y., Inada, Y., Harima, H., Oikawa, K., Murakawa, M., Nakawaki, H., Tokiwa, Y., Aoki, D., Shishido, H., Ikeda, S., Watanabe, N., and Ōnuki, Y. (2001). *Phys. Rev. B*, 63:060503.

Hamlin, J. (2015). *Physica C*, 514:59 – 76.

Janka, O., Niehaus, O., Pöttgen, R., and Chevalier, B. (2016). *Z. Naturforsch. B*, 71(7):737–764.

Kalychak, Y. M., Zaremba, V. I., Pöttgen, R., Lukachuk, M., and Hoffmann, R.-D. (2004). Rare earth-transition metal-indides. volume 34 of *Handbook on the Physics and Chemistry of Rare Earths*, pages 1–133. Elsevier.

Koitzsch, A., Kim, T. K., Treske, U., Knupfer, M., Büchner, B., Richter, M., Opahle, I., Follath, R., Bauer, E. D., and Sarrao, J. L. (2013). *Phys. Rev. B*, 88:035124.

Kratochvilova, M., Prokleska, J., Uhlirova, K., Tkac, V., Dusek, M., Sechovsky, V., and Custers, J. (2015). *Sci. Rep.*, 5:15904.

Kurleto, R., Starowicz, P., Goraus, J., Baran, S., Tyvanchuk, Yu., Kalychak, Ya. M., and Szytuła, A. (2015). *Solid State Commun.*, 206:46–50.

Lengyel, E. (2008). *Antiferromagnetism and Superconductivity in Ce-based Heavy-Fermion Systems*. Cuvillier Verlag.

Loa, I., Isaev, E. I., McMahon, M. I., Kim, D. Y., Johansson, B., Bosak, A., and Krisch, M. (2012). *Phys. Rev. Lett.*, 108:045502.

Matar, S. F. (2013). *Prog. Solid State Ch.*, 41(3):55 – 85.

Moze, O., Mentink, S., Nieuwenhuys, G., and Buschow, K. (1995). *J. Magn. Magn. Mater.*, 150(3):345–348.

Pham, L. D., Park, T., Maquilon, S., Thompson, J. D., and Fisk, Z. (2006). *Phys. Rev. Lett.*, 97:056404.

Pöttgen, R. (2006). *Z. Naturforsch. B*, 61(6):677–698.

Schiwek, A., Porsch, F., and Holzapfel, W. B. (2002). *High Pressure Res.*, 22(2):407–410.

Shimozawa, M., Goh, S. K., Shibauchi, T., and Matsuda, Y. (2016). From kondo lattices to kondo superlattices. *Rep. Prog. Phys.*, 79(7):074503.

Ślebarski, A., Bauer, E. D., Li, S., Maple, M. B., and Jezierski, A. (2001). *Phys. Rev. B*, 63:125126.

Ślebarski, A., Maple, M. B., Freeman, E. J., Sirvent, C., Radłowska, M., Jezierski, A., Granado, E., Huang, Q., and Lynn, J. W. (2002). *Philos. Mag. B*, 82(8):943–961.

Ślebarski, A. and Spałek, J. (2005). *Phys. Rev. Lett.*, 95:046402.

Spałek, J., Ślebarski, A., Goraus, J., Spałek, L., Tomala, K., Zarzycki, A., and Hackemer, A. (2005). *Phys. Rev. B*, 72:155112.

Szytuła, A., Baran, S., Penc, B., Przewoźnik, J., Winiarski, A., Tyvanchuk, Yu., and Kalychak, Ya. M. (2014). *J. Alloy. Compd.*, 589:622–627.

Tran, V., Skokowski, P., Sahakyan, M., and Szytuła, A. (2020). *J. Solid State Chem.*, 284:121135.

Wittig, J. (1968). *Phys. Rev. Lett.*, 21:1250–1252.

Chapter 4

Ab initio band structure calculations

The establishment of non-relativistic electronic structure of hydrogen atom was the cornerstone of modern physics. The Schrodinger equation describing the dynamics of a system composed of nucleus and one electron can be solved exactly. The elegant mathematical formalism gives compact formulas which describe the eigenenergies as well as wave functions. However, such description cannot be easily extended to systems with many electrons. The plethora of approximated methods have been developed, so far. The particular attention should be paid to the family of methods based on the concept of the self-consistent field. The methods arise from the idea, that the original problem can be mapped on the problem of motion of one electron in some field. Such a field is represented by a potential resulting from the interaction with nuclei and a rest of electrons. The approach employing this method together with the variational principle today is known as the Hartree-Fock method and was applied successfully to the helium atom (i.e. system with 2 electrons).

The main quest in the field of determination of an electronic structure of systems of many electrons is to provide a feasible method accounting for fermion character of electrons. The two fundamental issues should be addressed (Matar, 2013). Firstly, the Pauli exclusion principle should be taken into account, what imposes constrains on the symmetry of the full wave function (i.e. involving the spin). The effect of this rule can be illustrated by the so called ”Fermi hole”. Let's assume that the electron with the up spin is located at some point of the space. Then, the probability of finding of another electron with the up spin must be reduced in the vicinity of the first particle. The second aspect is a Coulomb interaction between electrons, which can be depicted by the so called ”correlation hole”. Let's recall the example mentioned above. The density of probability for the electron with down spin should be also reduced, due to strong Coulomb repulsion. The effect of correlation is not properly included in original Hartree-Fock method.

The Hartree-Fock method and its extensions taking into account the correlation effects turned out to be difficult in case of many electron systems. The techniques treating the electron density as a crucial variable and allowing for convenient determination of electronic structure have been developed in second half of the last century. However, the idea of employing electron density had been introduced before (i.e. Thomas-Fermi model) (Landau and Lifshitz, 2001) in order to describe atoms with many electrons.

The large family of computational methods today known as density functional theory calculation (DFT) is based on two theorems proposed by Hohenberg and Kohn. The theorems state:

1. The total energy of the system E is a unique functional of the electron density $\rho(\vec{r})$: $E = E[\rho(\vec{r})]$
2. The minimum of this functional corresponds to the ground state of the system (i.e. at T=0 K)

At this point, the brief outline of the method is provided (Nalewajski, 2001). The energy func-

tional can be rewritten in a form:

$$E[\rho(\vec{r})] = F[\rho(\vec{r})] + \int\limits_{R^3} \rho(\vec{r})V(\vec{r})d^3r, \tag{4.1}$$

where $V(\vec{r})$ represents the static part of a potential for the electron gas in solid and $F[\rho(\vec{r})]$ is some functional, which can be expressed as:

$$F[\rho(\vec{r})] = T[\rho(\vec{r})] + \frac{1}{2}\int\limits_{R^3}\int\limits_{R^3} \frac{\rho(\vec{r})\rho(\vec{r}')}{|\vec{r}-\vec{r}'|}d^3rd^3r' + E_{xc}[\rho(\vec{r})]. \tag{4.2}$$

The $T[\rho(\vec{r})]$ in formula (4.2) denotes the kinetic energy, the second part with double integral represents the Hartree energy, while the E_{xc} is exchange-correlation energy functional. The last quantity is unknown, and several schemes provide construction of its approximation. It is noteworthy, that proposed scheme is an exact theory, provided that the exact form of E_{xc} is known. In order to obtain ground state $\rho(\vec{r})$ the minimum of total energy should be found, what is equivalent with finding a solution of a set of Kohn-Sham equations:

$$\left(\frac{1}{2}\Delta_i + V_{eff}(\vec{r}) - \varepsilon_i\right)\psi_i(\vec{r}) = 0, \tag{4.3}$$

where ε_i is Kohn-Sham orbital energy and $V_{eff}(\vec{r})$ is an effective functional given by:

$$V_{eff} = V_{ext} + \int \frac{\rho(\vec{r}')}{|\vec{r}-\vec{r}'|}d^3r' + V_{xc}, \tag{4.4}$$

with V_{xc} related to exchange-correlation energy functional by:

$$V_{xc} = \frac{\delta E_{xc}}{\delta\rho}, \tag{4.5}$$

($\frac{\delta}{\delta\rho}$ denotes the variational derivative with respect to the function ρ). The symbol V_{ext} in equation (4.4) denotes the part of potential related to external sources (e.g. magnetic field).

The electron density is recovered from Kohn-Sham orbitals (ψ_i) after solving equations (4.3) with application of formula:

$$\rho(\vec{r}) = \sum_{i=1}^{N} |\psi(\vec{r})|^2. \tag{4.6}$$

The attention should be paid to the interpretation of obtained ψ_i functions. Namely, they are not equivalent to the eigenfunctions of original hamiltonian.

Bibliography

Landau, L. and Lifshitz, E. (2001). *Mechanika kwantowa*. Wydawnictwo Naukowe PWN, Warszawa.

Matar, S. F. (2013). *Prog. Solid State Ch,*, 41(3):55 – 85.

Nalewajski, R. (2001). *Podstawy i metody chemii kwantowej*. Wydawnictwo Naukowe PWN, Warszawa.

Part II

Experimental methods

Chapter 5

Photoemission Spectroscopy

5.1 Basics of Photoemission Spectroscopy

The basis of photoemission spectroscopy, which is nowadays a powerful technique in studies of electronic structure of materials, was established together with the birth of the quantum mechanics. The photoelectric effect was discovered collaterally by Heinrich Hertz and Wilhelm Hallwachs in 1887. Its theoretical interpretation provided in 1905 by Albert Einstein was one of the milestones in modern physics. The arrangement of typical photoemission experiment (Fig. 5.1) has been used. It is similar to the original experiment performed over hundred years ago. The beam of monochromatic light is directed into a sample subjected to the scrutiny. If the energy of incident photons ($\hbar\omega$) is greater than the work function (ϕ) of a studied system, the electrons are freed from the sample into a vacuum. The kinetic energy (E_{kin}) of the emitted photoelectron can be used in order to calculate the binding energy (E_B) of charge carrier in the sample. Namely, the famous Einstein-Millikan formula can be used:

$$E_{kin} = \hbar\omega - \phi - |E_B|. \tag{5.1}$$

Nowadays, the kinetic energy of photoelectrons is usually measured with application of hemispheric analyzers. The common sources of quasi monochromatic radiation used in small in-house laboratory setups are helium lamps and X-ray tubes. The first ones generate radiation with the energy 21.2 eV (He I spectral line) and 40.8 eV (He II spectral line). X-ray tubes for photoemission purposes usually contain Mg or Al anode, what corresponds to the radiation with energy equal to 1253.6 eV (Mg K_α) and 1486.6 eV (Al K_α) respectively. Another important sources of radiation are synchrotrons and free electrons lasers.

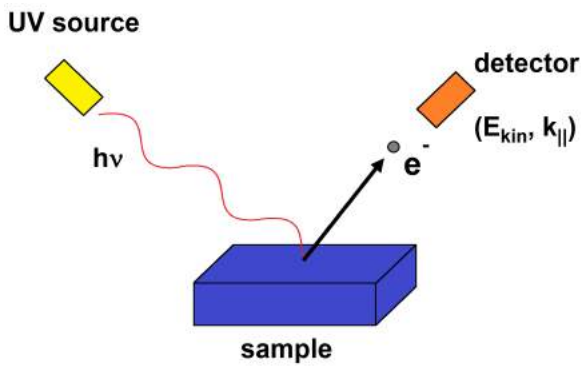

Figure 5.1: Schematic picture showing the photoemission experiment.

Despite the photoemission can be successfully performed for gases and liquids, this thesis deals only with the description of this process for crystalline solids. Here, we discuss the photoemission within the scope of simplified three step model with the so called sudden approximation. The model allows to split the act of photoemission into three steps: absorption of the photon, transport of excited electron to the surface and escape of the electron into vacuum. The sudden approximation assumes that the time of the photoemission act is many times shorter than characteristic time scale of the system, so the interaction between photoelectron and created hole can be neglected (this assumption is not justified in case of photoemission excited with extremely low photon energies). The direction of the momentum of excited electron leaving the crystalline sample, as well as its energy, can be referred to the components of its wave vector inside a solid. The component of wave vector which is parallel ($k_{||}$) to the sample surface is conserved during the act of photoemission due to the translational symmetry on the surface of perfectly periodical system, provided the momentum of the exciting photon can be neglected (which is well justified for UV radiation). The formula describing $k_{||}$ is following:

$$k_{||} = \frac{\sqrt{2mE_{kin}}}{\hbar} \sin\theta, \tag{5.2}$$

where the notation introduced in (Fig. 5.2) has been used.

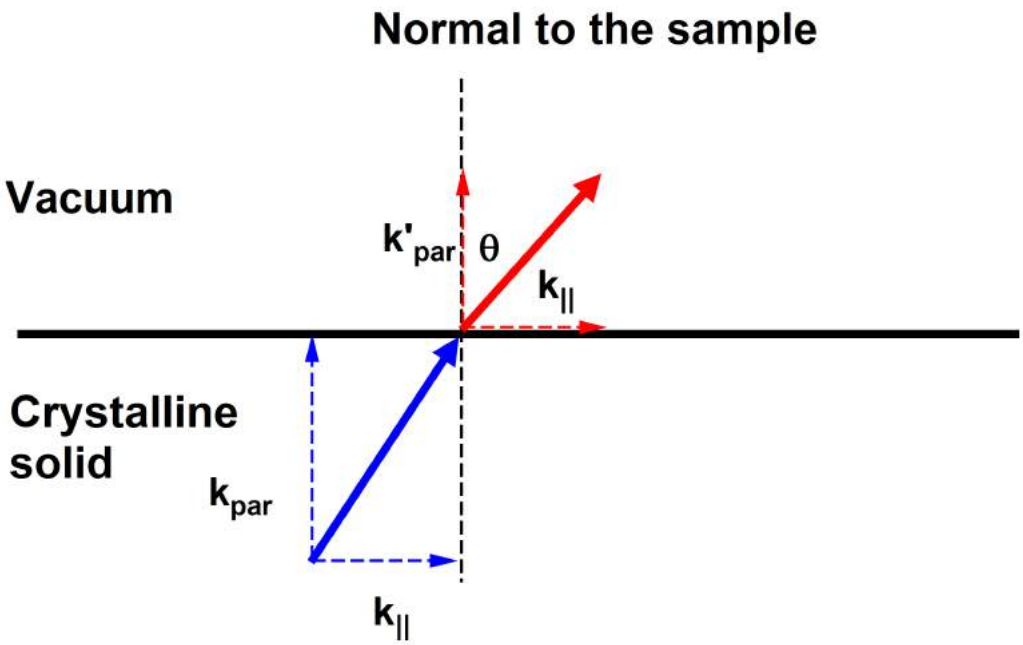

Figure 5.2: Schematic plot allowing to derive basic formulas obeyed during photoemission process.

The part of the electron's wave vector which is perpendicular ($k_{\perp}$) to the sample surface is not conserved, because of the broken translation symmetry in this direction. Additionally, one should know the dispersion relation for the final states. Assuming the free electron like (i.e. parabolic) dispersion relation, one can derive the following formula for $k_{\perp}$:

$$k_{\perp} = \sqrt{\frac{2m}{\hbar^2}} \cdot \sqrt{E_{kin}\cos^2\theta + V_0}, \tag{5.3}$$

where V_0 denotes the so called inner potential, which describes the height of the potential barrier between sample and surface (V_0 is usually of order of 10 eV). One should mention, that not all excited

electrons leave the sample. Firstly, the inelastic scattering between excited electrons implies finite mean free path of a charge carrier. As a result, the electrons freed into a vacuum come mainly from a few first atomic layers, especially in photoemission excited by the ultraviolet radiation. However, in the soft X-ray regime the contribution from the bulk of the sample to the number of emitted photoeletrons is significant. The mean free path of the excited electrons is a universal function (Hüfner, 2003; Suga and Sekiyama, 2014) of radiation energy and it has a minimum at some energy corresponding to ultraviolet radiation. This last fact points to the usefulness of the method in surface science. Secondly, some number of excited particles is reflected back to the interior of the crystalline sample on the barrier between the sample and vacuum. This can be explained by the analogy with total internal reflection effect in optics. The directions of momentum of electrons which can be freed into a vacuum must lie into so called Mahan cone, i.e. angle (θ) between the wave vector and the normal to the sample surface must be lesser than some limit angle (θ_{Mahan}) given by the formula:

$$\theta_{Mahan} = \arcsin\left(\sqrt{\frac{E_{kin}}{E_{kin}+V_0}}\right) \tag{5.4}$$

The variation of the photoemission experiment allowing for concurrent measurement of kinetic energy of photoelectron and components of its wave vector is called angle-resolved photoemission spectroscopy (ARPES). Today, technological development allows for many types of measurements based on photoelectric effect, e.g. spin resolved photoemission spectroscopy or time resolved photoemission. However, that rich family of experimental techniques is not described in this thesis, because here we concentrate on angle-resolved photoelectron spectroscopy in UV or soft X-ray regime. Now, the important question arises: what is the relation between measured number of photoelectrons as a function of a kinetic energy and emission angles? In order to give an answer one should refer to the quantum mechanical description of the system composed of crystalline solid and electromagnetic wave. The perturbation of a system due to the coupling to the photon field results in additional term H' in hamiltonian:

$$H' = \frac{e}{mc}\vec{A}\cdot\vec{p}, \tag{5.5}$$

where $\vec{p}$ denotes the momentum operator for electrons confined into a solid. The vector potential $\vec{A}$ contains the information about the light polarization and is described by a plane wave, but it can be treated as a constant, because typically the wavelength (λ) of the used radiation is many times greater than the size of an atom:

$$\vec{A} = \vec{A}_0 e^{i\vec{k}_\lambda\cdot\vec{r}} \approx \vec{A}_0.$$

The form of the coupling to the photon field presented in equation 5.5 is obtained from the general minimal coupling scheme assuming the conditions: $\phi = 0, \nabla\cdot\vec{A} = 0$ are fulfilled and neglecting the two photon term $\vec{A}^2$. Sometimes this approach is called the dipole approximation. The photocurrent excited by radiation with energy $\hbar\omega$, according to the golden Fermi rule, is given by the proportionality:

$$I \sim \sum_{f,i,k} |\left\langle \phi_{f,E_k}\middle|\vec{A}_0\cdot\vec{p}\middle|\phi_{i,k}\right\rangle|^2 \sum_s |c_s|^2 \delta(E_{kin}+E_s(N-1)-E_0(N)-\hbar\omega), \tag{5.6}$$

where $\left|\phi_{f,E_k}\right\rangle$ represents the final free electron like state of photoelectron with the kinetic energy E_k and $\left|\phi_{i,k}\right\rangle$ stands for the k-th orbital from which the photoelectron is emitted. The total energy of ground state of N electrons in absence of a radiation is denoted by $E_0(N)$, while the energy of s-th excited state after removal of electron is given by $E_s(N-1)$. The factor $|c_s|^2$ is interpreted as the probability of obtaining the s-th excited state by emission of electron from the initial $\phi_{i,k}$ orbital.

If we make a restriction $k = s$, then the equation 5.6 simplifies to:

$$I \sim \sum_{f,i,k} |M_{fik}|^2 \delta(E_k + |\varepsilon_k| - \hbar\omega), \tag{5.7}$$

where the symbol M_{fik} refers to the same matrix element as in 5.6 and ε_k stands for the energy of $\phi_{k,i}$ orbital. Such an assumption is equivalent with treating the remaining electrons in the system during the removal of electron from the particular shell as spectators, which are not involved in this process. Such an approach is justified for systems without strong correlation between electrons. In such a situation the electronic structure does not depend on the filling, so the presence of the hole does not lead to the reorganization of energy levels in a system.

The equation 5.7 informs us that the measured spectrum consists of a sharp peak (described by a Dirac δ) at the energy which corresponds to the energy of the state in a solid. Hence, for the uncorrelated system, one should expect one-to-one correspondence between the measured photoelectric spectrum and electronic structure. Of course, one should have in mind, that measured spectrum is a smooth function of kinetic energy, because of convolution with the instrumental function and to the non-zero lifetime of a photohole.

In case of presence of the correlations in the system, foregoing simplification is not justified. The measured spectra are not a simple blueprint of the electronic structure. Beyond the main lines corresponding to the energy levels of the system, the satellite peaks are observed due to rearrangement of electronic structure in presence of a hole in a system, what is reflected by the presence of many excited states labeled by s in 5.6.

For interacting system, the equation 5.7 can be rewritten with introduction the notion of spectral function A_0 :

$$I(\varepsilon) \sim \sum_{f,i,k} |M_{fik}|^2 A_0(\varepsilon;k), \tag{5.8}$$

where the experimental variable is denoted by ε:

$$\varepsilon = E_k - \hbar\omega.$$

The spectral function A is related to the one-particle retarded Green function $G(\varepsilon;k)$ via:

$$A_0(\varepsilon;k) = -\frac{1}{\pi}\,\mathrm{Im}\,G(\varepsilon;k). \tag{5.9}$$

One should have in mind that the photoemission probes only occupied states. Indeed, the measured photocurrent:

$$I(\varepsilon;k) \sim |M_{fik}|^2 A_0(\varepsilon;k) f_{FD}(\varepsilon,T)$$

is also determined by the Fermi function f_{FD}:

$$f_{FD} = \frac{1}{1+e^{(\varepsilon-\varepsilon_F)/k_BT}}, \tag{5.10}$$

where T is a temperature, k_B is Boltzmann constant, ε_F denotes the Fermi energy.

5.2 Analysis of spectral function in photoemission

The results obtained for non-interacting system are a starting point for description of spectra of a system with electronic correlations. In general, photoemission can probe the spin and momentum resolved spectral function $A^\sigma(\varepsilon,\vec{k})$ as a function of energy ε. Similarly as in equation 5.9 we have the relation between the spectral function and one-particle retarded Green function for interacting system:

$$A^\sigma(\varepsilon,\vec{k}) = -\frac{1}{\pi}\,\mathrm{Im}\,G^\sigma(\varepsilon,\vec{k}) \tag{5.11}$$

The influence of many-body interactions is described by means of so called "self-energy" operator Σ:

$$G^\sigma(\varepsilon,\vec{k}) = \frac{1}{\varepsilon - \varepsilon_0(\vec{k}) - \Sigma^\sigma(\varepsilon,\vec{k})}. \tag{5.12}$$

The bare band dispersion is denoted as $\varepsilon_0(\vec{k})$. The poles of the $G^{\sigma}(z;k)$ function in the complex plane of z determine the shape of the spectral function. The real part of z corresponding to the pole describes the peak position in spectral function, while the imaginary part describes its width.

In case of relatively small effects of "self-energy" operator and for a single first order pole, one can divide the spectral function into two parts (here we omit the spin dependency):

$$G(\varepsilon,\vec{k}) = \frac{Z_k}{\varepsilon - z_1(\vec{k})} + (1-Z_k)G_n(\varepsilon,\vec{k}), \tag{5.13}$$

where the first term of the sum is a coherent part, while the second one (G_n) is a smooth incoherent part. The so called quasiparticle weight is denoted by Z_k, and the self-energy effect is included in self-consistent equation:

$$z_1 = \varepsilon_0(\vec{k}) + \Sigma(z_1,\vec{k}).$$

The equation 5.13 contains the essence of the renormalization concept. Namely, the interaction shifts the bare energy levels according to the Σ function and the mass enhancement factor is reflected in Z_k factor.

$G(z,\vec{k})$ is a Green function, so it must obey some rigid mathematical rules (Landau and Lifshitz, 2001). In particular, causality impose that $G(z,\vec{k})$ must be an analytic function of z in the upper half of complex plane. As a consequence, one can use the following representation of the Green function:

$$G(z,\vec{k}) = -\frac{1}{\pi}\mathscr{P}\int_{\mathbb{R}} \frac{G(z',\vec{k})}{z'-z}\,\mathrm{d}z', \tag{5.14}$$

where the $\mathscr{P}\int$ symbol has a meaning of Cauchy principal value of integral. This equation can be rewritten separately for both, imaginary and real part:

$$\mathrm{Re}\,G(z,\vec{k}) = \frac{1}{\pi}\mathscr{P}\int_{\mathbb{R}} \frac{\mathrm{Im}\,G(z',\vec{k})}{z'-z}\,\mathrm{d}z' \tag{5.15}$$

$$\mathrm{Im}\,G(z,\vec{k}) = -\frac{1}{\pi}\mathscr{P}\int_{\mathbb{R}} \frac{\mathrm{Re}\,G(z',\vec{k})}{z'-z}\,\mathrm{d}z'. \tag{5.16}$$

The obtained formulas are known as Kramers-Kroning relations and are useful in analysis of effects of interaction in photoelectric spectra (i.e. for determination of self-energy operator). Same relations obeyed by the Green function $G(z,\vec{k})$ hold on also for the "self-energy" operator $\Sigma(z,\vec{k})$. Another important constraint is a normalization condition for the spectral function:

$$\int_{\mathbb{R}} A(\varepsilon,\vec{k})\,\mathrm{d}\varepsilon = 1, \tag{5.17}$$

which is closely related with the definition of momentum distribution $n(\vec{k})$:

$$n(\vec{k}) = \int_{\mathbb{R}} A(\varepsilon,\vec{k})\cdot f_{FD}(\varepsilon;T)\,\mathrm{d}\varepsilon. \tag{5.18}$$

Similar sum rules can be also written for the coherent and incoherent parts of the spectral function:

$$\int_{\mathbb{R}} A_{coh}(\varepsilon,\vec{k})\,\mathrm{d}\varepsilon = Z_k \qquad \int_{\mathbb{R}} A_n(\varepsilon,\vec{k})\,\mathrm{d}\varepsilon = 1-Z_k, \tag{5.19}$$

where A_{coh} and A_n are related to coherent and incoherent part of the Green function, respectively. The spectral function of interacting system is qualitatively different than that for non-interacting system. Namely, only coherent part is present in the latter case. In case of system of interacting electrons described by the Fermi liquid theory, in general both coherent and incoherent parts are present and well separated. At the wave vector corresponding to the Fermi vector (k_F), the incoherent part vanishes. The $n(k)$ function in this case has got a jump at k_F equal to Z_k. In case of absence of interactions the unity jump is observed at k_F.

The ARPES method gives the intensity of photocurrent as a function of energy and momentum $I(\varepsilon,\vec{k})$. The analysis of the data can be performed in two possible ways. Namely, one can analyze cuts corresponding to the constant value of momentum. These are energy distribution curves (EDC). On the other hand, one can fix the energy and deal with so called momentum distribution curves (MDC). The peak fitting procedure utilizing MDC or EDC approach can be used in order to obtain the dispersion relation from the ARPES data together and information about the lifetime of excitations (given by the width of the peak). However, in order to obtain the "self-energy" operator, the bare dispersion $\varepsilon_0(\vec{k})$ should be known. The theoretical calculations can be used in order to provide $\varepsilon_0(\vec{k})$. On the other hand, recently the self-consistent approach based on Kroning-Kramers relations which allow to determine $\Sigma(z,\vec{k})$ directly from ARPES data has been developed (Kordyuk et al., 2005).

5.3 Resonant photoemission

The photoemission spectrum of valence band of a solid can be treated, to some extent, as a superposition of contributions related to particular orbitals. Thus, the measured photocurrent $I(\varepsilon)$ can be approximately written as a linear combination:

$$I(\varepsilon) = \sum_{n,l} I_{n,l}(\varepsilon)\sigma_{n,l}(\hbar\omega), \tag{5.20}$$

where $I_l(\varepsilon)$ represents the contribution from n,l shell and $\sigma_{n,l}(\hbar\omega)$ denotes the cross section for a photoionization of this shell. The quantity $\sigma_{n,l}$ depends on the energy of incident radiation ($\hbar\omega$) in a highly rapid manner. The non-monotonic behavior of $\sigma_{n,l}(\hbar\omega)$ function, i.e. the presence of resonant peaks and minima between them, allows for estimation of $I_{n,l}(\varepsilon)$ functions. The resonant enhancement of intensity of photocurrent is realized, if the $\hbar\omega$ is close to the energy corresponding to the absorption threshold of some core level. This observation is an underlying principle of the so called resonant photoemission technique (Hüfner, 2003; Suga and Sekiyama, 2014). Here, we limit the discussion to the Ce compounds. Two main resonant transitions are encountered in such systems. These are: "$4d \to 4f$" at $\hbar\omega \approx$120 eV and "$3d \to 4f$" at $\hbar\omega \approx$880 eV. If the resonance condition is fulfilled, then the photoemission is a result of interference between two processes: direct photoionization and Auger process. Here, the description for "$3d \to 4f$" transition is provided. The change of the valence configuration of Ce during the direct photoemission can be written as:

$$3d^{10}4f^n + \hbar\omega \to 3d^{10}4f^{n-1} + e^-.$$

In contrary, two shells are involved during the indirect process. Firstly, the electron from the 3d shell is excited by photon and transferred to the 4f shell. Subsequently, the Auger decay takes place (actually super Koster-Kronig process). Namely, one electron from the 4f shell recombines with the hole in 3d level, while the second one is emitted to the vacuum. Thus the following sequence of valence changes:

$$3d^{10}4f^n + \hbar\omega \to 3d^9 4f^{n+1} \to 3d^{10}4f^{n-1} + e^-,$$

takes place. The analogous description can be formulated for the resonant photoemission near the 4d threshold. The increase in population of 4f electrons in resonance implies increased signal from

4f states. Hence, the difference between on-resonance and off-resonance spectra can be identified with 4f spectral function, providing that cross sections for other orbitals in the system does not rise significantly.

The interference between two possible channels in a quantum process resulting in the same final state was investigated by U. Fano (Fano, 1961). The intensity ($N(\hbar\omega)$) of the particular feature in the photoelectron spectrum excited with radiation of energy $\hbar\omega$ can be expressed as:

$$N(\hbar\omega) \sim \frac{(\varepsilon+q)^2}{\varepsilon^2+1}, \tag{5.21}$$

with:

$$\varepsilon = \frac{2(\hbar\omega - E_0)}{\Delta(E_0)}, \tag{5.22}$$

where E_0 is the energy of a core level ($3d$ in case of "$3d \rightarrow 4f$" transition), $\Delta(E_0)$ is a width of this level and q is some constant (characteristic of core level). The thorough analysis of the Ce $3d_{5/2}$ X-ray absorption spectrum (XAS) shows that several resonances exist for $\hbar\omega \approx 880$ eV (Cho et al., 2003). They arise due to presence of splitting of $3d$ multiplet in the intermediate step of indirect photoemission process. This fact is also reflected in photoelectric spectra. Namely, data collected with different $\hbar\omega$ contains the peak-like structure, which corresponds always to the same kinetic energy, what means that this structure arise due to the Auger effect. It turns out that the contamination of the spectra by such an effect is the smallest when the kinetic energy corresponds to the excitation of the lowest lying state of the core level multiplet, but not to the highest value of the integral photocurrent. Otherwise, the interpretation of the data is not unambiguous. The enhancement of the signal in satellite line due to the Auger effect does not reflect an intrinsic property of 4f spectral function, but can be spuriously identified as a result of the Kondo effect. Similar problem is also encountered in studies of d-electron systems (Hüfner, 2003).

There is another drawback of resonant photoelectron spectroscopy. The photoemission from $5d$ orbital is also enhanced with application of radiation with $\hbar\omega$ corresponding to "$3d \rightarrow 4f$" transition. However, the expected contribution from $5d$ states is not as large as for $4f$ ones (Sekiyama et al., 2001).

5.4 Photoemission spectroscopy on Ce intermetallics

The photoelectric spectrum measured on a polycrystalline sample of a simple metal (e.g. Au or Cu) at low temperature reproduces well the shape of the Fermi function (5.10) near the Fermi energy (ε_F). The completely different situation is encountered for many Ce intermetallic compounds, which display significant anomalies in measured spectrum close to ε_F due to many body effects. It is believed that a proper theoretical description of many body interactions which are present in Ce systems is provided by Anderson lattice model. The hamiltonian of the periodic Anderson model (PAM) has got a form:

$$H = \sum_{k,\sigma} \varepsilon_k c^\dagger_{k\sigma} c_{k\sigma} + \varepsilon_f \sum_{i,\sigma} f^\dagger_{i\sigma} f_{i\sigma} + U \sum_i n_{i\uparrow} n_{i\downarrow} + \sum_{i,k,\sigma} (V_{ik} c^\dagger_{k,\sigma} f_{i\sigma} + H.C.) \tag{5.23}$$

where the first term stands for the bare conduction band, the second part describes the lattice of f moments (U - intrasite Coulomb repulsion), the third part describe the mixing (V_{kf} - hybridization function) between the f states and the conduction band. This model takes into account the exchange interaction between different f-sites. Hence, it is suitable for description of systems, which consists of dense sublattice of f orbitals in a nonmagnetic matrix. In case of a system with relatively small concentration of Ce, each Ce atom can be treated to some extent as isolated impurity, what can be described by the single impurity Anderson model (SIAM). The hamiltonian of the SIAM can be

written as:

$$H = \sum_{k,\sigma} \varepsilon_k c^{\dagger}_{k\sigma} c_{k\sigma} + \varepsilon_f \sum_{\sigma} f^{\dagger}_{\sigma} f_{\sigma} + U n_{\uparrow} n_{\downarrow} + \sum_{k,\sigma} (V_k c^{\dagger}_{k,\sigma} f_{\sigma} + H.C.), \tag{5.24}$$

with application of the same notation as in equation (5.23). However, in this case we have not interaction between f moments at different sites of crystal lattice.

The spectral function for both models (PAM and SIAM) has been calculated within many theoretical schemes (Czycholl, 1985; Glossop and Logan, 2002; Horvatić et al., 1987). The crucial parameter is the filling of the f shell (n_f). This quantity is a measure of the degree of localization of the f electrons and plays the same role as the J_{cf} coupling constant (cf. Doniach diagram). In case of $n_f \approx 1$, i.e. in so called Kondo regime, the spectral function reveals the sharp peak in a vicinity of ε_F. This is a universal feature, obtained within many computational schemes, for both PAM and SIAM. The sharp resonant peak (so called Kondo peak) is interpreted as a symptom of a Kondo singlet (Frota, 1992). The spectrum consists also of some side peaks, albeit their shape and location depend on the model parameters such as onsite Coulomb repulsion (U) and the dispersion of bare conduction band (ε_k). The mixing between f shell and conduction band, described by V_{cf}, results in delocalization of f electrons. In case of mixed valence state (i.e. for $0.5 < n_f < 0.8$) the peak is still present in vicinity of ε_F, but it becomes broadened. Significant spectral weight is transferred above the Fermi level.

The enhancement of the spectral function in vicinity of ε_F is visible in large values of Sommerfeld γ coefficient reported for many Ce compounds. However, direct measurement of the Kondo peak was a serious challenge for earlier photoemission spectroscopy experiments. It should be noted that the Kondo peak is located above ε_F at energy:

$$\delta = k_B T_K \sin(\pi n_f) \tag{5.25}$$

in order to satisfy the Friedel sum rule, whereas the photoemission probes the occupied states. Hence, it provides mainly the information about spectral features with binding energy below ε_F. On the other hand, from the spectrum collected at temperature T, one can recover the spectral function up to $5k_BT$ (k_B - Boltzmann constant) dividing it by the Fermi function. Another issue, which will be discussed further in the text, is a suppression of the Kondo peak at elevated temperature. Therefore, actually a "tail" of the Kondo peak is recorded in experiment. To sum it up, these points together with exigency of very high resolution (the resolution should be of order of k_BT_K, in order to observe the Kondo peak (Garnier et al., 1997)) make that the direct measurement of a Kondo resonance is a very demanding task.

Several fundamental questions arise in studies of cerium intermetallic compounds. The problems of key importance for the modern physics are encountered in such systems. One can consider for example such ideas as asymptotic freedom or quantum entanglement, which emerge in theoretical studies of the Kondo problem. The direct scientific aim which underlies under the research in the field of cerium compounds is to provide a realistic description of them. There is a long standing debate on the interpretation of valence band photoelecton spectra. According to some studies, it seems that a single impurity Anderson model, treating f electrons as localized, captured well the physical situation. On the other hand, there are reports which contain results which can be explained exclusively by considering itinerant character of f electrons, what is in a scope of periodic Anderson model. The degree of delocalization of f electrons, presence of the spectroscopic signatures (i.e. presence of a Kondo peak in spectra) as well as their thermal evolution (i.e. large to small Fermi surface crossover) are a subject of controversy in the literature (Aynajian et al., 2012; Hackl and Vojta, 2008). The technical development of experimental methods such as angle-resolved photoelectron spectroscopy, allows to probe the dispersion relation in a close vicinity of the Fermi energy. This opens a route to the comparison of microscopic parameters derived from the model fit to the directly measured band structure with results of transport and thermal measurements. Here, a brief overview of the most important results of studies of cerium intermetallics with photoelectron spectroscopy will be given,

The analysis of the bulk 4f spectral function of $CeRu_2Si_2$ and $CeRu_2$ compounds obtained by means of photoelectron spectroscopy at Ce 3d-4f resonance (Sekiyama et al., 2000) provides a good illustration of applicability of SIAM. The strength of a mixing between f electrons and conduction band, represented by the Kondo temperature T_K, is different in these compounds . $CeRu_2Si_2$ is characterized by $T_K \approx$22 K, while for $CeRu_2$ T_K is of order of 1000 K. In the first compound the effects related to Coulomb repulsion on 4f shell have crucial meaning, what is reflected in a valency of Ce which is close to 3. On the other hand, the physics in $CeRu_2$ is dominated by a strong mixing between f level and conduction band. One can treat that compounds as two different limits of PAM. Namely, the $CeRu_2Si_2$ compound corresponds to SIAM which treats f electrons as localized, while $CeRu_2$ can be described in terms of a quasiparticle band. According to SIAM, the ground state of an f electron system can be described as a linear combination of $f^1{}_{\frac{5}{2}}$ and f^0 configuration due to non-zero hybridization V_{cf}. However, the photoelectron spectroscopy probes also excited states. Indeed, the spectral function of a typical Ce compound characterized by low T_K, consists of three peaks which correspond to different number of f electrons in the final state. These are: f^0, $f^1_{\frac{5}{2}}$ and $f^1_{\frac{7}{2}}$ final states. The first one, f^0 forms usually a broad hump-like structure with a maximum at binding energy equal to -0.2 eV. The $f^1_{\frac{5}{2}}$ spectral feature is located at the Fermi level and it is interpreted as a tail of the Kondo resonance peak, which itself has the maximum above ε_F. The $f^1_{\frac{7}{2}}$ final state is a spin-orbit partner peak, and it is observed at about -0.3 eV. Beyond such structures, the crystal field side bands give a contribution to the spectrum. However, there are usually not resolved because of not sufficient resolution. The analysis of the spectra of low T_K systems within the framework of the SIAM with the non-crossing approximation (NCA) has shown that, the effects of the crystal field should be taken into account, in order to obtain realistic value of T_K from spectra fitting (Ehm et al., 2007). On the other hand, the spectra of $CeRu_2$ compound cannot be described properly with reference to different final states of f shell. The angle-integrated spectrum (collected with the same resolution as that for $CeRu_2Si_2$) of such a compound displays a broad peak below the Fermi energy. This is interpreted as a fingerprint of the itinerant character of f electrons. Such a state should be well modeled with application of band structure calculations for example the tight binding method.

Numerous experimental studies testifies that SIAM provides sufficient framework for interpretation of the (angle-integrated) photoemission spectra on polycrystalline samples of Ce compounds characterized by low value of T_K (see for example (Garnier et al., 1997)). However, the high resolution angle resolved spectra of display features beyond the simple SIAM picture. The main disadvantage of SIAM is the lack of the coherence scale T_{coh}. Some experiments point to the thermal evolution of the spectra which is inconsistent with SIAM (Joyce et al., 1992). Such an inconsistency can be explained by reference to the solution of PAM. The exact numerical solution of such a model (Tahvildar-Zadeh et al., 1998) obtained within quantum Monte Carlo approach shows that the thermal evolution of a spectral function is not as rapid as in the case of SIAM. Moreover, it shows that the Kondo peak persists in the spectral function up to $10T_K$, what explains very weak dependency of the spectra on temperature. Another predictions of the PAM is the absence of universal scaling of the Kondo peak intensity with the hybridization. In case of impurity models the Kondo peak height is proportional to the $1/V_{cf}^2$ factor. Among discrepancies between experimental data and the description of spectra in terms of SIAM, the problem of dispersion of f states was reported many times (Andrews et al., 1996, 1995; Vyalikh et al., 2006). However, the first systematic studies of dispersion of spectral features related to the Kondo peak is presented in (Im et al., 2008). The authors have studied the electronic structure of quasi two dimensional heavy fermion compound $CeCoGe_{1.2}Si_{0.8}$. Such a system is characterized by the following energy scales: $T_K \approx$ 300 K, $T_{coh} \approx$180 K. The ARPES spectra collected below T_{coh} with application of resonance spectroscopy near $4d$ edge clearly shows the itinerant character of f electrons. The dispersion of a quasiparticle $E^{\pm}(k)$ band was fitted with the simplified formula based

on PAM:

$$E^{\pm}(k) = \frac{\tilde{\varepsilon}_f + \varepsilon_k \pm \sqrt{(\tilde{\varepsilon}_f - \varepsilon_k)^2 + 4|\tilde{V}_k|^2}}{2}, \tag{5.26}$$

where the bare dispersion of conduction band $\varepsilon_k\pm$ was assumed as a linear function of k vector. The constant strength of the hybridization between f electrons and conduction band carriers was assumed: $\tilde{V}_k \approx$const. The renormalized f level position was used to estimate the Kondo temperature:

$$T_K = \frac{\tilde{\varepsilon}_f}{k_B}. \tag{5.27}$$

The coherence temperature is equal to the energy corresponding to the maximum of hole quasiparticle band divided by k_B. Obtained values of T_{coh}, T_K and mass enhancement $\frac{m^\star}{m}$ turned out to be in good agreement with these obtained from thermodynamic and transport measurements. On the other hand, one should have in mind that the hybridization strength V_{cf} should reflect the symmetry of both, the crystal lattice and f orbital character. The variation of quasiparticle weight at the Fermi level, observed in $Ce_2Co_{0.8}Si_{3.2}$ by means of ARPES was interpreted in a light of this effect (Starowicz et al., 2014). The cornerstone of such an analysis is the theoretical analysis of hybridization effects in PAM by means of slave boson approach (Ghaemi et al., 2008). According to such a theory, there are some directions in the Brillouin zone which correspond to nodes in the hybridization function. This opens a way to possibility of extraction of the variation of V_{cf} function from the ARPES data.

5.5 Matrix elements in ARPES

The measured signal related to photoemission from states characterized by wave vector $\vec{k}$ and energy ε is given by the proportionality:

$$I(\varepsilon,\vec{k}) \sim |M_{fik}|^2 A(\varepsilon,\vec{k}) f_{FD}(\varepsilon,T) \tag{5.28}$$

The spectral function $A(\varepsilon,\vec{k})$ and the Fermi function have been discussed in preceding chapters. Here, we would like to concentrate on the role of the matrix element M_{fik}. It turns out, that the measured intensity of photocurrent can be significantly modified, even totally suppressed, due to details of geometric arrangement of experimental setup (Damascelli et al., 2003). Such a behavior is explained by the influence of M_{fik} quantity. Indeed, matrix elements depend on the geometry of the measurement, i.e. on the energy and polarization of incident radiation as well as on the geometrical relation between the propagation vector of radiation and detection direction with respect to the sample position. M_{fik} identified from equation 5.6 can be rewritten with application of commutation rules as:

$$M_{fik} = \left\langle \phi_{f,E_k} \middle| \vec{A}\cdot\vec{p} \middle| \phi_{i,k} \right\rangle \sim \left\langle \phi_{f,E_k} \middle| \vec{\xi}\cdot\vec{r} \middle| \phi_{i,k} \right\rangle = \int_R \phi^\star_{f,E_k}(\vec{r})\vec{\xi}\cdot\vec{r}\phi_{i,k}(\vec{r})\,\mathrm{d}^3 r, \tag{5.29}$$

with $\vec{\xi}$ being a unit vector describing the polarization of the incoming photons. The formula 5.29 shows, that M_{fik} is proportional to the matrix element of dipole moment operator between an initial and a final state. The initial state $\left|\phi_{i,k}\right\rangle$ usually can be treated as the linear combination of atomic orbitals, which can be separated into orbital and radial part. The final state can be approximated by a plane wave function:

$$\left\langle \vec{r} \middle| \phi_{f,E_k} \right\rangle \sim e^{i\vec{\kappa}\cdot\vec{r}},$$

where κ is a vector connecting a sample with the detection point. The dependency of M_{fik} on polarization of incident radiation can be useful in determination of dominating orbital character of measured spectral features. Imagine that the photoemission experiment in geometry depicted in (Fig. 5.3) is performed.

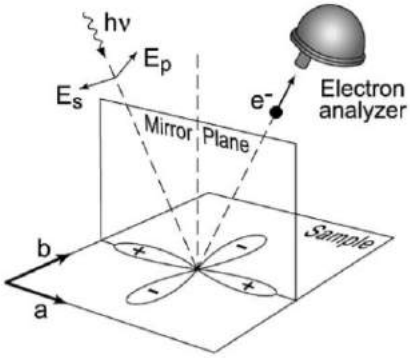

Figure 5.3: Schematic plot of exemplary ARPES experimental geometry allowing to study observed orbital contributions in ARPES spectra. Taken from (Damascelli et al., 2003)

We can distinguish some mirror plane, i.e. the plane that is determined by the direction of detection $\vec{\kappa}$ and the propagation vector ($\vec{q}$) of incoming light. At the beginning we can assume that the polarization of light $\vec{\xi}$ is perpendicular to the mirror plane ($\vec{\xi} = \vec{E}_s$). Let's apply the reflection with respect to the mirror plane to the expression under integral giving matrix element 5.29. This operation changes the sign of the dipole operator, while the function describing the final state remains unchanged. Thus, if the function describing the initial state is invariant under performed reflection (e.g. s atomic orbital), the overall expression under integral changes sign and the integral gives zero. On the other hand, if the initial state has got an odd symmetry, then integration results in some non-zero value. Hence, photoemission in mirror plane with a polarization of the radiation perpendicular to this plane probes only states which have got odd symmetry with respect to the mirror plane. The same reasoning can be repeated for the light with polarization lying in mirror plane. In such a case, the situation is reversed. Namely, the contribution from even parity orbitals with respect to the mirror plane is observed, while that connected with the odd ones vanishes. The table 5.1 displays the symmetry of the atomic like orbitals (here we deal with real atomic orbitals, which have well defined parity under space reflections, in distinctions to the complex orbitals given by spherical harmonics) with respect to mirror plane reflection in described experimental geometry, as well as assess visibility in photoemission induced by radiation with particular polarization.

Table 5.1: The atomic orbitals together with their parity with respect to mirror symmetry (cf. (Fig. 5.3)). The suppression of contribution related to particular orbital character in a spectrum collected with radiation with polarization in-plane $\vec{E}_p$ or out off plane $\vec{E}_s$ is denoted by $\times$. These results are valid only for the photoemission in mirror plane.

orbital	parity	ξ_{ip}	ξ_{op}
s	even		$\times$
p_x	even		$\times$
p_y	odd	$\times$	
p_z	even		$\times$
d_{z^2}	even		$\times$
d_{xz}	even		$\times$
d_{yz}	odd	$\times$	
d_{xy}	odd	$\times$	
$d_{x^2-y^2}$	even		$\times$
f_{z^3}	even		$\times$
f_{xz^2}	even		$\times$
f_{yz^2}	odd	$\times$	
f_{xyz}	odd	$\times$	
$f_{z(x^2-y^2)}$	even		$\times$
$f_{x(x^2-3y^2)}$	even		$\times$
$f_{y(3x^2-y^2)}$	even		$\times$

5.6 Experimental setups

At this point, the detailed description of used experimental setups will be given. The measurement of specific heat (two-tau method) and electrical resistivity (four-probe technique) have been performed with application of standard Physical Property Measurement System (PPMS, Quantum Design). The description of these methods would be mainly technical, so it is omitted.

5.6.1 ARPES setup available in Department of Solid State Physics, Institute of Physics, Jagiellonian University

The significant part of the data presented in this thesis was collected with application of equipment available in the Laboratory of Photoelectron Spectroscopy in Department of Solid State Physics (Insititute of Physics, Jagiellonian University in Krakow). The equipment was bought thanks to the financial support from ATOMIN project.

The single crystals were oriented along high symmetry directions using Laue method, before photoemission studies. Laue patterns were collected using the setup (Laue camera) allowing for experiments in backscattered radiation geometry. The intensity of the reflected X-rays were collected by CCD detector. X-ray radiation was generated by standard X-ray tube with Mo anode.

The band structure of investigated systems was measured with conventional in-house ARPES setup. The ultra high vacuum (uhv) conditions were realized in the system of vacuum chambers. Typical base pressure in the analysis chamber was equal to $5 \cdot 10^{-11}$ mbar. Measurements were performed at fixed temperature, selected between 10.5 K and 340 K. The sample cooling was provided by He refrigerator working in a closed cycle. During the measurements sample was mounted on the manipulator with five degrees of freedom, what enabled for Fermi surface mapping. Hemispheri-

cal photoelectron energy analyzer Scienta R4000 present in the system allowed for measurements with the minimal resolution of 1.8 meV and 0.1°, for energy and angles respectively. The photoelectrons are excited by the radiation generated by helium lamp (He I and He II spectral lines with energies 20.1 eV and 40.8 eV respectively) or X-ray tube (MgK_α and AlK_α radiation with energies 1253.6 eV and 1486.6 eV respectively). The analysis chamber is also equipped with instruments allowing for performing low energy electron diffraction (LEED). Additionally, several vacuum chambers allowing for sample preparation are present within the same uhv system. The heating stage enables heating the samples up to 2000°C. The samples can be also cleaved and sputtered by Ar^+ ions generated by ion gun.

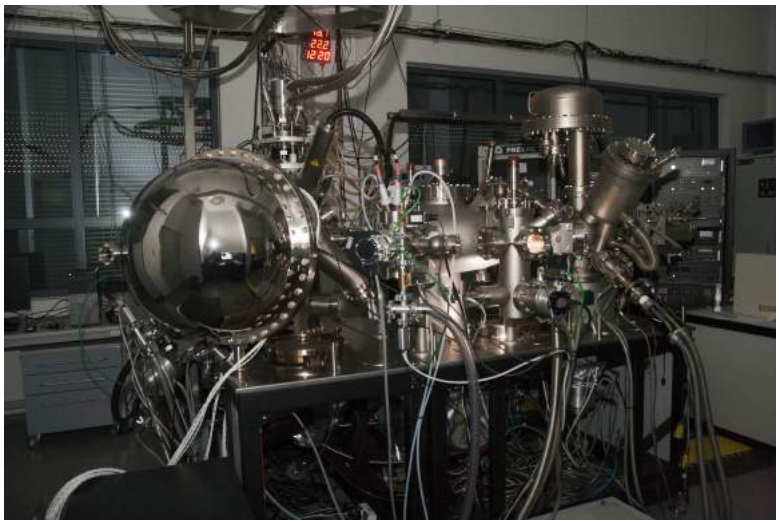

Figure 5.4: Experimental setup for ARPES measurements available in Department of Solid State Physics (Jagiellonian University). (photo: M. Rosmus)

5.6.2 Cassiopee beamline, synchrotron Soleil

High intensity and broad energy range makes synchrotron radiation a powerful tool in edge-cutting research in material science. The opportunity of performing a resonant photoemission is of particular interest for Ce intermetallics. Thorough studies of fine spectral feature in band structure close to the Fermi level need good resolution and considerable statistics. The enhancement of cross section for photoionization of Ce 4f electrons is encountered at $\hbar\omega \approx 120$ eV, 880 eV. Such energies are inaccessible in conventional in-house experimental setups. Thus, synchrotrons allow to explore subtle effects, e.g. related to Kondo physics, which are hardly visible with conventional sources.

One of these types of sources is the synchrotron center SOLEIL, which is located near Paris, in France. Particularly good conditions to study compounds of Ce are provided in the Cassiopee ARPES endstation [3]. Such a beamline allows for experiments with application of exciting radiation between 8 eV and 1500 eV. Actually, there are two independent ARPES setups in this endstation: the first one used for conventional ARPES measurements and the second one for spin resolved photoemission. However, they cannot be used simultaneously because the beam coming from the ring is directed by the reflecting mirror to the one selected part. There is also a setup allowing for preparation of samples with application of molecular beam epitaxy (MBE) technique. These parts are connected with each

[3] Detailed description and technical information of the Cassiopee beamline is available in the web page: https://www.synchrotron- soleil.fr/en/beamlines/cassiopee

other within a single ultra-high vacuum system enabling a transfer of samples between chambers. Two undulators are used in order to obtain electromagnetic radiation. One generates photons with energies between 8 eV and 155 eV, while the second one works between 100 eV and 1500 eV. The spin resolved spectra are collected with application of Mott detector and energy electron analyzer SES2002. It is possible to collect a spectrum corresponding to a single angle. The ARPES part of setup is equipped with Scienta R4000 hemispheric analyzer. It allows to measure with many angular channels simultaneously. The optimal energy resolution obtained at $\hbar\omega \approx$120 eV was dominated by the spectral width of radiation and it was equal to about 15 meV (it was possible to set the better resolution, but it lead to worse quality of the spectra). The sample is mounted on the four-axis manipulator. The lowest possible temperature near the sample is equal to 6 K. The manipulator is cooled by liquid He from a Dewar flask (open system). There is a possibility to change a polarization of incoming radiation between linear vertical and linear horizontal.

Figure 5.5: Experimental setup for ARPES measurements available at Cassiopee beamline of Soleil synchrotron. (photo: M. Rosmus)

Bibliography

Andrews, A. B., Joyce, J. J., Arko, A. J., Fisk, Z., and Riseborough, P. S. (1996). *Phys. Rev. B*, 53:3317–3326.

Andrews, A. B., Joyce, J. J., Arko, A. J., Thompson, J. D., Tang, J., Lawrence, J. M., and Hemminger, J. C. (1995). *Phys. Rev. B*, 51:3277–3280.

Aynajian, P., Neto, E., Gyenis, A., Baumbach, R., Thompson, J., Fisk, Z., Bauer, E., and Yazdani, A. (2012). *Nature*, 486:201–6.

Cho, E.-J., Jung, R.-J., Choi, B.-H., Oh, S.-J., Iwasaki, T., Sekiyama, A., Imada, S., Suga, S., Muro, T., Park, J.-G., and Kwon, Y. S. (2003). *Phys. Rev. B*, 67:155107.

Czycholl, G. (1985). *Phys. Rev. B*, 31:2867–2880.

Damascelli, A., Hussain, Z., and Shen, Z.-X. (2003). *Rev. Mod. Phys.*, 75:473–541.

Ehm, D., Hüfner, S., Reinert, F., Kroha, J., Wölfle, P., Stockert, O., Geibel, C., and Löhneysen, H. v. (2007). *Phys. Rev. B*, 76:045117.

Fano, U. (1961). *Phys. Rev.*, 124:1866–1878.

Frota, H. O. (1992). *Phys. Rev. B*, 45:1096–1099.

Garnier, M., Breuer, K., Purdie, D., Hengsberger, M., Baer, Y., and Delley, B. (1997). *Phys. Rev. Lett.*, 78:4127–4130.

Ghaemi, P., Senthil, T., and Coleman, P. (2008). *Phys. Rev. B*, 77:245108.

Glossop, M. T. and Logan, D. E. (2002). *J. Phys. Condens. Matter*, 14(26):6737–6760.

Hackl, A. and Vojta, M. (2008). *Phys. Rev. B*, 77:134439.

Horvatić, B., Sokcević, D., and Zlatić, V. (1987). *Phys. Rev. B*, 36:675–683.

Hüfner, S. (2003). *Photoelectron Spectroscopy: Principles and Applications*, pages 133–148. Springer Berlin Heidelberg.

Im, H. J., Ito, T., Kim, H.-D., Kimura, S., Lee, K. E., Hong, J. B., Kwon, Y. S., Yasui, A., and Yamagami, H. (2008). *Phys. Rev. Lett.*, 100:176402.

Joyce, J. J., Arko, A. J., Lawrence, J., Canfield, P. C., Fisk, Z., Bartlett, R. J., and Thompson, J. D. (1992). *Phys. Rev. Lett.*, 68:236–239.

Kordyuk, A. A., Borisenko, S. V., Koitzsch, A., Fink, J., Knupfer, M., and Berger, H. (2005). *Phys. Rev. B*, 71:214513.

Landau, L. and Lifshitz, E. (2001). *Mechanika kwantowa*. Wydawnictwo Naukowe PWN, Warszawa.

Sekiyama, A., Iwasaki, T., Matsuda, K., Saitoh, Y., Onuki, Y., and Suga, S. (2000). *Nature*, 403:369–398.

Sekiyama, A., Suga, S., Iwasaki, T., Ueda, S., Imada, S., Saitoh, Y., Yoshino, T., Adroja, D., and Takabatake, T. (2001). *J. Electron Spectrosc.*, 114-116:699 – 703.

Starowicz, P., Kurleto, R., Goraus, J., Schwab, H., Szlawska, M., Forster, F., Szytuła, A., Vobornik, I., Kaczorowski, D., and Reinert, F. (2014). *Phys. Rev. B*, 89:115122.

Suga, S. and Sekiyama, A. (2014). *Photoelectron Spectroscopy: Bulk and Surface Electronic Structures*, pages 7–31, 155–217. Springer Berlin Heidelberg.

Tahvildar-Zadeh, A. N., Jarrell, M., and Freericks, J. K. (1998). *Phys. Rev. Lett.*, 80:5168–5171.

Vyalikh, D. V., Kucherenko, Y., Danzenbächer, S., Dedkov, Y. S., Laubschat, C., and Molodtsov, S. L. (2006). *Phys. Rev. Lett.*, 96:026404.

Part III

Results

Chapter 6

Kondo Lattice Behavior Observed in $CeCu_9In_2$ Compound

R. Kurleto, A. Szytuła, J. Goraus, S. Baran, Yu. Tyvanchuk, Ya. M. Kalychak, and P. Starowicz, Journal of Alloys and Compounds **803**, 576-584 (2019). doi: 10.1016/j.jallcom.2019.06.140

Highlights

- $CeCu_9In_2$ is a new system which hosts Kondo lattice state with coherence temperature of 45 K
- electrical resistivity varies with a temperature in a way typical of Kondo lattice systems
- Ce 4f contribution to the specific heat displays pronounced anomaly at 1.8 K
- at higher temperatures (≈30 K) contribution from crystal field effect is visible in specific heat
- extracted Ce 4f spectral function near the Fermi energy with application of ultraviolet photoelectron spectroscopy shows features related to $f^1_{7/2}$ and $f^1_{5/2}$ final states
- Gunnarsson-Schönhammer analysis has been applied to XPS spectra of Ce 3d core levels confirming presence of mixing between 4f orbitals and conduction band
- ab initio calculations suggest that one may expect a Fermi surface nesting in $CeCu_9In_2$ compound

Kondo Lattice Behavior Observed in the $CeCu_9In_2$ Compound

R. Kurleto[a], A. Szytuła[a], J. Goraus[b], S. Baran[a], Yu. Tyvanchuk[c], Ya. M. Kalychak[c], P. Starowicz[a]

[a] *Marian Smoluchowski Institute of Physics, Jagiellonian University, Łojasiewicza 11, 30-348 Kraków, Poland*
[b] *Institute of Physics, University of Silesia, 75 Pułku Piechoty 1a, 41-500 Chorzów, Poland*
[c] *Department of Analytical Chemistry, Ivan Franko National University of Lviv, Kyryla and Mephodiya 6, 79005 Lviv, Ukraine*

arXiv:1906.10748v2 [cond-mat.str-el] 11 Mar 2020

Abstract

We report systematic studies of $CeCu_9In_2$, which appears to be a new Kondo lattice system. Electrical resistivity exhibits a logarithmic law characteristic of Kondo systems with a broad maximum at T_{coh} ≈45 K and it obeys the Fermi liquid theory at low temperature. Specific heat of $CeCu_9In_2$ is well described by the Einstein and Debye models with electronic part at high temperature. Fitting of the Schottky formula to low temperature 4f contribution to specific heat yielded crystal field splitting of 50.2 K between a doublet and quasi-quartet. The Schotte-Schotte model estimates roughly Kondo temperature as T_K ≈5 K, but does not reproduce well the data due to a sharp peak at 1.6 K. This structure should be attributed to a phase transition, a nature of which is possibly antiferromagnetic. Specific heat is characterized with increased Sommerfeld coefficient estimated as γ ≈132 mJ/(mole·K^2). Spectra of the valence band, which have been collected with ultraviolet photoelectron spectroscopy (UPS), show a peak at binding energy≈250 meV, which originates from the Ce 4f electrons and is related to the $4f^1{}_{7/2}$ final state. Extracted 4f contribution to the spectral function exhibits also the enhancement of intensity in the vicinity of the Fermi level. Satellite structure of the Ce 3d levels spectra measured by X-ray photoelectron spectroscopy (XPS) has been analyzed within the framework of the Gunnarsson-Schönhammer theory. Theoretical calculations based on density functional theory (FPLO method with LDA+U approach) delivered densities of states, band structures and Fermi surfaces for $CeCu_9In_2$ and $LaCu_9In_2$. The results indicate that Fermi surface nesting takes place in $CeCu_9In_2$.

Keywords: rare earth alloys and compounds, Kondo effect, heat capacity, electrical transport, photoelectron spectroscopies, electronic band structure

1. Introduction

Presence of unpaired 4f electron in cerium atom leads to many unusual physical phenomena in cerium intermetallic compounds. Often, experimental evidence points to a dichotomous character of 4f electrons, which are neither fully localized nor fully itinerant. This plays an important role in physics of such systems. These electrons form a relatively narrow band, which hybridizes with carriers from a conduction band. This coupling can lead to quenching of magnetic moments of f electrons and to formation of singlets in a ground state. Other complex states, such as a Kondo lattice or a mixed valency are also possible. The aforementioned dynamic singlet state in a Kondo regime is manifested by a pronounced anomaly in an electrical resistivity and by the so called Kondo peak in a spectral function. While the presence of the latter feature in a single impurity regime (Kondo regime) is well established, analogous spectral shape in the case of a Kondo lattice may be an interesting subject of research.

Crystal chemistry of ternary indides with rare-earth and transition metal elements was the subject of previous studies due to intriguing physical properties [1, 2, 3]. The structural phase diagram of the Ce–Cu–In system was constructed previously and extensively discussed [1, 4, 5]. $CeCu_9In_2$ compound crystallizes in the YNi_9In_2-type tetragonal structure (P4/mbm space group), with lattice constants: a=8.5403(4) Å and c=5.0204(5) Å. $LaCu_9In_2$ is isostructural to $CeCu_9In_2$. Its crystal structure, specific heat and magnetic susceptibility were reported before [6]. Lattice constants of $LaCu_9In_2$ slightly differ from those obtained for the cerium counterpart (a=8.6351(4) Å, c=5.1488(3) Å). Both intermetallic compounds are characterized by narrow homogeneity ranges with substitution of Cu by In [1]. Specific heat of $LaCu_9In_2$ is well modeled by the sum of phononic and electronic contributions (details of the fitting procedure are available elsewhere [6]). The magnetic susceptibility of $LaCu_9In_2$, measured at 0.1 T and 1 T, is almost temperature independent. This fact was interpreted as a symptom of a Pauli paramagnetism [6]. It should be mentioned that replacement of a transition metal may have a significant effect; recently, a mixed valence state has been proposed for the isostructural $CeNi_9In_2$ compound [3, 7, 8, 9].

Magnetic properties of $CeCu_9In_2$ were studied before [6]. Measured magnetic susceptibility follows the Curie-Weiss law in a broad temperature range (100-350 K). The estimated Curie-Weiss temperature is equal to −39 K, while inferred value of effective magnetic moment is slightly enhanced to μ=2.88 μ_B, which can be compared to μ=2.54 μ_B,

Email addresses: rafal.kurleto@uj.edu.pl (R. Kurleto), pawel.starowicz@uj.edu.pl (P. Starowicz)

what is a theoretical value for free Ce^{3+} [6]. This value suggests that valency of cerium is close to 3.

In this article we describe physical properties of the $CeCu_9In_2$ compound. Namely, we provide electrical resistivity, specific heat, as well as photoelectron spectra of the valence band and Ce 3d levels. In order to reveal the role of the 4f electrons we have also performed measurements on isostructural $LaCu_9In_2$. The obtained spectra are confronted with the results of theoretical calculations. We have analyzed our data in terms of the Kondo lattice with the Fermi liquid ground state. Our results testify significant coupling between the 4f electrons and carriers from the conduction band in $CeCu_9In_2$. This compound is a new system in which a realization of a Kondo lattice takes place.

2. Materials and methods

Fabrication and characterization of polycrystalline samples of $CeCu_9In_2$ and $LaCu_9In_2$ (the latter with exact stoichmiotery: $LaCu_{8.25}In_{2.75}$) were described elsewhere [6]. Electrical resistivity has been measured with application of four-terminal alternating current technique in Physical Property Measurement System (PPMS, Quantum Design) in temperature range 2–300 K. Specific heat has also been measured in PPMS, with application of a relaxation method (two-tau model), in similar temperature range. Additional measurement of specific heat in temperature range 0.4–10 K has been performed with application of ^{3}He refrigerator.

Photoelectron spectroscopy has been conducted with an in-house experimental setup, equipped with VG Scienta R4000 photoelectron energy analyzer. X-ray photoelectron spectroscopy (XPS) has been performed with application of Mg K_α (hν=1253.6 eV) and Al K_α (hν=1486.6 eV) radiation (without a monochromator) at temperature: 12.5 K, 100 K or 292 K. He I (hν=21.2 eV) and He II (hν=40.8 eV) spectral lines from helium lamp have been used in the ultraviolet photoelectron spectroscopy (UPS) studies. Spectra have been collected at the same temperatures as the ones from XPS. Both XPS and UPS measurements do not reveal any significant change in the function of temperature, so further in the article we present only spectra collected at the lowest possible temperature (12.5 K). Base pressure during measurements was equal to $5{\cdot}10^{-11}$ mbar. Before measurements, surface of the samples was polished under ultra high vacuum conditions (base pressure $2{\cdot}10^{-10}$ mbar) with application of a diamond file. Calibration was provided by a measurement of binding energy of the Au 4f states on polycrystalline gold layer and by measurement of Fermi edge of polycrystalline Cu for XPS and UPS measurements, respectively.

Full potential local orbital (FPLO) code [10] in scalar relativistic version has been used in order to obtain partial densities of states (DOS) of $CeCu_9In_2$ and $LaCu_9In_2$. Additional correlations have been involved in around mean field scheme with application of local spin density approximation (LSDA+U) [11]. Perdew-Wang exchange-correlation potential [12, 13] has been assumed in calculations. In case of the compound with cerium, DOS have been obtained for Coulomb repulsion on the f shell equal to 0 eV, 2 eV (not shown in this paper) and 6 eV. The band dispersion along important crystallographic directions in k-space as well as Fermi surface (FS) of both studied compounds have been calculated with application of Elk software [14]. The results from FPLO and Elk are consistent. All theoretical calculations have been performed assuming non-magnetic state of $CeCu_9In_2$, what corresponds to a paramagnetic state for which the photoemission spectroscopy has been realized.

3. Results and Discussion

3.1. Electrical resistivity

Electrical resistivity of the $CeCu_9In_2$ compound, measured as a function of temperature, exhibits a pronounced anomaly (Fig. 1 a). There is a broad maximum clearly visible at temperature equal to 45 K. At low temperature (T<13 K) resistivity is well described by the quadratic function:

$$\rho = \rho_0 + AT^2. \tag{1}$$

Obtained residual resistivity ρ_0 is equal to 70.10(1) $\mu\Omega{\cdot}$cm, while A coefficient reaches $10.2(2){\cdot}10^{-3}$ $\mu\Omega{\cdot}$cm/K^2. This behavior implies that a coherent Fermi liquid is developed below 13 K in the studied system. Temperature variation of electrical resistivity for $CeCu_9In_2$ is typical of Kondo lattice systems and the broad maximum yields a coherence temperature of $T_{coh}{\approx}45$ K. It should be mentioned that the equation (1) with an additional T^5 term representing phonon scattering was also fitted to experimental data but the quality of the fit did not improve considerably.

We have also measured electrical resistivity of the $LaCu_9In_2$ compound (Fig. 1 b), which has got the same crystal structure as $CeCu_9In_2$. Temperature dependence of electrical resistivity for $LaCu_9In_2$ does not exhibit any pronounced anomaly. Its shape is typical of a simple metal, besides some small concavity, which is most probably due to s-d scattering. We have found that experimental data are described well by the Grneisen–Bloch–Mott model [15, 16]. The fitted function has got the following form:

$$\rho = \rho_0 + c\frac{T}{\theta}\int_0^{\frac{\theta}{T}} \frac{x^5 dx}{(e^x-1)(1-e^{-x})} - KT^3, \tag{2}$$

where: ρ_0 is a residual resistivity, θ denotes the Debye temperature, c is a parameter related to the electron-phonon coupling, while K is the Mott coefficient, which describes the strength of interband s-d scattering. The obtained values of the parameters are as follows: ρ_0=45.33(2) $\mu\Omega{\cdot}$cm, c=82.2(8) $\mu\Omega{\cdot}$cm, θ=189(2) K, K=$1.9{\cdot}10^{-7}$ $\mu\Omega{\cdot}$K$^{-3}{\cdot}$cm.

The measured electrical resistivities of both compounds have been used in order to estimate magnetic contribution of Ce 4f states (ρ_m) to electrical transport in $CeCu_9In_2$. It was obtained by a subtraction of $LaCu_9In_2$ data from those measured for Ce counterpart (Fig. 1 c). The obtained shape is consistent with previous studies of Kondo lattice systems [17]. Beyond the aforementioned broad maximum we have found that logarithmic dependency is

obeyed between 58 K and 165 K. The fit of the formula proposed by J. Kondo:

$$\rho_m = b_1 + b_2 \ln T, \tag{3}$$

yielded b_1=91.1(3) $\mu\Omega$·cm and b_2=-15.54(5) $\mu\Omega$·cm.

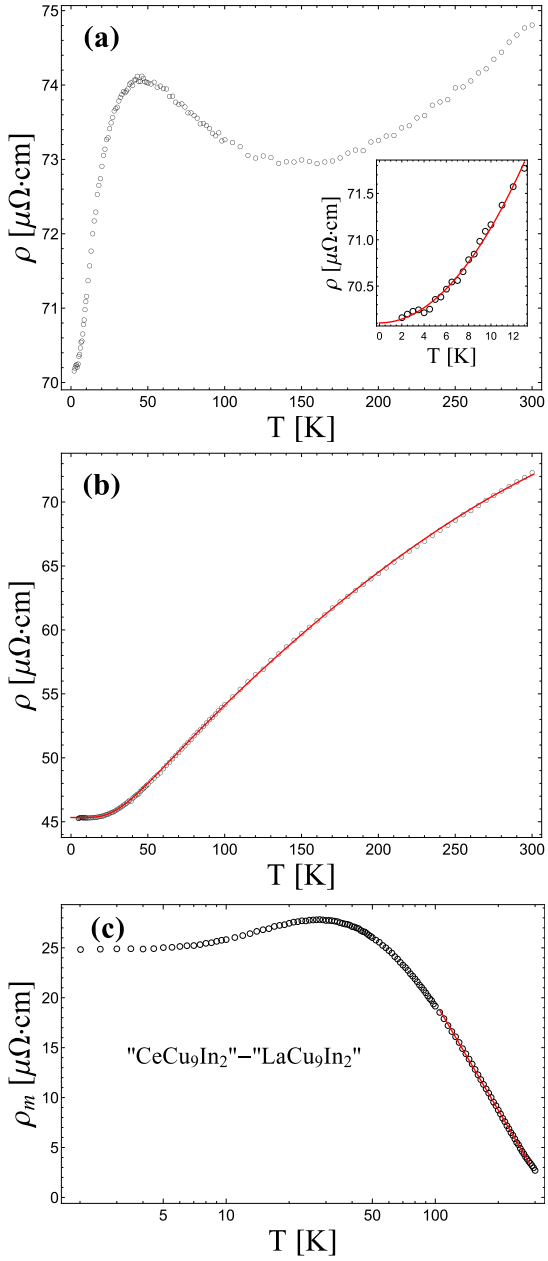

Figure 1: (Color on-line) (a) Temperature variation of the electrical resistivity (black circles) of $CeCu_9In_2$. The red line represents fitted model. Inset: the electrical resistivity at low temperature (2-13 K) with fitted model characteristic of the Fermi liquid (1). (b) Temperature variation of the electrical resistivity (black circles) of $LaCu_9In_2$. The red line represents fitted Grneisen–Bloch–Mott formula (2). (c) Extracted Ce 4f contribution to the electrical resistivity (black circles) of $CeCu_9In_2$ with fitted Kondo law (3) in temperature range 58-165 K.

3.2. Specific heat

The investigated compounds were also subjected to studies of specific heat (Fig. 2). High temperature part of specific heat (Fig. 2 a) for the $CeCu_9In_2$ compound is described well by the sum of lattice contributions (Debye and Einstein models) and electronic part. Namely, we have used the formula:

$$c = \gamma' T + 9kNR\left(\frac{T}{\theta}\right)^3 \int_0^{\frac{\theta}{T}} \frac{x^4 dx}{(e^x-1)^2} + 3(1-k)R\left(\frac{\theta_E}{T}\right)^2 \frac{e^{\frac{\theta_E}{T}}}{\left(e^{\frac{\theta_E}{T}}-1\right)^2}, \tag{4}$$

where: γ' represents a linear term, k is relative weight of Debye and Einstein modes, θ_E is the Einstein temperature, N=12 is the number of atoms in the unit cell, R is the universal gas constant. Obtained values are as follows: θ=246(8) K, γ'=121(8) mJ/(mole·K^2), θ_E=176(129) K, k=0.64(3).

At low temperature, we have plotted c/T versus T^2 (see inset to Fig. 2 a). We have found a linear dependency in the temperature range between 10 K and 20 K. The linear fit yielded γ =132(4) mJ/(mol·K^2), as well as the Debye temperature equal to 107.8 K, which is much lower than the value obtained for high temperature fit to the equation (4). The value of γ is close to γ' resulting from fitting more complex formula (4). Although, the temperatures taken for the linear fit were relatively high for the obtained value of θ [18] the fitted γ is some estimation of Sommerfeld coefficient. Its high value indicates that charge carriers in $CeCu_9In_2$ have got high effective masses. This fact also implies high value of the density of states at the Fermi level.

Significant anomalies are found at low temperature specific heat. Magnetic contribution related to 4f electrons has been estimated (Fig. 2 b) by a subtraction of the specific heat measured for the isostructural $LaCu_9In_2$ compound. One can see three peak-like structures at low temperature. The first one is sharp and located at about 1.6 K (cf. Fig. 2 b). The contribution from the Kondo effect is expected at such temperature. It can be described in terms of the Schotte-Schotte model [19]. It was argued before that such model applies even in a Kondo lattice regime: $Ce_{1-x}La_xNi_2Ge_2$ [20]. The second, broad peak is located roughly at 22 K. According to our knowledge, it is related to crystal field effects, described by the modified Schottky formula [21]. The third, additional λ-type peak at about 7 K is related to the presence of small amount of cerium sesquioxide (Ce_2O_3) [22]. It is known, that cerium ion, confined in symmetry different than cubic, should have crystal field configuration, which consists of three doublets. In $CeCu_9In_2$, Ce atoms occupy 2a site of P4/mbm space group, which is characterized by tetragonal symmetry (site symmetry: 4/m..). However, our data can be described properly by the Schottky formula with a doublet-quartet configuration, which should be observed in case of cubic symmetry. Our attempts of fitting the model with three doublets have led to the results with unreliable coefficients. This discrepancy may be explained by the fact that splitting energy for two doublets is too small to be resolved and therefore a quasi-quartet results from fitting. Similarly, such a quasi-quartet state was observed in case of hexagonal $CeCu_4Al$ [23]. Finally, the fitted model has got a form:

$$c_{4f} = c_{cf} + c_K + \gamma^\star T, \tag{5}$$

where c_{cf} stands for contribution related to crystal field:

$$c_{cf} = \frac{8e^{-\frac{\Delta}{T}} R\Delta^2}{(4+2e^{-\frac{\Delta}{T}})2T^2} \quad (6)$$

(R-universal gas constant, Δ-quartet-doublet splitting), while c_K denotes a contribution related to a Kondo scattering given by the Schotte-Schotte model:

$$c_K = R\frac{T_K}{T\pi}\left[1 - \frac{T_K}{2T\pi}\psi'\left(\frac{1}{2}+\frac{T_K}{2T\pi}\right)\right] \quad (7)$$

(R-universal gas constant, T_K-Kondo temperature, ψ' first derivative of digamma function).

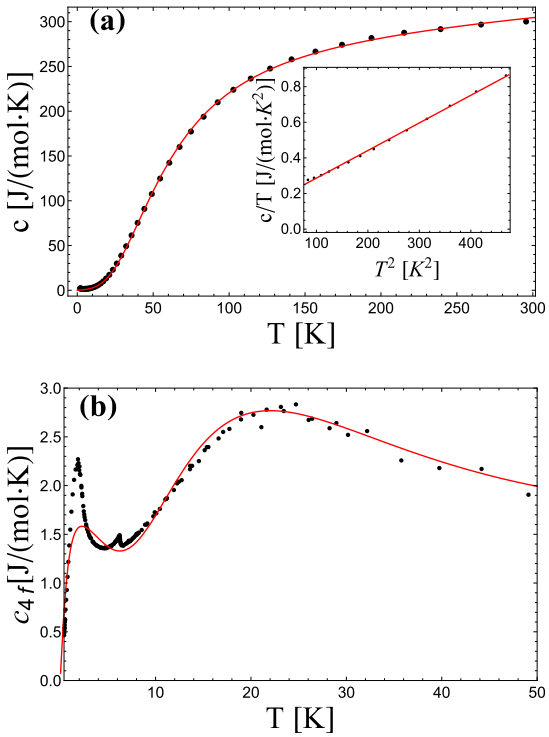

Figure 2: (Color on-line) (a) Specific heat of $CeCu_9In_2$ (black points). Red line is a result of the fitted model (4). Inset: c/T vs T^2 dependency with the fitted line. (b) Magnetic contribution of 4f electrons to the specific heat of $CeCu_9In_2$ (black points). The red line corresponds to the fit of the sum of contributions from the Shotte-Schotte model and the Schottky model (5).

$\gamma^\star$ coefficient obtained from the fit of equation (5) to the data equals 13.4(1.9) mJ/(mole·K^2). Fitting procedure yielded Kondo temperature (T_K) equal to 4.6(3) K and a doublet-quartet splitting Δ equal to 50.2(1.1) K. The effect of correlation between charge carriers is included in both Schotte-Schotte and linear contribution to specific heat. Hence, the value of $\gamma^\star$ is not a good measure of the mass enhancement. Indeed for $T << T_K$ the Schotte-Schotte model can be linearized and its contribution to a linear term is not included in $\gamma^\star$. Therefore the obtained small value of $\gamma^\star$ underestimates the renormalization factor for the electron mass.

One can see that the agreement between the fitted model (eq. 5, cf. Fig. 2 b) and experimental data is not perfect, especially below 6 K. In particular, a phase transition, which has been not considered so far, can be reflected in a peak at 1.6 K. In fact, there are premises, which point to the appearance of the transition to antiferromagnetic state in the $CeCu_9In_2$ compound at low temperature. Namely, these are a negative value of the paramagnetic Curie-Weiss temperature and a significant deviation of magnetic susceptibility from the Curie-Weiss law at low temperature [6]. Magnetic entropy was calculated using estimated Ce 4f contribution to the specific heat. At the temperature of the peak at T =1.6 K it reaches about 45% of a theoretical value $R\ln 2$, corresponding to a doublet ground state. The reduced value of the magnetic entropy points to significance of the Kondo interaction in the studied compound.

3.3. Valence band photoelectron spectra

Many interesting properties of systems with interacting electrons are reflected in the spectral function. In order to study impact of the Kondo effect on the spectral function we have measured UPS spectra of the valence band of the studied compound. One of the fingerprints of the Kondo effect is the Kondo peak. In heavy fermion compounds maximum of the Kondo peak should lie at δ energy above Fermi level according to the Friedel formula [24]:

$$\delta = k_B T_K \sin(\pi n_f), \quad (8)$$

where: n_f is a mean occupation of 4f level, T_K is a Kondo temperature. Usually in photoemission experiments, one can observe only the tail of the Kondo peak, i.e. the peak is sharply cutted by the Fermi edge. The Kondo peak itself is assigned to the $4f^1{}_{5/2}$ final state in the UPS spectra of the valence band. For the parameters corresponding to our study; n_f=0.96, T_K=4.6 K, according to (8) δ is of order of 0.05 meV, which should locate the Kondo peak very close to the Fermi energy.

UPS spectra of the valence band of $CeCu_9In_2$ in vicinity of the Fermi level, measured with He-II and He-I radiation are shown in the Fig. 3 a. In both, He-II and He-I spectra, the tail of the Kondo peak at the Fermi level is not visible. However, in both spectra, one can see some small peak superimposed on the linear slope at binding energy equal to −0.28 eV. This structure can be assigned to $4f^1{}_{7/2}$ final state in the photoemission process. We have estimated 4f contribution to the spectral function of $CeCu_9In_2$ by subtracting He-I from the He-II spectrum [25, 26]. Such 4f spectral weight yields slightly increased intensities near the Fermi energy (E_F) and at −0.28 eV, which are attributed to the $4f^1{}_{5/2}$ and $4f^1{}_{7/2}$ final states, respectively. The intensity near E_F may originate from a Kondo peak, which is hardly visible in this case.

UPS spectra of the valence band of isostructural $LaCu_9In_2$ have also been measured. One can see that He-II spectrum of $LaCu_9In_2$, in contrary to that for $CeCu_9In_2$, is completely featureless in the vicinity of the Fermi level. 4f contribution to the spectral function of $CeCu_9In_2$ has also been estimated by subtracting He-II spectrum for $LaCu_9In_2$ from He-II spectra for $CeCu_9In_2$ (Fig. 3 b). The obtained result is similar to the difference between He-II and He-I spectra for $CeCu_9In_2$. However, in this case the increased intensity near E_F is not well visible. A sharp Kondo peak is not

found. Except for the absence of a sharp, coherent peak at the Fermi level, our spectral function resembles that usually observed for Kondo lattice systems [27].

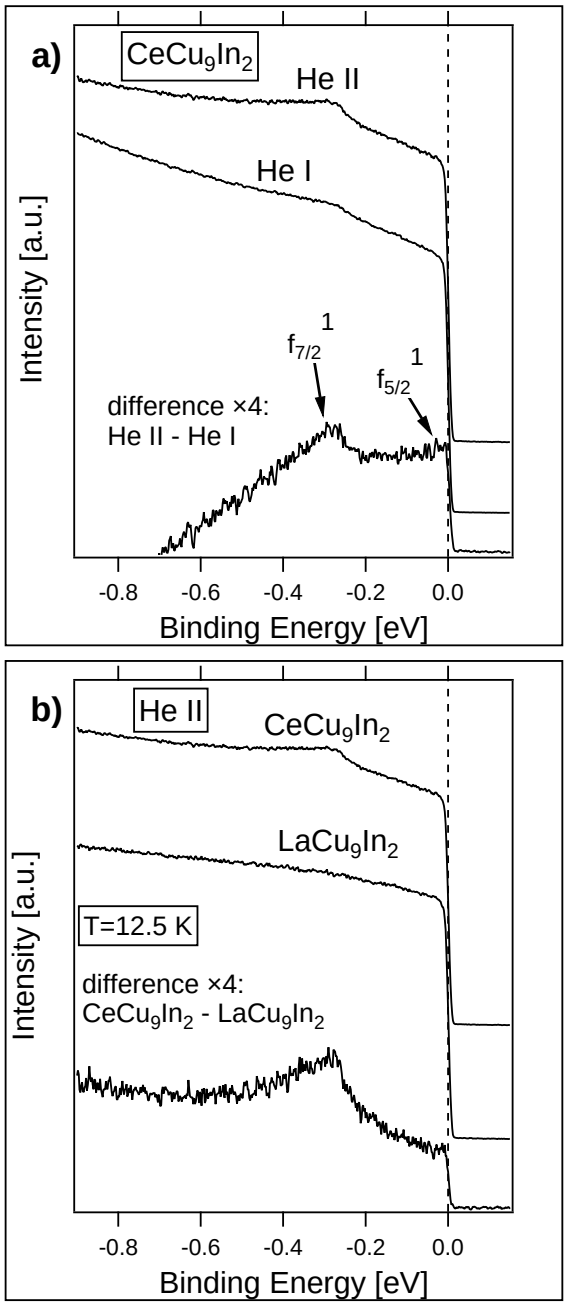

Figure 3: (a) UPS spectra of valence band of $CeCu_9In_2$ obtained with He-II (40.8 eV) and He-I (21.2 eV) radiation at the temperature equal to 12.5 K. 4f contribution to the spectral function, estimated by subtraction of He-I spectrum from He-II spectrum, is presented. Peaks corresponding to the $f^1{}_{7/2}$ and $f^1{}_{5/2}$ final states are marked by arrows. (b) Comparison between $CeCu_9In_2$ and $LaCu_9In_2$ He-II spectra of valence band. The calculated difference is also an estimation of Ce 4f electrons contribution.

There can be several reasons which render difficulty in observation of a Kondo peak. For instance, the applied experimental resolution of 13 meV might be not sufficient to record such a sharp feature. Moreover, polycrystalline samples obtained by arc-melting may exhibit certain disorder in particular at the surface, which can supress spectral intensity at E_F. It is also worth to compare spectra presented here for $CeCu_9In_2$, with those reported previously for $CeNi_9In_2$ [9]. In case of the compound with Ni, the Ni 3d states are located almost at the Fermi level and interact strongly with f states resulting in the mixed valence state. In case of compounds with Cu, the Cu 3d states are rather distant from the Fermi level, making interaction with 4f states weaker and resulting in the Kondo lattice state.

We would like to refer to the results reported previously for $CeCu_6$. This system is an archetypal heavy fermion compound, which displays the Kondo lattice behavior without magnetic ordering down to 5 mK [28, 29]. Specific heat as well as magnetic susceptibility of this compound are enhanced at low temperatures. Its electrical resistivity shows a maximum at low temperature, similarly to our results obtained for $CeCu_9In_2$. Although fingerprints of Kondo lattice state are clearly visible in electronic transport, the influence of the Kondo effect on the UPS spectra of the valence band of $CeCu_6$ is barely seen in certain reports [30, 31]. Namely, in the He-II spectra, there is no any sharp peak at the Fermi level. However, there is a peak visible at the binding energy equal to -0.25 eV, which was attributed to $f^1{}_{7/2}$ final state. According to the results of inelastic neutron scattering experiment [32], the $CeCu_6$ compound has got $T_K = 5$ K. It is commonly believed, that the value of T_K is related to the shape of the UPS spectrum. Namely, the ratio of intensities $I(f^1_{5/2})/I(f^1_{7/2})$ is a monotonic, increasing function of T_K. So, when the T_K is small, the intensity of the Kondo peak with respect to its spin-orbit partner is very low. Some studies of heavy fermion systems with low value of T_K, state that in order to observe the Kondo peak in the UPS spectra, one should measure with resolution less than $k_B T_K$ [33]. This statement was confirmed by recent measurements on $CeCu_6$, in which the authors reported the Kondo peak in the spectra [34, 35]. Possibly, the situation in case of $CeCu_9In_2$ is the same as for $CeCu_6$. Analysis of the specific heat of $CeCu_9In_2$ yields very low value of T_K (about 5 K), and the He-II spectrum resembles the early spectra of $CeCu_6$.

3.4. XPS of Ce 3d levels

Strong Coulomb interaction between 4f electrons and photoholes created in core levels during photoemission process leads to characteristic satellite structure of the XPS spectrum of Ce 3d levels. Each spin orbit partner in 3d doublet splits into three satellites corresponding to different numbers of electrons on the f shell in the final state of photoemission process. Fitting procedure applied together with the so called Gunnarsson-Schönhammer theory [36, 37] allows to estimate parameters such as a mean occupation of 4f shell, as well as the strength of the coupling between conduction band and 4f level.

XPS spectrum of Ce 3d levels of $CeCu_9In_2$ is shown in the Fig. 4. Peak deconvolution and numerical analysis can be based on the Doniach-Šunjić theory [38]. The background has been simulated with application of the Shirley method [39]. Peaks corresponding to the Ce $3d_{5/2}$ and Ce $3d_{3/2}$ levels are clearly visible. They are separated by spin-orbit splitting equal to 18.5 eV. Each component of

the doublet is further splitted due to the hybridization effects. Namely, each component of the doublet consists of three satellite lines: f^0, f^1 and f^2. The $3d^94f^0$ component is an evidence of the intermediate valence state of cerium ions, while the $3d^94f^2$ component gives information about the hybridization between 4f states and conduction electron states. Locations as well as intensities of particular peaks are collated in Table 1.

Table 1: Binding energies (E_B) and relative intensities (I) of satellite lines in XPS spectra of Ce 3d levels. We present results obtained for the $3d_{5/2}$ component. Spin-orbit splitting is equal to 18.5 eV.

$3d_{5/2}$	f^0	f^1	f^2
E_B [eV]	897.45	884.50	881.97
I [a.u.]	0.06	1	0.37

Satellites corresponding to the f^0 and f^2 final states are not fully resolved — they are visible as shoulders of the intense f^1 line. According to the theoretical model [36, 37], the intensity ratio $r_1 = I(f^0)/[I(f^0)+I(f^1)+I(f^2)]$ yields information about the occupation of Ce 4f shell $n_f = 1 - r_1$. We have obtained the value n_f=0.96. The hybridization energy can be estimated from the ratio $r_2 = I(f^2)/[I(f^1)+I(f^2)]$. The value of r_2 equal to 0.27 corresponds to the hybridization energy equal to 139 meV.

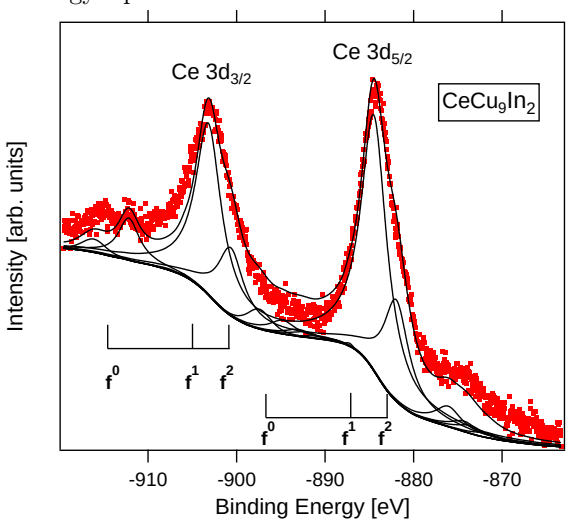

Figure 4: (Color on-line) XPS spectra of the Ce 3d levels in $CeCu_9In_2$ obtained with Mg K_α radiation at the temperature equal to 12.5 K. Experimental data are denoted by red dots, while solid black lines correspond to the fitted model.

3.5. Theoretical calculations

Theoretical calculations have been performed in order to get insight into the electronic structure of the studied compounds and to have a comparison with our experimental results. Total and partial densities of states, calculated for $LaCu_9In_2$ and $CeCu_9In_2$ with application of FPLO code, are shown in Fig. 5. In case of $CeCu_9In_2$ densities of states have been calculated within two computational schemes: without interaction between f electrons (U=0 eV, Fig. 5 b) and with Coulomb repulsion on 4f shell (U=2 eV not shown, U=6 eV, Fig. 5 c).

Density of states in the valence band of $LaCu_9In_2$ is dominated by the Cu 3d states (Fig. 5 a). There is some humped structure build up from those states, mostly located between −5 eV and −1 eV. In the vicinity of the Fermi level, La 5d, In 5s and 5p states contribute to the total density of states. La 5d states extend mostly above the Fermi level, while In 5s and 5p are rather smeared over the whole valence band.

In case of $CeCu_9In_2$ we have performed calculations for different values of Coulomb repulsion (U) between electrons on 4f shell. Densities of states calculated for U=0 eV, are symmetric and one can notice that for Cu and In, they are roughly the same as in case of the compound with La. In partial density originating from Ce, contribution from 4f orbital character is very significant. Namely, there is a sharp peak, located at about 0.3 eV above the Fermi level. For U=6 eV the density of states is considerably modified. While the partial densities of states related to Cu and In remain roughly unchanged, there is an important change in case of partial Ce 4f DOS. This quantity is not symmetric with respect to the spin degrees of freedom. One can see that, for arbitrary chosen, "up" component of the spin, 4f DOS has two dominating structures. The first one is the peak at binding energy equal to −4 eV, the second one is the peaked structure, which is located above the Fermi level. The maximum of the latter structure is at about 2 eV. 4f DOS related to "down" component of the spin has got only one, hump-like structure. This feature lies above the Fermi level, with the maximum at about 1.7 eV. The asymmetry of the 4f, as well as total DOS, can lead to a presence of some spontaneous magnetic moment in the ground state of the $CeCu_9In_2$ compound. We have also performed calculation for U=2 eV, however they are not qualitatively different from those for U=0 eV.

The band dispersion along some high symmetry lines inside first Brillouin zone (BZ) (Fig. 6), as well as FS (Fig. 7), have been calculated for $CeCu_9In_2$ and $LaCu_9In_2$. For both compounds, calculations have been done under assumption of non-magnetic ground state. One can notice, that far from the Fermi level, the bands have got similar dependency on the **k**-vector. In the band structure of $CeCu_9In_2$, one can observe some structures which are absent in case of $LaCu_9In_2$. These are six flat bands visible above the Fermi level. They extend from about 0.2 eV to about 0.4 eV above the Fermi level. These states are mostly related to 4f orbital character. So, according to the theoretical calculations, 4f states in $CeCu_9In_2$ are not localized and are characterized by large effective masses. For both compounds one can observe some broad hole pocket around the center of the Γ-Z line. Beyond this fact, the band structure in the vicinity of the Fermi level is quite different for studied compounds and this fact is reflected in the calculated FS. FS (Fig. 7) of both compounds is strongly anisotropic. In case of $LaCu_9In_2$ 4 bands contribute to FS, while in case of $CeCu_9In_2$ there are only 3 bands which cross the Fermi level. For the compound with La, one can see a feature in the center of BZ (around the Γ point) flattened in the direction perpendicular to $\mathbf{c}^\star$. This structure is surrounded, symmetrically in the $\mathbf{c}^\star$ direction, by highly corrugated leaf-like structures. In case of

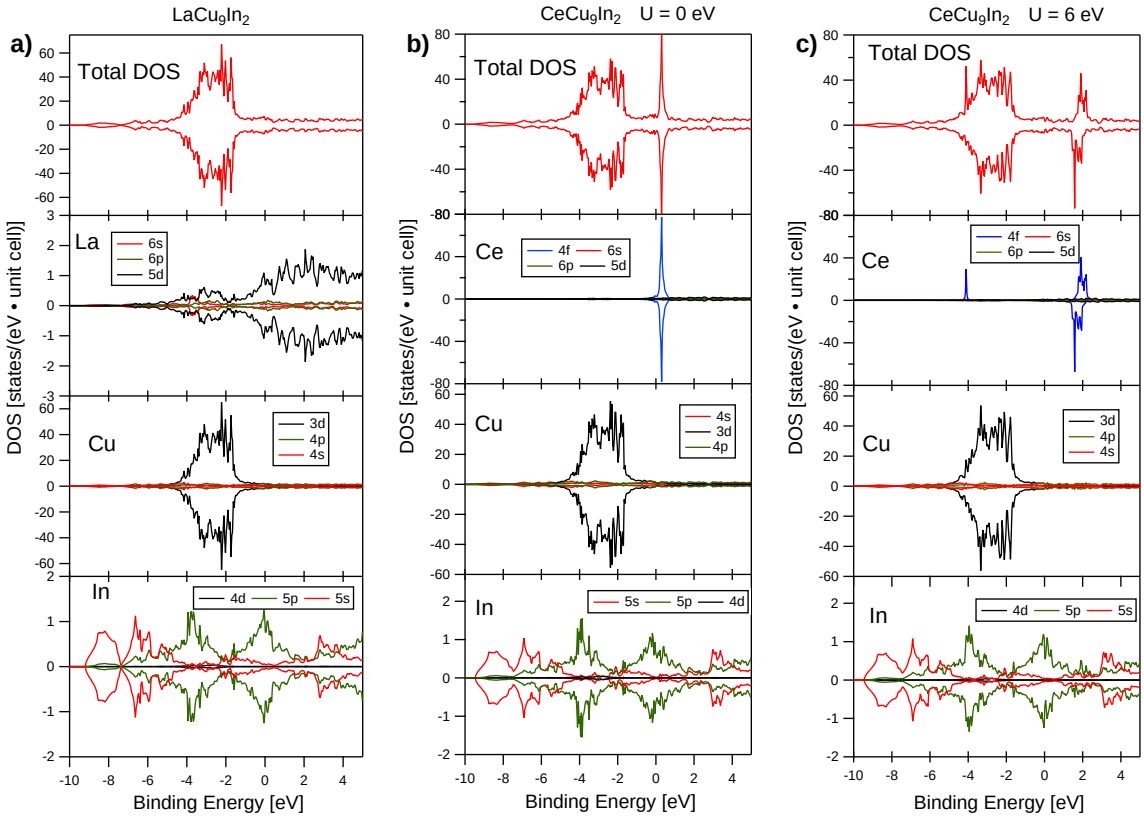

Figure 5: (Color on-line) Total and partial densities of states calculated with application of FPLO code for (a) $LaCu_9In_2$ and (b) $CeCu_9In_2$ without (U =0 eV) and (c) with (U =6 eV) additional correlations. Opposite spin directions are marked by positive and negative values of density of states.

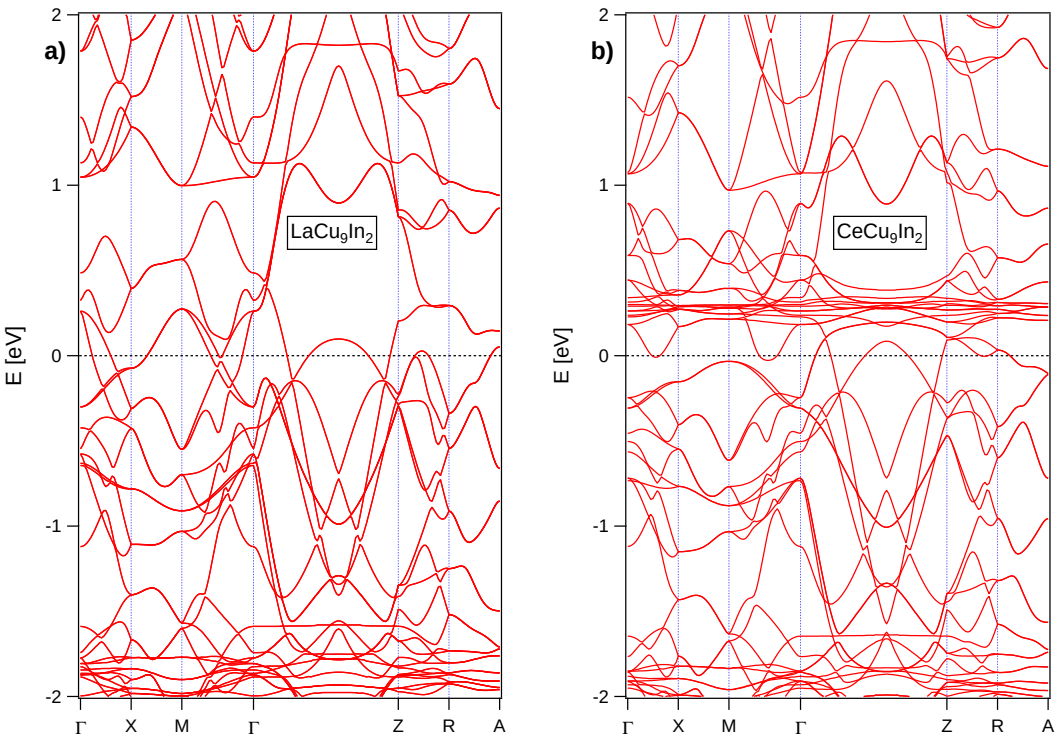

Figure 6: (Color on-line) Ground state band structures of (a) $LaCu_9In_2$ and (b) $CeCu_9In_2$, calculated with application of Elk code. Non-magnetic ground state has been assumed.

$CeCu_9In_2$, there is a structure in the center of BZ, which resembles a doughnut which is flattened also in the direction perpendicular to $\mathbf{c}^\star$. Moreover, one can see some almost flat parallel sheets of FS, which are perpendicular to $\mathbf{c}^\star$. This fact can be interpreted as an existence of FS nesting in $CeCu_9In_2$.

We have computed the Sommerfeld coefficient (γ_{theor}) with application of formula derived on the basis of free electron theory using calculated total densities of states at the Fermi level ($D(E_F)$) according to the equation [40]:

$$\gamma_{theor} = \frac{k_B^2 \pi^2}{3} D(E_F) \tag{9}$$

The obtained values of the γ_{theor} coefficient are collated in the Table 2.

One can notice, that in case of $LaCu_9In_2$, the value of γ_{theor} is in perfect agreement with the experimental one. This means that electrons in this compound are not strongly correlated and can be properly described with application of DFT based methods. On the contrary, in case of $CeCu_9In_2$, there is a large discrepancy between γ_{theor} and the experimental one. Even the introduction of correlation between 4f electrons in the mean-field level does not lead to improvement of agreement between theory and experiment. It rather leads to greater discrepancy, than in case with U=0. It can be explained as follows. For U=0 eV, DOS is symmetric with respect to the spin, and one can observe some peak-like structure in Ce 4f partial DOS, which has got a maximum above the Fermi level. However, there is some non-zero density of states at the Fermi level, because of the finite width of this structure. When Coulomb repulsion on the f shell is slightly higher than 0, then this peak moves above the Fermi level (calculations for U=2 eV are not shown), which corresponds to decrease of DOS at E_F and finally to smaller value of γ_{theor}, while the actual value of γ is enhanced by the correlation effects. Moreover, increase of U leads to splitting of the peak in vicinity of the Fermi level into two peaks because lower and higher Hubbard bands are formed. The first one is located below E_F, while the second one is placed above the Fermi level. Similar situation was observed previously in case of the $CeNi_9In_2$ compound [9]. Discrepancy between theoretical and experimental value of Sommerfeld coefficient of $CeCu_9In_2$ is not startling for us and it testifies presence of strong correlations in this compound.

4. Conclusions

In order to characterize the properties of the $CeCu_9In_2$ system we performed experimental studies of electrical resistivity, specific heat and electronic structure. The data are complemented by DFT calculations. To separate an effect of 4f electrons similar studies have been realized for the isostructural $LaCu_9In_2$ reference compound. The results indicate that $CeCu_9In_2$ is a Kondo lattice system with the coherence temperature T_{coh}=45 K and Kondo temperature $T_K \approx$5 K. Transition to the AFM state is anticipated at T =1.6 K. Properties of a Fermi liquid are observed at low temperatures. Lattice vibrations, Kondo effect, crystal field splitting and magnetism contribute to specific heat. Crystal field energy level scheme for $CeCu_9In_2$ is of the doublet-quartet type with splitting energy Δ =50.2(1.1) K. Low temperature linear dependence of specific heat yields relatively high Sommerfeld coefficient of 132(4) mJ/(mole·K^2) what points to the enhancement of the effective mass of charge carriers. Another effects of coupling between 4f electrons and conduction band are visible in the 3d core level XPS spectra and in UPS spectra of valence band. The Kondo peak, which is assigned usually to the $4f^1{}_{5/2}$ final state is not visible in raw UPS data. However, increased spectral intensity near E_F is found in the extracted spectral contribution from 4f electrons. We have observed peak at binding energy equal to -0.25 eV, which is related to the $4f^1{}_{7/2}$ final state. Theoretical calculations predict nesting of FS in case of $CeCu_9In_2$.

Acknowledgement

This work has been supported by the National Science Centre, Poland within the Grant no. 2016/23/N/ST3/02012. Support of the Polish Ministry of Science and Higher Education under the grant 7150/E-338/M/2018 is acknowledged. We are grateful to M. Rams for measurements of specific heat at low temperature (0.4–10 K). The research was carried out with the equipment purchased thanks to the financial support of the European Regional Development Fund in the framework of the Polish Innovation Economy Operational Program (contract no. POIG.02.01.00-12-023/08).

References

[1] Y. M. Kalychak, V. I. Zaremba, R. Pöttgen, M. Lukachuk, R.-D. Hoffmann, Rare earthtransition metalindides, Vol. 34 of Handbook on the Physics and Chemistry of Rare Earths, Elsevier, 2004, pp. 1–133. doi:10.1016/S0168-1273(04)34001-8.

[2] I. Bigun, M. Dzevenko, L. Havela, Ya. M. Kalychak, in: Solid Compounds of Transition Elements II, Vol. 194 of Solid State Phenomena, Trans Tech Publications, 2013, pp. 45–49. doi:10.4028/www.scientific.net/SSP.194.45.

[3] I. Bigun, M. Dzevenko, L. Havela, Ya. M. Kalychak, Eur. J. Inorg. Chem. 16 (2014) 2631–2642. doi:10.1002/ejic.201400058.

[4] V. M. Baranyak, Ya. M. Kalychak, Neorg. Mater. 27 (6) (1991) 1235–1238.

[5] Ya. M. Kalychak, Izv. AN SSSR, Metally 4 (1998) 110–118.

[6] S. Baran, J. Przewonik, Ya. M. Kalychak, Yu. Tyvanchuk, A. Szytuła, J. Magn. Magn. Mater. 410 (2016) 156–164. doi:10.1016/j.jmmm.2016.03.009.

[7] O. Moze, S. Mentink, G. Nieuwenhuys, K. Buschow, J. Magn. Magn. Mater. 150 (3) (1995) 345–348. doi:10.1016/0304-8853(95)00297-9.

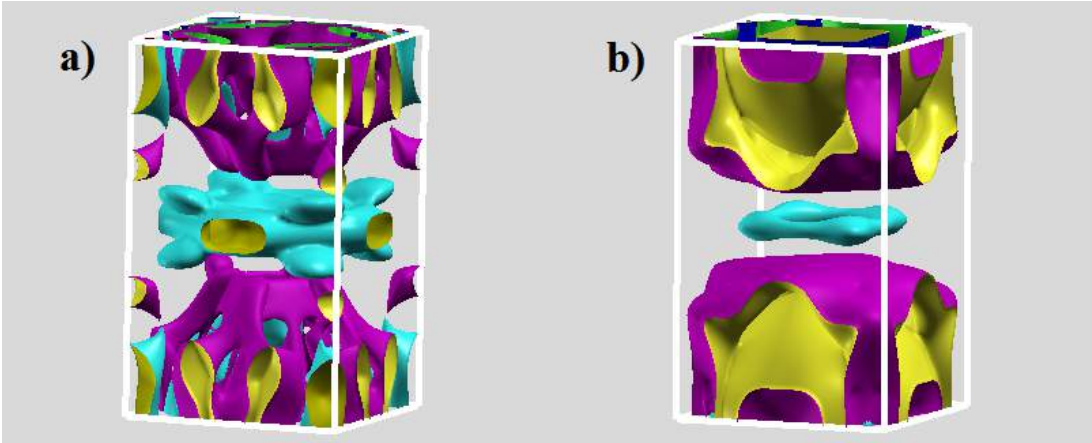

Figure 7: (Color on-line) Fermi surface of (a) $LaCu_9In_2$ and (b) $CeCu_9In_2$, calculated with application of Elk code. Non-magnetic ground state has been assumed.

Table 2: Comparison between experimental (γ_{exp}) and theoretical (γ_{theor}) values of the Sommerfeld coefficient for $LaCu_9In_2$ and $CeCu_9In_2$.

	U [eV]	γ_{theor} [mJ/(mole·K^2)]	γ_{exp} [mJ/(mole·K^2)]
$LaCu_9In_2$	0	14.08	14.0(1)
	0	19.76	
$CeCu_9In_2$	2	19.69	132(4)
	6	13.61	

[8] A. Szytuła, S. Baran, B. Penc, J. Przewonik, A. Winiarski, Yu. Tyvanchuk, Ya. M. Kalychak, J. Alloy. Compd. 589 (2014) 622–627. doi:10.1016/j.jallcom.2013.12.012.

[9] R. Kurleto, P. Starowicz, J. Goraus, S. Baran, Yu. Tyvanchuk, Ya. M. Kalychak, A. Szytuła, Solid State Commun. 206 (2015) 46–50. doi:10.1016/j.ssc.2015.01.014.

[10] K. Koepernik, H. Eschrig, Phys. Rev. B 59 (1999) 1743–1757. doi:10.1103/PhysRevB.59.1743.

[11] V. I. Anisimov, I. V. Solovyev, M. A. Korotin, M. T. Czyżyk, G. A. Sawatzky, Phys. Rev. B 48 (1993) 16929–16934. doi:10.1103/PhysRevB.48.16929.

[12] J. P. Perdew, Y. Wang, Phys. Rev. B 45 (1992) 13244–13249. doi:10.1103/PhysRevB.45.13244.

[13] D. M. Ceperley, B. J. Alder, Phys. Rev. Lett. 45 (1980) 566–569. doi:10.1103/PhysRevLett.45.566.

[14] [link].
URL http://elk.sourceforge.net/

[15] N. F. Mott, H. Jones, The Theory of the Properties of Metals and Alloys, Oxford University Press, London, 1958.

[16] G. Grimvall, The Electron-Phonon Interaction in Metals, North-Holland Pub. Co., Amsterdam, 1981.

[17] M. Szlawska, D. Kaczorowski, Phys. Rev. B 85 (2012) 134423. doi:10.1103/PhysRevB.85.134423.

[18] V. H. Tran, Phys. Rev. B 70 (2004) 094424. doi:10.1103/PhysRevB.70.094424.

[19] K. Schotte, U. Schotte, Phys. Lett. A 55 (1) (1975) 38–40. doi:10.1016/0375-9601(75)90386-2.

[20] A. P. Pikul, U. Stockert, A. Steppke, T. Cichorek, S. Hartmann, N. Caroca-Canales, N. Oeschler, M. Brando, C. Geibel, F. Steglich, Phys. Rev. Lett. 108 (2012) 066405. doi:10.1103/PhysRevLett.108.066405.

[21] M. d. Souza, R. Paupitz, A. Seridonio, R. E. Lagos, Braz. J. Phys. 46 (2) (2016) 206–212. doi:10.1007/s13538-016-0404-9.

[22] M. E. Huntelaar, A. S. Booij, E. H. P. Cordfunke, R. R. van der Laan, A. C. G. van Genderen, J. C. van Miltenburg, J. Chem. Thermodynamics 32 (2000) 465–482. doi:10.1006/jcht.1999.0614.

[23] T. Toliński, A. Hoser, S. Rols, A. Kowalczyk, A. Szlaferek, Solid State Commun. 149 (47) (2009) 2240–2243. doi:10.1016/j.ssc.2009.09.002.

[24] A. Georges, C. R. Phys. 17 (3) (2016) 430–446. doi:10.1016/j.crhy.2015.12.005.

[25] J. J. Yeh, Atomic Calculation of Photoionization Cross-Sections and Asymmetry Parameters, Gordon and

Breach Science Publishers, Langhorne, PE (USA), 1993.

[26] J. J. Yeh, I. Lindau, Atomic Data and Nuclear Data Tables 32 (1) (1985) 1–155. doi:10.1016/0092-640X(85)90016-6.

[27] P. Starowicz, R. Kurleto, J. Goraus, H. Schwab, M. Szlawska, F. Forster, A. Szytuła, I. Vobornik, D. Kaczorowski, F. Reinert, Phys. Rev. B 89 (2014) 115122. doi:10.1103/PhysRevB.89.115122.

[28] G. R. Stewart, Z. Fisk, M. S. Wire, Phys. Rev. B 30 (1984) 482–484. doi:10.1103/PhysRevB.30.482.

[29] Y. nuki, Y. Shimizu, M. Nishihara, Y. Machii, T. Komatsubara, J. Phys. Soc. Jpn. 54 (5) (1985) 1964–1974. doi:10.1143/JPSJ.54.1964.

[30] F. Patthey, W. D. Schneider, Y. Baer, B. Delley, Phys. Rev. B 34 (1986) 2967–2970. doi:10.1103/PhysRevB.34.2967.

[31] F. Patthey, J.-M. Imer, W.-D. Schneider, H. Beck, Y. Baer, B. Delley, Phys. Rev. B 42 (1990) 8864–8881. doi:10.1103/PhysRevB.42.8864.

[32] E. A. Goremychkin, R. Osborn, Phys. Rev. B 47 (1993) 14580–14583. doi:10.1103/PhysRevB.47.14580.

[33] M. Garnier, K. Breuer, D. Purdie, M. Hengsberger, Y. Baer, B. Delley, Phys. Rev. Lett. 78 (1997) 4127–4130. doi:10.1103/PhysRevLett.78.4127.

[34] D. Ehm, F. Reinert, J. Kroha, O. Stockert, S. Hüfner, Acta Phys. Pol. B 34 (2003) 951–954.

[35] D. Ehm, S. Hüfner, F. Reinert, J. Kroha, P. Wölfle, O. Stockert, C. Geibel, H. v. Löhneysen, Phys. Rev. B 76 (2007) 045117. doi:10.1103/PhysRevB.76.045117.

[36] J. C. Fuggle, F. U. Hillebrecht, Z. Zołnierek, R. Lässer, C. Freiburg, O. Gunnarsson, K. Schönhammer, Phys. Rev. B 27 (1983) 7330–7341. doi:10.1103/PhysRevB.27.7330.

[37] O. Gunnarsson, K. Schönhammer, Phys. Rev. B 28 (1983) 4315–4341. doi:10.1103/PhysRevB.28.4315.

[38] S. Doniach, M. Šunjić, J. Phys. C Solid State 3 (2) (1970) 285–291. doi:10.1088/0022-3719/3/2/010.

[39] D. A. Shirley, Phys. Rev. B 5 (1972) 4709–4714. doi:10.1103/PhysRevB.5.4709.

[40] C. Kittel, Introduction to Solid State Physics, John Wiley and Sons, Inc., United States, 1996.

Chapter 7

Studies of Electronic Structure across a Quantum Phase Transition in $CeRhSb_{1-x}Sn_x$

R. Kurleto, J. Goraus, M. Rosmus, A. Ślebarski, and P. Starowicz, The European Physical Journal B **92**, 192 (2019). doi: 10.1140/epjb/e2019-100157-3

Highlights

- $CeRhSb_{1-x}Sn_x$ is a Kondo insulator for $x < 0.13$ and a weakly magnetic non-Fermi liquid for $x > 0.13$, $x = 0.13$ corresponds to a quantum critical transition
- sharp peak at the Fermi level ($4f^1_{5/2}$ final state) is not visible in photoemission spectra, while the structure corresponding to $4f^1_{5/2}$ final state is clearly visible in measurements for each studied composition
- observed shifts of the band structure as a function of x agree with the hole doping scenario, both in experiment and ab initio calculations
- however, there are some deviations from a simple rigid band shift scenario
- ab initio calculations predict that the hole doping induces a series of modifications of the Fermi surface topology (Lifshitz transitions)

Eur. Phys. J. B
This is a post-peer-review, pre-copyedit version of this article.
The final version is available online at: https://doi.org/10.1140/epjb/e2019-100157-3.

arXiv:1910.07967v2 [cond-mat.str-el] 11 Mar 2020

Studies of Electronic Structure across a Quantum Phase Transition in $CeRhSb_{1-x}Sn_x$

R. Kurleto[1], J. Goraus[2], M. Rosmus[1], A. Ślebarski[2], P. Starowicz[a,1]

[1]Marian Smoluchowski Institute of Physics, Jagiellonian University, Łojasiewicza 11, 30-348 Kraków, Poland
[2]Institute of Physics, University of Silesia, ul. 75 Pułku Piechoty 1A, 41-500 Chorzów, Poland

Published in Eur. Phys. J. B, September 2019

Abstract We study an electronic structure of $CeRhSb_{1-x}Sn_x$ system, which displays quantum critical transition from a Kondo insulator to a non-Fermi liquid at $x = 0.13$. We provide ultraviolet photoelectron spectra of valence band obtained at 12.5 K. A coherent peak at the Fermi level is not present in the data, but a signal related to $4f^1{}_{7/2}$ final state is detected. Spectral intensity at the Fermi edge has a general tendency to grow with Sn content. Theoretical calculations of band structure are realized with full-potential local-orbital minimum-basis code using scalar relativistic and full relativistic approach. The calculations reveal a depletion of density of states at the Fermi level for CeRhSb. This gap is shifted above the Fermi energy with increasing Sn content and thus a rise of density of states at the Fermi level is reflected in the calculations. It agrees with metallic properties of compounds with larger x. The calculations also yield another important effects of Sn substitution. Band structure is displaced in a direction corresponding to hole doping, although with deviations from a rigid band shift scenario. Lifshitz transitions modify a topology of the Fermi surface a few times and a number of bands crossing the Fermi level increases.

1 Introduction

Quantum phase transition (QPT) is a matter of particular interest because it is related to an instability of a ground state [1–3]. Heavy fermions are a perfect playground for studying quantum criticality. The transition from one to another type of the ground state is associated with non-Fermi liquid behavior. Quantum critical point (QCP) which separates metallic phase from so called Kondo insulator (KI) has attracted particular attention so far [4–6]. KIs are materials with a narrow gap or a pseudogap in an electronic structure, which opens due to hybridization between correlated electrons and conduction band [6–8].

$CeRhSb_{1-x}Sn_x$ is an example of the system with QCP. Representatives of $CeRhSb_{1-x}Sn_x$ system crystallize in orthorombic ε-TiNiSi structure (Pnma space group) for $x < 0.2$

[a]e-mail: pawel.starowicz@uj.edu.pl

and in hexagonal Fe_2P (P62m space group) for $x > 0.8$ [9–11]. In case of $0.2 \leq x \leq 0.8$ phase separation occurs. The parent compound, CeRhSb, is a KI with a gap width equal to approximately 7 K [8, 9, 12]. Doping with Sn, which is equivalent to increasing concentration of holes, leads to a gradual closing of the gap [13]. The gap disappears at $x = x_c = 0.13$, which is associated with QCP [6]. For $x > x_c$ the system becomes metallic with non-Fermi liquid ground state [9, 14]. Thorough studies of physical properties of $CeRhSb_{1-x}Sn_x$ in the vicinity of the transition have been made so far [6, 8, 12]. According to them a universal scaling law $\rho \cdot \chi$ =const (ρ - electrical resistivity, χ - magnetic susceptibility) is obeyed in KI phase ($x < 0.13$) [9]. A singular behavior of magnetic susceptibility was observed for $x > x_c$, which is related to a non-Fermi liquid formation [14]. At a higher value of temperature there is a crossover from a non-Fermi-liquid to a Fermi liquid [6]. Strong valence fluctuations have been found in all synthesized representatives of $CeRhSb_{1-x}Sn_x$ system [12]. Such instabilities of Ce valency are believed to play an important role in the pseudogap formation for $x < x_c$ [15].

Photoelectron spectroscopy (PS) combined together with theoretical modeling of a band structure is a powerful tool in studying effects of hybridization in heavy electrons systems. Several studies devoted to the electronic structure of KIs have been conducted with application of PS, so far [16–19]. Particularly, the abrupt step behavior of the single ion Kondo scale (T_K) at a critical point has been inferred from photoemission data [19].

Both, CeRhSb and CeRhSn compounds were studied with application of PS. In case of CeRhSn [20, 21], an enhancement of signal attributed to $4f^1{}_{5/2}$ final state, together with a small intensity of $4f^0$ feature was interpreted as a symptom of valence fluctuations [20, 21]. Valence band (VB) spectra of CeRhSb obtained previously show not only characteristics of a cerium compound with Kondo effect: f^0, $f^1_{5/2}$ and $f^1_{7/2}$ features but also a depletion of the spectral weight at ε_F due to the hybridization gap formation below 120 K [22–25].

Transition from KI in CeRhSb to a metallic state in CeRhSn via the critical point was studied by means of density functional theory (DFT) calculations before [26]. It was shown that QPT is manifested by a change of Mulliken occupation of Ce 5d states as a function of x. Indeed, DFT calculations properly reproduced experimental value of critical Sn concentration (x_c=0.13) and it was testified that atomic disorder is not a necessary factor for the formation of QCP. However, such a disorder leads to the Griffiths phase, which was evidenced for CeRhSn [13, 14, 20, 27]. The schematic phase diagram of $CeRhSb_{1-x}Sn_x$ system in $T - x$ plane has been proposed so far [9]. The metallization of a system was explained in terms of the model, which takes into account both, itinerant character of Ce 4f electrons and collective Kondo singlet state. A transition from KI to metallic state is related to destruction of such a collective singlet state accompanied by delocalization of 4f electrons.

In this paper we present studies of the electronic structure of $CeRhSb_{1-x}Sn_x$ performed as a function of hole doping x in a light of QPT. VB spectra collected with application of PS are confronted with the results of theoretical modelling. DFT calculations show that the increase of Sn content in $CeRhSb_{1-x}Sn_x$ results in a growth of density of states at the Fermi energy (ε_F), which is observed also in the experiment.

The theoretical results also yield a sequence of Lifshitz transitions in Fermi surface and band structure.

2 Material and methods

Description of synthesis and characterization of polycrystalline samples of $CeRhSb_{1-x}Sn_x$ ($x = 0$, 0.06, 0.16, 1) was provided elsewhere [6, 13]. The quality of used samples was checked with application of x-ray diffraction and energy dispersive x-ray spectroscopy (EDXS). Diffraction patterns testified that the specimens subjected to the scrutiny consist of single phase. Good homogenity of samples was proven by means of EDXS. The ultraviolet photoemission spectroscopy (UPS) data have been collected with application of a VG Scienta R4000 photoelectron energy analyzer. Measurements have been conducted at temperature equal to 12.5 K. Both, He II (40.8 eV) and He I (21.2 eV) radiation have been used. Base pressure in the analysis chamber was equal to $4{\cdot}10^{-11}$ mbar. Specimens were cleaned with diamond file in the preparation chamber (base pressure $4{\cdot}10^{-10}$ mbar) prior to the measurement. For comparison we also made measurements on samples which were cleaved in the ultra-high vacuum conditions, but results obtained in this way have got worse quality. Overall resolution was not greater than 30 meV.

Partial densities of states (DOSes) have been simulated with application of full-potential local-orbital (FPLO) package [28–33]. Calculations in scalar relativistic scheme were performed with the virtual crystal approximation. Irreducible Brillouin zone (BZ) was divided for 343 k-points. Perdew-Wang exchange correlation potential was used. Partial DOSes, band structure along high symmetry directions in the first BZ and Fermi surfaces have been resolved also with application of FPLO code in full relativistic approach.

Photoelectron spectra have been simulated using calculated partial DOSes and assuming atomic cross sections for photoionization [34]. Experimental broadening has been introduced by a convolution with the gaussian function of the width of 10 meV.

3 Results and Discussion

3.1 Photoemission - wide energy range

Spectra of $CeRhSb_{1-x}Sn_x$ measured in a wide range of binding energy (ε_B) are presented in Fig. 1 a. Sn $4d_{5/2}$ and $4d_{3/2}$ core levels have been observed at ε_B equal to -24.74 eV and -23.7 eV, respectively, for compounds with $x \neq 0$, in He II spectra. Ce 5p doublet is visible for each investigated specimen. It consists of a humped structure at $\varepsilon_B \approx -21$ eV, followed by a broad peak at -17.9 eV. This last structure was used for normalization of the He II spectra, together with a guide served by Sn 4d core levels. A broad peak-like feature has been observed at $\varepsilon_B \approx -10$ eV except for the compound without Sb. Signal in this energy region observed for CeRhSn is completely flat, so we can attribute this structure to Sb derived states. In fact, the position of the maximum corresponds to the Sb 5s states.

3.2 Photoemission - valence band

Spectra of investigated compounds have got similar shape in VB region (inset to Fig. 1 a). There are two, broad and intense humps ($\varepsilon_B \approx -5.2$ eV, -2.1 eV) and a small blurred peak close to ε_F in He II measurements. The last structure ($\varepsilon_B \approx -0.3$ eV) is related to Ce 4f electrons, because it is suppressed in He I spectra (discussed below). Locations and mutual ratio of intensities of ascribed structures depend on x. The peak corresponding to higher absolute value of ε_B is located at about -5.16 eV in case of CeRhSb and remains in the same position for $CeRhSb_{0.94}Sn_{0.06}$, while in case of CeRhSn and $CeRhSb_{0.84}Sn_{0.16}$ it is found at about -5.25 eV. This effect may be connected with a small contribution from Sn p and d states. The second structure also displays a weak dependency on x. This maximum occupies roughly the same position, equal to -2.1 eV, for three samples with Sb, while for CeRhSn it moves to -2.3 eV. Intensity taken at maximum at ≈ -2.1 eV divided by intensity taken at second maximum amounts to 1.1, 1.3, 0.98 and 1.8 for $x = 0$, 0.06, 0.16 and 1 respectively. The values obtained for CeRhSn differ from these obtained for other studied compounds, which is not startling, because CeRhSn adopts a different crystal structure. Hence, it should have a different electronic structure as well.

Shape of VB spectra obtained with application of He I radiation (also shown in the inset to Fig. 1 a) corresponds to the data recorded with He II lamp with two major peaks observed at similar binding energies. The spectrum is mainly related to Rh 4d states, what is supported by theoretical calculations discussed further in the text. This is also consistent with previous PS measurements and theoretical calculations performed for metallic Rh [35, 36]. The maximum for CeRhSb is located at -2.1 eV and a small amount of the dopant ($x = 0.06$) shifts the peak towards ε_F, next for $x = 0.16$ the maximum is displaced in opposite direction and finally for CeRhSn its binding energy is -2.33 eV. These results would suggest a non-monotonic dependence with respect to x. However, these displacements are very close to experimental uncertainty. He-II spectra do not follow well these trends.

High resolution measurements of vicinity of ε_F are shown in Fig. 1 b. Spectra measured with application of He II are compared with those obtained with He I. In He II data one can see a broad maximum at about -0.3 eV which is superimposed on a linear signal. The slope of measured intensity of He I spectra changes as well. However, for He I excited photoemission a broad hump near -0.3 eV is visible only for CeRhSn.

3.3 Ce 4f spectral function

Cross section for photoionization of Ce 4f electrons is amplified over three times when one goes from He I to He II [37], so we can estimate 4f contribution to spectral function by subtracting high resolution measurements: He I from He II (Fig. 1 c). The obtained spectral function has got similar shape for each value of x. A blurred peak-like maximum is observed roughly at the same $\varepsilon_B = -0.3$ eV for each composition. This feature can be assigned to $4f^1{}_{7/2}$ final state [38].

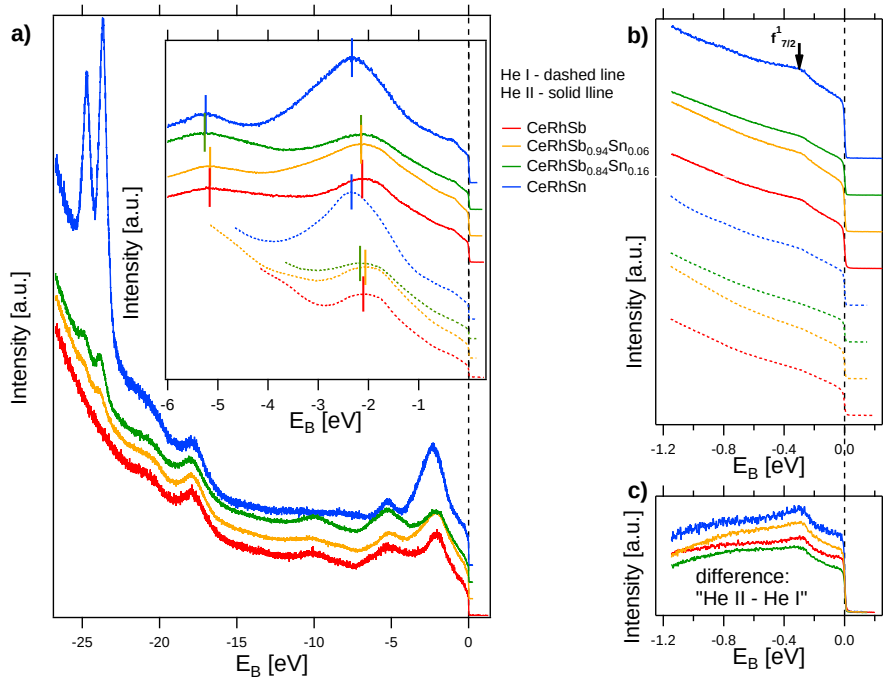

Fig. 1 (Color online) Valence band of the $CeRhSb_{1-x}Sn_x$ ($x = 0$, 0.06, 0.16, 1) system studied by means of ultraviolet photoemission spectroscopy. All measurements have been performed at T=12.5 K a) Spectra obtained with application of He II radiation in wide energy range. (Inset) Comparison of valence band spectra of studied compounds obtained with He I and He II radiation. Solid vertical lines denote peak maxima obtained with fitting the Gaussian function. b) High resolution spectra of valence band near ε_F, obtained with He I and He II radiation. c) Extracted 4f contribution to spectral function for each studied compound.

The estimated Ce 4f spectral function of $CeRhSb_{1-x}Sn_x$ does not reveal any enhancement of the intensity at ε_F even for evidently metallic CeRhSn compound. This stands in a difference with some previous PES experiments performed on Kondo insulators, which often yield spectra which cannot be distinguished from that of weakly hybridized Kondo metal [18], because of low experimental resolution or presence of nonmagnetic impurities. Additionally, the lack of enhancement of signal at ε_F can be explained as follows. Firstly, theoretical calculations, which are discussed below, predict that Ce 4f partial DOS concentrates mostly above ε_F for all possible concentrations of Sn. Secondly, if the so called Kondo peak is present in spectral function of CeRhSn it is located, according to the Friedel sum rule, above ε_F [39]. PES probes spectral function within occupied states, making observation of any enhancement of DOS almost infeasible in both situations.

However, we believe that due to careful normalization of the spectra we can discuss how the spectral intensity at ε_F changes with substitution of Sn in place of Sb. Namely, one can see that for $x = 0.06$ the signal at ε_F increases by 13%, while in case of $x = 0.16$, spectral intensity at ε_F decreases by 16%, with respect to $x = 0$. Intensity

measured at ε_F for CeRhSn is greater by about 33% than that for CeRhSb. Nevertheless, samples with $x = 0.16$ are likely to be more defected, which may explain the lower signal at ε_F. Hence, we cannot conclude, if a reduction of DOS for $x = 0.16$ is intrinsic to this QPT or rather is an effect of disorder. The remaing compositions show a general increase of DOS at ε_F with doping.

3.4 Theoretical calculations - scalar relativistic approach

Total and partial DOS of $CeRhSb_{1-x}Sn_x$ have been calculated within scalar relativistic scheme for $0 \leq x \leq 0.3$. Calculated DOS has got a similar shape for each composition. We present results for $CeRhSb_{0.94}Sn_{0.06}$ (Fig. 2 a). VB is mainly composed of Ce 4f and Rh 4d states with admixture of Sn 5p and Ce 5d states. Partial DOSes are symmetric for both spin directions, as expected, because we have not included additional correlations in computational scheme. Ce 4f spectrum concentrates mainly above ε_F. Peak-like structure corresponding to 4f states is centered at about 0.5 eV and it extends roughly from ε_F to 0.9 eV. In the close vicinity of ε_F one can notice a depletion of Ce 4f DOS (Fig. 2 b). A "v-shape" gap is formed with non-zero DOS at minimum ($\approx$1 state/(eV·unit cell)). The calculations show that such a gap is located at ε_F for CeRhSb and is shifted above ε_F with Sn doping. As a consequence, DOS at ε_F is very low for a semimetallic CeRhSb and grows with x. Such a gap is also present in Rh 4d and total DOS. It is in line with ”semiconducting” character of the system for $0 \leq x \leq x_c$. Such residual states in the gap are consistent with measurements of specif heat [40]. It is noteworthy, that Anderson lattice model at half filling also predicts a gap in 4f spectral function, as well as in a spectrum of carriers from conduction band for KIs with momentum independent hybridization [41, 42].

The photoelectron spectra were simulated using theoretical DOS (cf. the lowest panel of Fig. 2 a). They reproduce the shape of the valence band obtained experimentally. It appears that the contribution from Rh 4d states dominates the valence band spectra. Rh 4d states extend mainly from ε_B equal to -5 eV to about 2 eV. Rh 4d theoretical spectrum consists of two broad structures below ε_F, located at about -3 eV and -2 eV, respectively. Direct comparison of the simulated photoelectron spectra with the measurements shows good agreement in case of the structure at -2 eV. However, the maximum located at -3 eV in simulation is observed roughly at -5 eV in the experimental data.

In Sb/Sn spectrum we observe a peak originating from Sb 5s states, which is found approximately at -9 eV (not shown). This structure was also observed in He II PS spectra near ≈ -10 eV (Fig. 1 a). A leading contribution from Sb/Sn site to DOS comes from 5p states. These states are smeared over whole VB, with increased contribution in ε_B range from about -5 eV to -3 eV. Sb/Sn 5p states are also depleted in the vicinity of ε_F.

3.5 Theoretical calculations - full relativistic approach

Partial DOS calculated in full relativistic approach for compounds with $x = 0$, 0.06, and 0.16, in principle has got a similar shape as this obtained within scalar relativistic

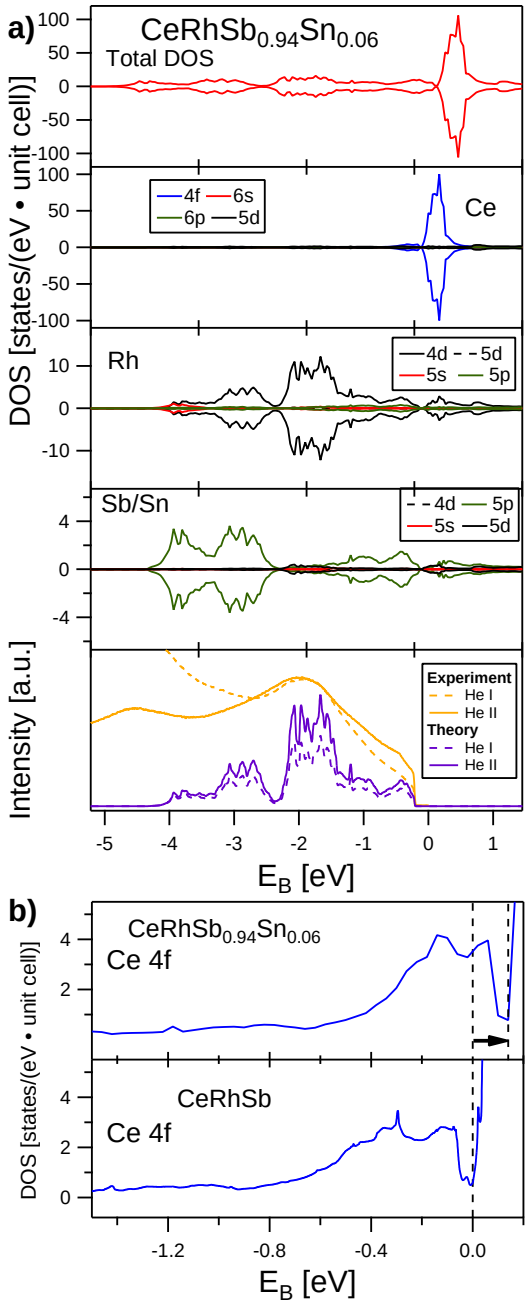

Fig. 2 (Color online) Results of FPLO calculations with scalar relativistic approach. a) Partial densities of states calculated for $CeRhSb_{0.94}Sn_{0.06}$. The lowest panel presents a comparison between experimental (collected at $T = 12.5$ K) and simulated spectra of $CeRhSb_{0.94}Sn_{0.06}$. b) Ce 4f partial DOS calculated for $CeRhSb_{0.94}Sn_{0.06}$ (upper panel) and for CeRhSb (lower panel). The black arrow indicates the position of the minimum in DOS which is discussed in the text.

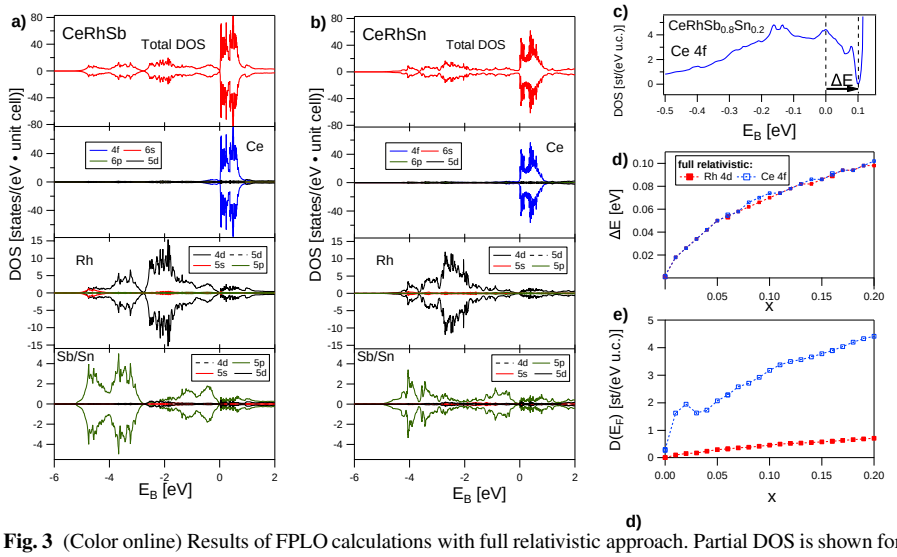

Fig. 3 (Color online) Results of FPLO calculations with full relativistic approach. Partial DOS is shown for (a) CeRhSb, (b) CeRhSn. (c) Ce 4f partial DOS calculated for $CeRhSb_{0.8}Sn_{0.2}$. The black arrow indicates the position of the minimum in DOS, which is the closest to the Fermi energy. d) Position of the partial Ce 4f and Rh 4d DOS minimum as a function of x in $CeRhSb_{1-x}Sn_x$. e) Partial Ce 4f (blue open squares) and Rh 4d (red filled squares) densities of states at the Fermi level for $CeRhSb_{1-x}Sn_x$.

scheme (Fig. 3 a, b). A difference is visible in Ce 4f spectra, the structure above ε_F is different than that discussed previously. In case of $x = 0$, 0.06 and 0.16, the gap-like depletion of DOS in vicinity of ε_F is also observed (Fig. 3 c).

The position of the gap in Ce 4f and Rh 4d DOS is a rising function of x (Fig. 3 d). The gap is located at ε_F for CeRhSb. It is shifted above ε_F as a result of hole doping. The same trend is observed for Ce 4f and Rh 4d states. The influence of the doping is also visible in DOSes at ε_F (Fig. 3 e). The Rh 4d partial DOS at ε_F rises almost linearly with x, while in case of Ce 4f a small maximum at $x = 2$ is visible. However, both Ce 4f and Rh 4d DOS at ε_F are enhanced with respect to $x = 0$.

Partial DOS calculated for different orbital characters in CeRhSn, is different from the corresponding DOS in the compounds with non-zero Sb amount. There is no longer gap in vicinity of ε_F. Strictly speaking, in Rh 4d and in Sn 5p spectral densities, there is a significant, gap-like depletion at ε_F. However in case of Ce 4f, ε_F is located in the rising slope of the peak in DOS. One can conclude that metallic properties of CeRhSn are mostly related to 4f electrons.

Dispersion of the bands in the first BZ, calculated within full relativistic FPLO method, is shown in Fig. 4. For all studied compounds, except for CeRhSn, bands have similar shape. At the first sight it seems that Fermi level is simply shifted in a direction corresponding to lowering electron band filling. However, a more detailed analysis shows that there are significant deviations from a rigid band shift. Nevertheless, due to displacing bands below Fermi energy and shifting another bands to the Fermi level one can anticipate interesting modifications of the Fermi surface topology. The observed band shifts suggests that certain filled bands may become hole bands and some electron parts of the Fermi surface may disappear with doping. This

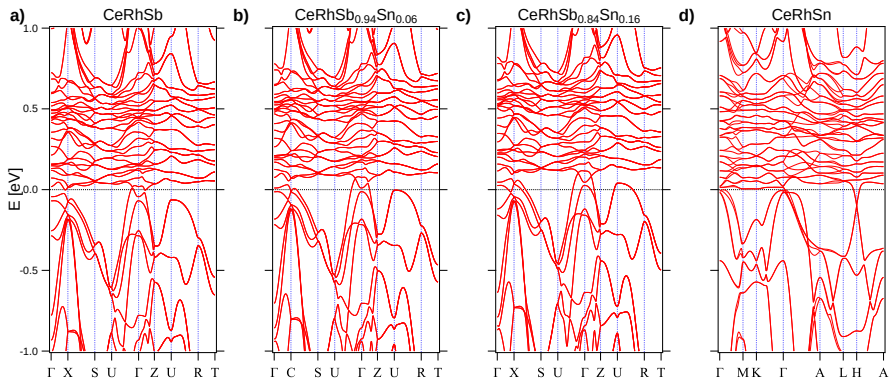

Fig. 4 (Color online) Band structure along high symmetry directions calculated for $CeRhSb_{1-x}Sn_x$ ($x =$ 0, 0.06, 0.16, 1) with FPLO method in full relativistic approach.

would mean that Lifshitz transitions occur with growing x. Careful analysis of the evolution of FS may confirm that and it is presented in the next section.

The bands related mostly to 4f electrons are characterized by a very weak dispersion and lie just above ε_F. In band structure of CeRhSn there are bands located nearly at ε_F related to 4f electrons and characterized by high effective mass. There is one band along M-K-Γ direction, which is especially flat and lies just above ε_F.

3.6 Calculated Fermi surfaces

Theoretical calculations performed in full relativistic approach have yielded Fermi surfaces (FSes) of representatives of $CeRhSb_{1-x}Sn_x$ family (Fig. 5). The shape of the FS strongly depends on x. The band structure calculated along high symmetry lines (Fig. 4) shows that the number of bands crossing ε_F depends on the sample composition. The same feature is reflected in the FS contours. The shape of FS changes with x in a discontinuous manner. The variation of the number of separated parts of FS foreshadows the topological changes of FS, which can be regarded as a sequence of subsequent Lifshitz transitions. In case of CeRhSb, four hole-like pockets contribute to the FS. They are transformed under doping ($x = 0.02$) into one tori-like structure extended along Γ-X direction. For $x = 0.03$ FS can be regarded as two deformed concentric spheres. The increase in x leads to increase of the overall volume of FS. For $x = 0.05$ FS contour reaches the border of the BZ, resulting in opening of FS. Moreover, some new parts of FS, attributed to band 1 emerge. In case of $x = 0.6$, FS consists of four leaf-like structures near the X-U-S BZ wall (band 1) and a barrel-like shape along Γ-X direction with two plate-like structures on both sides of the X point (band 2). Subsequent increase in x makes leaf like structures merge into a pair of bow-tie shaped structures. The barrel-like shape becomes bigger, while the bottoms (plate-like structures) disappear. Afterwards, the additional closed part of FS appears around the Γ point, for $x = 0.09$. The volume of this structure increases with x, and

eventually it touches and merges with the bow tie-like structure near to X-U-S wall of BZ. In parallel, the volume of the barrel like band 2 increases.

The presented simulations indicate that Sn substitution in $CeRhSb_{1-x}Sn_x$ system modifies FS topology six times for x ranging from 0 to 0.2. This is interpreted as a sequence of Lifshitz transitions. FS volume is also considerably increased. It is difficult to assign a particular Lifshitz transition to QPT because the location of ε_F is given with some uncertainty in DFT calculations. Hence, Sn concentrations in calculations may correspond to a shifted value of x in a real system. Nevertheless, a general increase of DOS at ε_F, FS volume and a number of band crossing ε_F certainly helps to understand the modifications of electronic structure, which are related to QPT.

4 Conclusions

We have investigated electronic structure of $CeRhSb_{1-x}Sn_x$ family, in which QPT occurs. VB spectra obtained with UPS agree qualitatively with both scalar relativistic and full relativistic FPLO calculations. They are dominated by Rh 4d states. The spectra collected at 12.5 K, do not reveal 4 f electron peak in vicinity of ε_F. However, the feature related to $4f^1{}_{7/2}$ final state is clearly visible in Ce 4f spectral function extracted for each of the studied compounds. The UPS results exhibit a tendency of Ce 4f derived DOS at ε_F to rise with Sn content. Calculated DOS yields a semimetallic character of CeRhSb with a gap-like minimum in DOS at ε_F. This gap is shifted above ε_F with Sn doping leading to metallic properties. Full relativistic calculations show that due to the effect of hole doping realized with Sn substitution a few modifications of FS topology takes place. These are interpreted as Lifshitz transitions. The calculations also yield that FS volume generally grows and a number of band crossings at ε_F increases as a function of x. These results visualize the evolution of the electronic structure which occurs in QPT in $CeRhSb_{1-x}Sn_x$ system.

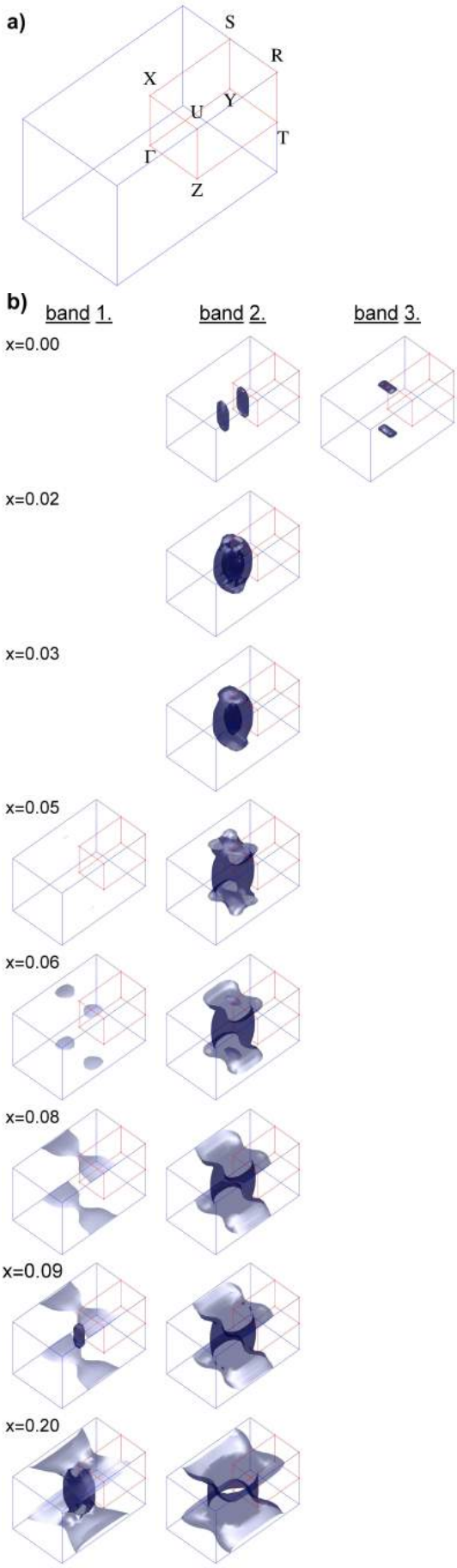

Fig. 5 (Color online) a) The first Brillouin zone of $CeRhSb_{1-x}Sn_x$. b) The Fermi surface of selected representatives of $CeRhSb_{1-x}Sn_x$ system.

Acknowledgements This work has been supported by the National Science Centre, Poland within the Grant no. 2016/23/N/ST3/02012. Support of the Polish Ministry of Science and Higher Education under the grant 7150/E-338/M/2018 is acknowledged.

Author contribution statement

A. Ś. and P. S. came up with the presented idea. A. Ś. synthesized and characterized the used samples. J. G. performed theoretical calculations. Photoelectron spectroscopy was performed by R. K., M. R. and P. S. R. K. performed data analysis and comparison with theoretical results. The project was realized under supervision of P. S. All authors discussed the obtained results and contributed to the article.

References

1. J.A. Hertz, Phys. Rev. B **14**, 1165 (1976). DOI 10.1103/PhysRevB.14.1165
2. S. Sachdev, *Quantum Phase Transitions* (Cambridge University Press, 2000). DOI 10.1017/CBO9780511622540
3. P. Coleman, A.J. Schofield, Nature **433**(7023), 226 (2005). DOI 10.1038/nature03279
4. Q. Si, S. Paschen, Phys. Status Solidi B **250**(3), 425 (2013). DOI 10.1002/pssb.201300005
5. R. Doradziński, J. Spałek, Phys. Rev. B **58**, 3293 (1998). DOI 10.1103/PhysRevB.58.3293
6. A. Ślebarski, J. Spałek, Phys. Rev. Lett. **95**, 046402 (2005). DOI 10.1103/PhysRevLett.95.046402
7. P.S. Riseborough, Adv. Phys. **49**(3), 257 (2000). DOI 10.1080/000187300243345
8. T. Takabatake, F. Iga, T. Yoshino, Y. Echizen, K. Katoh, K. Kobayashi, M. Higa, N. Shimizu, Y. Bando, G. Nakamoto, H. Fujii, K. Izawa, T. Suzuki, T. Fujita, M. Sera, M. Hiroi, K. Maezawa, S. Mock, H. Von Lohneysen, A. Bruckl, K. Neumaier, K. Andres, J. Magn. Magn. Mater. **177**(1), 277 (1998). DOI 10.1016/S0304-8853(97)00842-1
9. J. Spałek, A. Ślebarski, J. Goraus, L. Spałek, K. Tomala, A. Zarzycki, A. Hackemer, Phys. Rev. B **72**, 155112 (2005). DOI 10.1103/PhysRevB.72.155112
10. O. Janka, O. Niehaus, R. Pöttgen, B. Chevalier, Zeitschrift für Naturforschung B **71**, 737 (2016). DOI 10.1515/znb-2016-0101
11. Pöttgen, Zeitschrift für Naturforschung B **61**, 677 (2014). DOI 10.1515/znb-2006-0607
12. S. Malik, D. Adroja, Phys. Rev. B **43**(7, B), 6277 (1991). DOI 10.1103/PhysRevB.43.6277
13. A. Ślebarski, T. Zawada, J. Spałek, A. Jezierski, Phys. Rev. B **70**(23) (2004). DOI 10.1103/PhysRevB.70.235112
14. A. Ślebarski, J. Spałek, M. Gamża, A. Hackemer, Phys. Rev. B **73**(20) (2006). DOI 10.1103/PhysRevB.73.205115

15. A. Ślebarski, A. Jezierski, A. Zygmunt, Acta Phys. Pol. A **97**(1), 59 (2000). DOI 10.12693/APhysPolA.97.59
16. K. Breuer, S. Messerli, D. Purdie, M. Garnier, M. Hengsberger, Y. Baer, M. Mihalik, Phys. Rev. B **56**, R7061 (1997). DOI 10.1103/PhysRevB.56.R7061
17. T. Susaki, A. Sekiyama, K. Kobayashi, T. Mizokawa, A. Fujimori, M. Tsunekawa, T. Muro, T. Matsushita, S. Suga, H. Ishii, T. Hanyu, A. Kimura, H. Namatame, M. Taniguchi, T. Miyahara, F. Iga, M. Kasaya, H. Harima, Phys. Rev. Lett. **77**, 4269 (1996). DOI 10.1103/PhysRevLett.77.4269
18. K. Breuer, S. Messerli, D. Purdie, M. Garnier, M. Hengsberger, G. Panaccione, Y. Baer, T. Takahashi, S. Yoshii, M. Kasaya, K. Katoh, T. Takabatake, Europhys. Lett. **41**, 565 (1998). DOI 10.1209/epl/i1998-00192-1
19. M. Klein, A. Nuber, F. Reinert, J. Kroha, O. Stockert, H. v. Löhneysen, Phys. Rev. Lett. **101**, 266404 (2008). DOI 10.1103/PhysRevLett.101.266404
20. A. Ślebarski, M.B. Maple, E.J. Freeman, C. Sirvent, M. Radłowska, A. Jezierski, E. Granado, Q. Huang, J.W. Lynn, Philos. Mag. B **82**(8), 943 (2002). DOI 10.1080/13642810208218354
21. K. Shimada, H. Namatame, M. Taniguchi, M. Higashiguchi, S.I. Fujimori, Y. Saitoh, A. Fujimori, M.S. Kim, D. Hirata, T. Takabatake, Physica B **378-80**, 791 (2006). DOI 10.1016/j.physb.2006.01.289
22. M. Taniguchi, J. Alloy. Compd. **362**(1-2), 133 (2004). DOI 10.1016/S0925-8388(03)00573-5
23. K. Shimada, M. Higashiguchi, M. Arita, H. Namatame, M. Taniguchi, S.i. Fujimori, Y. Saitoh, A. Fujimori, Y. Takata, S. Shin, K. Kobayashi, E. Ikenaga, M. Yabashi, K. Tamasaku, Y. Nishino, D. Miwa, T. Ishikawa, T. Sasakawa, T. Takabatake, J. Magn. Magn. Mater. **310**(2, 1), E57 (2007). DOI 10.1016/j.jmmm.2006.10.201
24. H. Kumigashira, T. Sato, T. Yokoya, T. Takahashi, S. Yoshii, M. Kasaya, Phys. Rev. Lett. **82**, 1943 (1999). DOI 10.1103/PhysRevLett.82.1943
25. H. Kumigashira, T. Takahashi, S. Yoshii, M. Kasaya, Phys. Rev. Lett. **87**, 067206 (2001). DOI 10.1103/PhysRevLett.87.067206
26. J. Goraus, A. Ślebarski, Phys. Staus Solidi B **250**(3, SI), 533 (2013). DOI 10.1002/pssb.201200615
27. M. Gamża, A. Ślebarski, H. Rosner, Eur. Phys. J. B **67**(4), 483 (2009). DOI 10.1140/epjb/e2009-00047-1
28. K. Koepernik, H. Eschrig, Phys. Rev. B **59**, 1743 (1999). DOI 10.1103/PhysRevB.59.1743
29. I. Opahle, K. Koepernik, H. Eschrig, Phys. Rev. B **60**(20), 14035 (1999). DOI 10.1103/PhysRevB.60.14035
30. K. Lejaeghere, G. Bihlmayer, T. Björkman, P. Blaha, S. Blügel, V. Blum, D. Caliste, I.E. Castelli, S.J. Clark, A. Dal Corso, S. de Gironcoli, T. Deutsch, J.K. Dewhurst, I. Di Marco, C. Draxl, M. Dułak, O. Eriksson, J.A. Flores-Livas, K.F. Garrity, L. Genovese, P. Giannozzi, M. Giantomassi, S. Goedecker, X. Gonze, O. Grånäs, E.K.U. Gross, A. Gulans, F. Gygi, D.R. Hamann, P.J. Hasnip, N.A.W. Holzwarth, D. Iuşan, D.B. Jochym, F. Jollet, D. Jones, G. Kresse, K. Koepernik, E. Küçükbenli, Y.O. Kvashnin, I.L.M. Locht, S. Lubeck, M. Marsman, N. Marzari, U. Nitzsche, L. Nordström, T. Ozaki, L. Paulatto, C.J. Pickard,

W. Poelmans, M.I.J. Probert, K. Refson, M. Richter, G.M. Rignanese, S. Saha, M. Scheffler, M. Schlipf, K. Schwarz, S. Sharma, F. Tavazza, P. Thunström, A. Tkatchenko, M. Torrent, D. Vanderbilt, M.J. van Setten, V. Van Speybroeck, J.M. Wills, J.R. Yates, G.X. Zhang, S. Cottenier, Science **351**(6280) (2016). DOI 10.1126/science.aad3000

31. H. Eschrig, K. Koepernik, I. Chaplygin, J. Solid State Chem. **176**, 482 (2003). DOI 10.1016/S0022-4596(03)00274-3
32. H. Eschrig, M. Richter, I. Opahle, in *Relativistic Electronic Structure Theory, Theoretical and Computational Chemistry*, vol. 14, ed. by P. Schwerdtfeger (Elsevier, 2004), pp. 723 – 776. DOI https://doi.org/10.1016/S1380-7323(04)80039-6
33. H. Eschrig, *The Fundamentals of Density Functional Theory*, 2nd edn. (Edition am Gutenbergplatz, Leipzig, 2003)
34. J.J. Yeh, *Atomic Calculation of Photoionization Cross-Sections and Asymmetry Parameters* (Gordon and Breach Science Publishers, Langhorne, PE (USA), 1993)
35. H. Höchst, M.K. Kelly, Phys. Rev. B **30**, 1708 (1984). DOI 10.1103/PhysRevB.30.1708
36. N.V. Smith, G.K. Wertheim, S. Hüfner, M.M. Traum, Phys. Rev. B **10**, 3197 (1974). DOI 10.1103/PhysRevB.10.3197
37. J. Yeh, I. Lindau, Atom. Data Nucl. Data **32**(1), 1 (1985). DOI https://doi.org/10.1016/0092-640X(85)90016-6
38. A. Sekiyama, T. Iwasaki, K. Matsuda, Y. Saitoh, Y. Onuki, S. Suga, Nature **403**(6768), 396 (2000). DOI 10.1038/35000140
39. A. Georges, C. R. Phys. **17**(3), 430 (2016). DOI https://doi.org/10.1016/j.crhy.2015.12.005
40. S. Nishigori, H. Goshima, T. Suzuki, T. Fujita, G. Nakamoto, H. Tanaka, T. Takabatake, H. Fujii, J. Phys. Soc. Jpn. **65**(8), 2614 (1996). DOI 10.1143/JPSJ.65.2614
41. C. Grober, R. Eder, Phys. Rev. B **57**(20), R12659 (1998). DOI 10.1103/PhysRevB.57.R12659
42. M. Rozenberg, G. Kotliar, H. Kajueter, Phys. Rev. B **54**(12), 8452 (1996). DOI 10.1103/PhysRevB.54.8452

Chapter 8

Direct observation on f-electron hybridization effects in $CeCoIn_5$

Highlights

- the electronic structure of heavy fermion superconductor $CeCoIn_5$ has been mapped at 6 K using ARPES method
- a band characterized by large effective masses and high f orbital contribution has been observed in spectra near the Fermi level
- the significant effect of matrix elements on the ARPES spectra has been observed
- a symmetrization of experimentally obtained Fermi surface allowed to extract variation of 4f electron spectral intensity, which is related to the effect of hybridization, what was confirmed by tight binding calculations

Abstract

A heavy fermion superconductor, $CeCoIn_5$ was studied by angle-resolved photoemission spectroscopy (ARPES) with excitation energy corresponding to Ce 4d-4f resonance. Fermi surface (FS) maps with pronounced Ce 4f electron spectral weight have been obtained at temperature of T=6 K in wide angular range. Various effects of a hybridization between valence band and f-electrons (V_{cf}) have been observed. These are e.g. heavy f-electron dispersing bands and variable f-electron contribution along FS. Due to a strong variation of hybridization between FS branches certain bands are strongly correlated with high f-electron contribution while others are weakly correlated. The hot spots at E_F found around the Γ point in ARPES spectra, which represent highly correlated states, coincide with high contribution from In atoms (5p electrons) located in Ce-In layers, which have been identified as principal surface termination with a help of one-step model calculations.

Spectral weight of f-electrons at E_F is determined by both matrix element effects and the form of wave vector dependent $V_{cf}(k)$. FS scans covering a few Brillouin zones allowed to observe large matrix element effects. In contrast, the influence of V_{cf} on spectral intensity obeys the reciprocal lattice symmetry. A symmetrization of experimental FS, which reduced matrix element effects to some extent, yielded a specific variation of 4f electron spectral intensity at E_F around Γ and M points, which was attributed to a pure effect of V_{cf} hybridization. Tight binding approximation calculations for Ce-In plane yielded the same, quite universal distribution of 4f electron density for a variety of parameters used in TBA. This proves that we were able to extract the effect of V_{cf} on f-electron intensity in ARPES spectra.

8.1 Introduction

Hybridization between 4f electrons and conduction band (V_{cf}) leads to various fascinating phenomena such as Kondo effect, heavy fermion state or mixed valence (Stewart, 1984). It can also play a role in quantum phase transitions and superconductivity. In case of many Ce systems photoemission spectroscopy reveals a high intensity peak near the Fermi energy (E_F) with strong contribution from 4f electrons and this spectral feature is called a Kondo resonance in some cases (Klein et al., 2011; Sekiyama et al., 2000; W. Allen, 2005).

Already early ARPES studies of the Kondo resonance for Ce systems pointed that its intensity depends on wave vector, which is a fingerprint of anisotropic hybridization (Garnier et al., 1997). Later it was observed that this f-electron related peak is intensive at Fermi vectors (Danzenbächer et al., 2005). Finally, it is known that bands, which are strongly correlated with 4f electrons, may coexist with those weakly correlated (Koitzsch et al., 2013). In fact, anisotropic structure of V_{cf} is a source of f-electron peak intensity variation along the Fermi surface (FS) (Ghaemi et al., 2008). However, matrix element effects play an important role here and also have a serious influence in this intensity. Although, it is believed that anisotropic V_{cf} yields a specific distribution of f-electron peak along FS, its structure described consistently by ARPES and theory was not presented so far.

The effects described above can be conveniently studied on the example of intermetallics from $Ce_mT_nIn_{3m+2n}$ family (T - transition metal) (Thompson et al., 2003). We choose $CeCoIn_5$, which despite of relatively simple, layered crystal structure hosts many interesting physical states (Shimozawa et al., 2016; Steglich and Wirth, 2016). Namely, the superconductivity with T_c of 2.3 K has been observed in this compound (Petrovic et al., 2001). The heavy fermion state, which appears due to hybridization between 4f electrons and conduction band, can be characterized by Sommerfeld coefficient γ which amounts to 0.35 J/(mole·K^2) (Thompson et al., 2003) and coherence temperature equal to 45 K (Jia et al., 2011). Such a system provides an opportunity to study exotic phenomena like quantum criticality (Paglione et al., 2003) or Fulde-Ferrel-Larkin-Ovchnnikov (FFLO) type superconductivity at high magnetic fields (Kumagai et al., 2006).

In this paper we report a systematic ARPES study performed for a $CeCoIn_5$ heavy fermion compound. Observation of different hybridization effects, which depend on band and Fermi vector, gives an image of V_{cf} effects in ARPES spectra. A principal role in a formation of the observed heavy fermion bands is played by Ce-In planes. Distribution of f-electron spectral weight at ε_F obtained with tight binding approximation (TBA) calculations is found in the ARPES FS mapping, what allows to propose an image of V_{cf} hybridization for the investigated system.

8.2 Material and methods

Single crystalline samples of $CeCoIn_5$ have been obtained using the flux method. Their synthesis and characterization is described elsewhere (Jia et al., 2011). They have been oriented along important crystallographic directions using X-ray diffraction (Laue method). The ARPES measurements have been realized in Cassiopee beamline of Synchrotron Soleil (Paris, France). All measurements have been performed at temperature equal to 6 K. The Scienta R4000 photoelectron energy analyzer has been used. The samples have been cleaved in ultra high vacuum conditions prior to the measurements (base pressure: 10^{-10} mbar). The (001) plane was exposed after cleaving. Spectra have been collected using radiation with energy equal to 122 eV (Ce 4d-4f resonant transition) and 87 eV. The electronic structure of $CeCoIn_5$ has been calculated using Korringa-Kohn-Rostoker (KKR) method in single particle Green function approach with application of multiple scattering theory (Ebert et al., 2011). The implementation of the method in a spin polarized relativistic Korringa-Kohn-Rostoker (SPR-KKR) code for Calculating Solid State Properties (SPR-KKR) has been used. The tight binding approximation (TBA) model (Maehira et al., 2003) based on the generalized Slater-Koster approach (Slater

and Koster, 1954) has been fitted to the experimental band structure. The five orbital TBA model for Ce-In planes comprises three doublets from Ce $4f_{\frac{5}{2}}$ manifold (f_a, f_b, f_c) together with two doublets (p_a, p_b; $j_z = \pm 1$) from In 5p manifold. The 5p state with $j_z = 0$ does not contribute to the band structure of Ce-In layer near the Fermi level. Average occupancy of the f shell was fixed during fits as $n_f = 1$.

8.3 Results and Discussion

Fermi surface (FS) of $CeCoIn_5$ was studied by ARPES at low temperature (T=6 K) in a wide angular range for two sample orientations (Fig. 8.1 a-c). Such experiment allows to visualize not only FS topography but enables a closer look into a contribution from f-electrons and matrix element effects. These last depend on experimental geometry, photon energy and on a probed Brillouin zone. Fig. 8.1 a-c presents spectral intensity at a Fermi energy (E_F) along semi-planar cuts of the reciprocal lattice. The spectra recorded with $h\nu$=122 eV photons, namely at Ce $4d$-$4f$ resonance, assure an increased contribution from Ce 4f electrons (Fig. 8.1 a, b) as compared to off-resonance data obtained with $h\nu$=87 eV (Fig. 8.1 c). It is known that ARPES mapping with photon energy of 122 eV probes the region close to Γ point in three-dimensional Brillouin zone (Fig. 8.1 d) for normal emission (Chen et al., 2017). The assumption of inner potential $V_0 = 16$ eV (Chen et al., 2017) allowed to find the off-resonance energy of 87 eV, for which the scanned surface in k-space crosses the Γ point at k_x=0 and k_y=0 as well.

Even a superficial analysis of spectral intensity dominated by Ce 4f electrons (Fig. 8.1 a, b) leads to a conclusion that it breaks the reciprocal lattice symmetry and such a result is independent of the applied method of spectra normalization. Hence, the reason for such asymmetry must be in matrix element effects. Moreover, the matrix element effects must be responsible for different distribution of spectral intensity in Figs. 8.1 a and b as these differ just by sample orientation. It also is known that a variation of f-electron density and related spectral intensity may also depend on a specific form of hybridization between f-electrons and the valence band (V_{cf}) (Ghaemi et al., 2008; Starowicz et al., 2014) but such a variation must fit into the reciprocal lattice symmetry in contrary to matrix element effects, which depend i.a. on experimental geometry (Fig. 8.1 e). Therefore, one can distinguish the areas of higher 4f-electron signal, while equivalent k-space regions exhibit a depletion of intensity. Such high intensity areas are indicated with black dashed line rectangles in Fig. 8.1 a-c. It is noteworthy that the off-resonance FS (Fig. 8.1 c) regains more reciprocal lattice symmetry, what signifies that quite prominent matrix element effects on intensity are related to f-electrons.

The first approach to understand the spectral intensity are one-step model calculations realized with SPR-KKR code (Ebert et al., 2011), which treat the system as a semi-infinite crystal with a specific surface termination. A projection of both bulk and surface initial states on time-reversed LEED final states yields a simulation of ARPES spectra, which takes into account photon energy, light polarization, experimental geometry, final state effects and surface termination. As there are 3 possible surface terminations for cleaved $CeCoIn_5$ (Fig. 8.1 f) such calculations have been performed for Ce-In (Fig. 8.1 g), Co (Fig. 8.1 h) and In_2 (Fig. 8.1 i) terminations as marked with arrows in Fig. 8.1 f. They indicate that Ce-In termination prevails as corresponding simulated ARPES spectra for $h\nu$=122 eV (Fig. 8.1 g) fit the experimental results, what is also the case for the off resonance ($h\nu$=87 eV) spectra (not shown). The simulations also visualize a break of left-right symmetry, which is characteristic of f-electron intensity in the ARPES FS image. To extract the contribution of f-electrons a simulated spectrum for only 4f initial states was added to the spectrum comprising all initial states (Fig. 8.1 j). This figure presents increased asymmetric contribution of 4f states to photoemission spectra and the lack of symmetry is particularly visible around the Γ point. Thus, we observe that the matrix element effects are strong and they have to be separated, if one wishes to study bare V_{cf} hybridization effects on 4f electron spectrum.

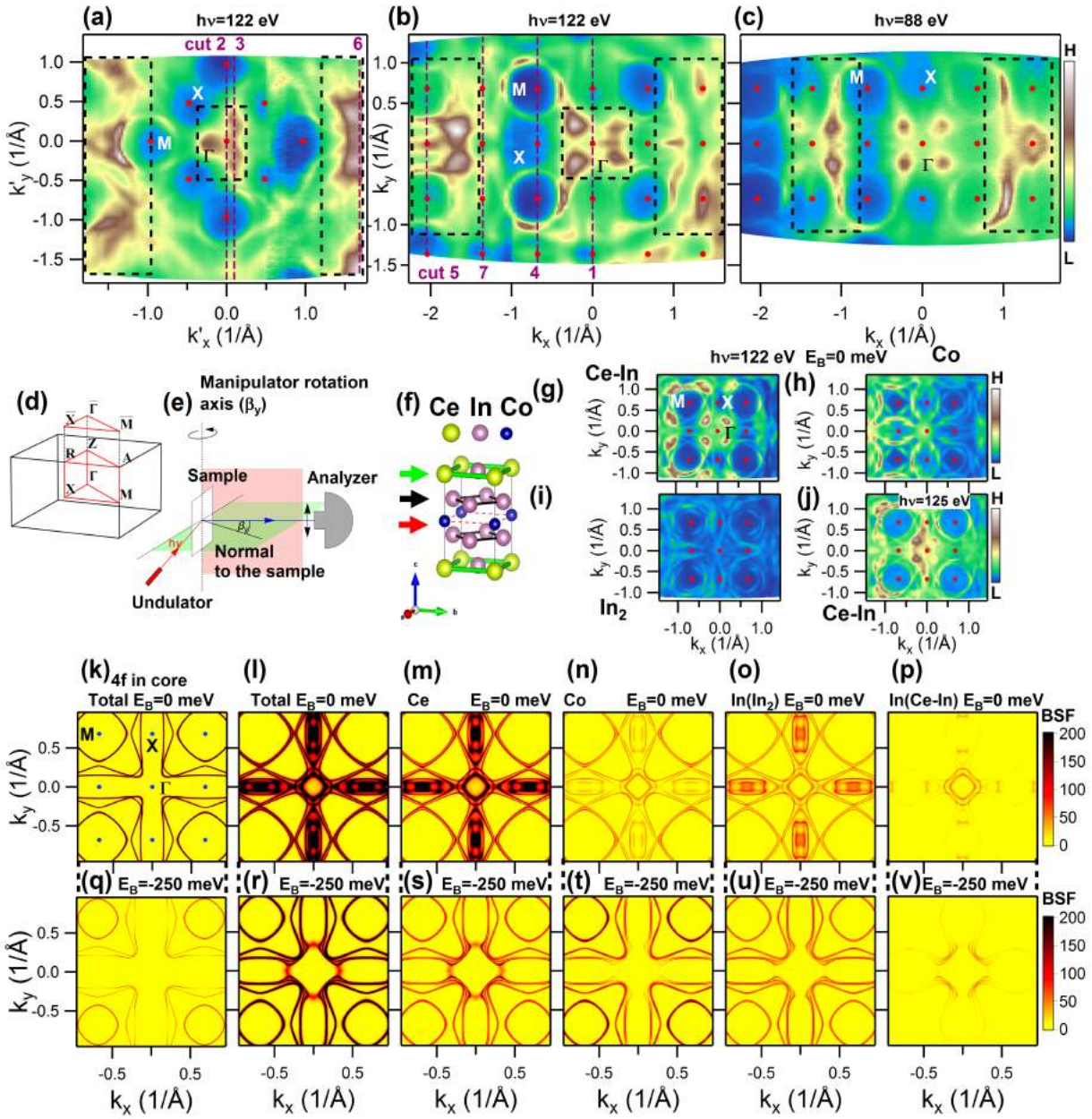

Figure 8.1: (Color on-line) Fermi surface of $CeCoIn_5$. Intensity maps along Fermi surface obtained by ARPES at T=6 K for photon energies of 122 eV (a,b) and 87 eV (c). (d) First Brillouin zone with marked high symmetry points. (e) Crystal structure of $CeCoIn_5$. (f) Geometry of the experiment. Simulation of the ARPES spectra for Ce-In (g), Co (h), In_2 (i) surface terminations using one-step photoemission model based on SPR-KKR calculations for photon energy of 122 eV as well as with enhanced contribution from 4f initial states (j) in case of Ce-In termination. Constant energy contours at 0 eV (k-p) and -0.30 eV (q-v) of Bloch spectral functions obtained in SPR-KKR calculations. These represent a topology of the Fermi surface. The total Bloch spectral function (k,l, q, r) is projected onto atomic wave functions of Ce (m,s), Co (n,t), In from In_2 layers (o,u) and In from Ce-In planes (p,v). The total Bloch spectral function calculated in the absence of hybridization effects (4f in core) is shown in (k) and (q).

Experimental FS topography can be confronted with KKR calculations yielding Bloch spectral functions (BSF), which have been extracted in constant energy contours of E_F (Fig. 8.1 k-p) and 0.25 eV below E_F (Fig. 8.1 q-v) for wave vector $k_z = 0$ (Fig. 8.1 k-v). A presentation for two binding

energies gives already some idea about dispersions, allows to distinguish hole and electron bands and helps to find theoretical counterparts of the experimental FS. Total BSF distributions with f-electrons frozen in a core are given in Fig. 8.1 k, q and the corresponding plot for the system with itinerant f-electrons is shown in Fig. 8.1 l, r. The difference between these figures shows an effect of V_{cf} hybridization with f-electrons on electronic structure. The most prominent changes are located around Γ point and along Γ-X direction, where a large contribution from f-electron states is present. This is visible in particular at $E_B = 0$ defined in calculations (Fig. 8.1 l,m). This f-electron spectral intensity is diminished at lower binding energy (Fig. 8.1 r,s). The calculations show a presence of hole pockets at Γ and X and one large electron pocket at M. In fact, branches of experimental FS correspond to theoretical FS contours located either at $E_B = 0$ or $E_B = -0.25$ eV. Generally, the calculations for $E_B = -0.25$ eV represent well the shape of experimental FS. However, the theoretical contours for $E_B = 0$ show two hole pockets at Γ, which are observed experimentally.

BSF for itinerant f-electrons have been projected on atomic wave functions (Fig. 8.1 m-p, s-v) in order to find a contribution of particular atoms to FS. Ce atoms donate mainly 4f electrons at E_F with high intensity in the region of Γ and M points. Co (mainly 3d) electrons and In atoms from In planes shown by blue arrows in Fig. 8.1 f (high contribution from 5p) contribute rather to the whole FS. However, Co 3d states have a high population in the electron pockets around M (well seen for $E_B = -0.25$ eV), while this population is reduced in some bands around Γ. Interestingly, In 5p electrons from Ce-In planes (green arrows in Fig. 8.1 f) exhibit four prominent maxima around the Γ point visible in particular at at $E_B = -0.25$ eV. These maxima correspond to the location of four hot spots in ARPES maps located around the Γ point along Γ-M direction (Fig. 8.1 a-c). BSF represent states from the whole Brillouin zone, whereas one-step model calculations show that the contribution from Ce-In planes dominates the ARPES image. Even if 4 In atoms per unit cell give high intensity in BSF, one indium atom per unit cell located in the surface Ce-In planes may deliver quite significant contribution to ARPES spectra. Therefore, the hot spots observed in ARPES should correspond to increased contribution from In located in Ce-In planes. Moreover, one can see that also Ce 4f electrons yield a high amplitude of BSF at the same points in k-space (Fig. 8.1 s). This will be reflected in high V_{cf} hybridization effects observed by ARPES. The experimental FS obtained in this work reproduces some shapes also present in previous ARPES studies (Chen et al., 2017; Dudy et al., 2013; Jang et al., 2017; Koitzsch et al., 2013). However, FSs obtained before were recorded at higher temperatures and, depending on a report, with other photon energies, geometry and in some cases other surface terminations. Hence, also four hot spots around Γ were not discussed before.

Band structure obtained by ARPES is shown along important crystallographic directions as well as along other interesting paths in k-space (Fig. 8.2 a-p). These paths are numbered from 1 to 7 and are drawn on experimental FSs (Fig. 8.1 a,b). The increased f-electron contribution reflected in a high signal at E_F is well visible in the spectra presented as energy distribution curves (Fig. 8.2 a-l). One can resolve an electron pocket α around M (Fig. 8.2 b, d, e), hole pockets (β, γ) around the Γ point (Fig. 8.2 a-c) and two hole-like dispersions observed at the X point along M-X-M direction (Fig. 8.2 d, e). These last are attributed to β and γ bands. The measured dispersions are in qualitative agreement with calculated BSF (Fig. 8.2 q). On the other hand, an electron like band around the X point detected along X-Γ-X direction (Fig. 8.2 a) is not found in calculations. The labels α, β and γ correspond to bands observed previously in ARPES spectra of $CeCoIn_5$ (Chen et al., 2017; Dudy et al., 2013; Jang et al., 2017) and these are also named 135, 133 and 131, respectively, in other ARPES study (Koitzsch et al., 2013). BSF with frozen f-electrons is also shown to visualize the effect of these electons on band structure (Fig. 8.2 r). Roughly speaking this is an appearance of heavy bands at or above E_F. Projections of BSF on particular atoms along high symmetry directions is shown in the *Supplementary material*.

Previous ARPES measurements performed by Chen et al. delivered interesting information on heavy fermion formation in $CeCoIn_5$. These studies showed that along the M-Γ direction the bands β and γ become broad and gain high f-electron related intensity with lowering temperature down

to 17 K. We had the opportunity to measure the same region at much lower temperature of 6 K. Therefore, the hybridization effects are quite pronounced; bands β and γ are much broadened and yield high intensity hot spots at FS, while the α band remains sharp and weakly correlated. This is visible in Fig. 8.2 b, c presenting single measurements assuring the same experimental conditions for the band structure along M-Γ-M and the path "3" located next to M-Γ-M direction (Fig. 8.2 b, c).

Panels d and e from the Fig. 8.2 present scans along M-X-M measured in different Brillouin zones and differing by certain value of k_z vector. The α and β bands are better separated in the Fig. 8.2 e. Spectral intensity in these panels differs also due to matrix element effects for 4f electrons. Namely, a contribution from Ce 4f electrons is visible below $k_y \sim -1$ Å^{-1} and above $k_y \sim 1$ Å^{-1} in Fig. 8.2 d, whereas it is enhanced around X in Fig. 8.2 e. This agrees with the general tendency of high and low intensity of 4f electrons related to matrix element effects. Finally, effects of c-f hybridization are also visible in Fig. 8.2 f. High f-electron intensity starts at wave vectors, which would be Fermi vectors in the absence of V_{cf} hybridization. These images present the spectral shape characteristic of V_{cf} hybridization described by the periodic Anderson model (Tahvildar-Zadeh et al., 1998). Finally, the spectra allowed to detect dispersion of f-electron bands. The spectra normalized by Fermi Dirac distribution were subjected to MDC fitting (Fig. 8.2 m,n). The found dispersions were approximated by parabolas, which allowed to estimate values of effective masses, which range from 30 to 130 free electron mass. This does not exclude the existence of higher effective masses in other regions of BZ.

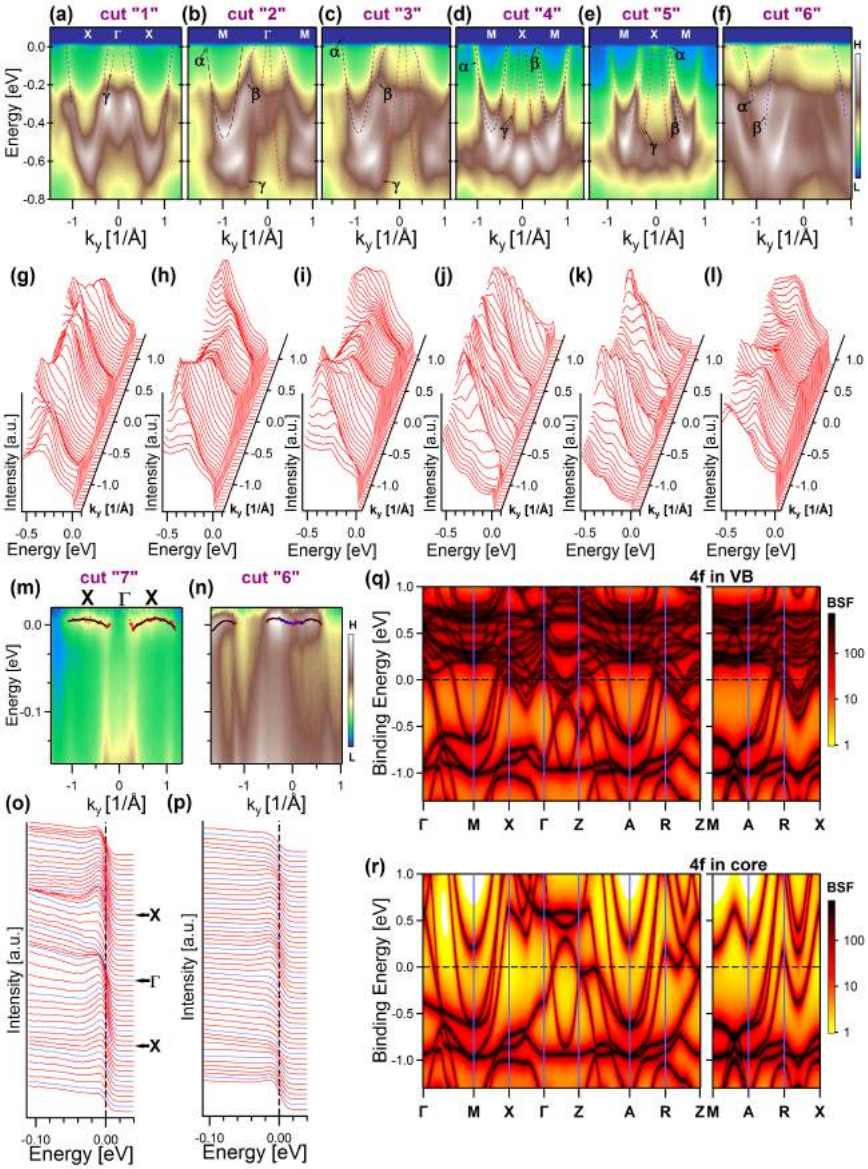

Figure 8.2: (Color on-line) Band structure for $CeCoIn_5$ along selected paths in k-space denoted in the Fig. 8.1. ARPES scans along path "1" (X-Γ-X) (a), path "2" (M-Γ-M) (b), "'3" (c), "4" (M-X-M) (d), "5" (M-X-M) (e), "6" (f). Such band structures are represented in the form of EDCs in panels (g) - (l). Weakly dispersive band is visible near the Fermi level in spectra corresponding to cut "7" (m) and "6' (n) after dividing by Fermi function. The corresponding EDCs are shown in (o) and (p). Panels (q) and (r) present Bloch spectral functions along important crystallographic directions calculated with SPR-KKR package in presence (4f in VB) and absence (4f in core) of hybridization effects, respectively.

Anisotropic V_{cf} hybridization should affect ARPES spectra considerably. The evidence includes not only variation of effective masses and quasiparticle weight (Ghaemi et al., 2008) but also various contribution of 4f electrons to spectra along the Fermi surface. The latter influences spectral intensity at E_F together with matrix element effects. The last should be separated in order to discuss a bare contribution of 4f electrons to the spectra related to V_{cf} hybridization. In order to remove partially geometrical effect of matrix elements, FS was symmetrized by adding spectra rotated by 90°, 180° and 270° to the original Fermi surface (Fig. 8.3 a). We have also performed alternative symmetrization procedure using reflections or their combination with rotations (what corresponds to full 4/mmm point symmetry of Γ point), but this resulted in an image of worse quality. The contour of FS around

corresponding to electron pocket around M point has been described by the circle which was fitted to points belonging to FS. Then we defined the ϕ angle, as the angle between horizontal M-X direction and the line crossing the particular point at the contour and M point. The angles are measured in counterclockwise direction. The momentum distribution curves (MDCs) crossing M point and corresponding to different ϕ angles have been extracted at the Fermi energy (Fig. 8.3 b). The integration over energy window of ± 20 meV around E_F was applied. A closer inspection shows that higher intensity of f-electron related peak at E_F is present along M-X direction whereas it is lower at M-Γ. Energy distribution curves (EDCs) shown for the contour around M point exhibit a variation indicating higher f-electron contribution along same directions as for MDCs (Fig. 8.3 c). Finally, the integrated (over 0.1 x 0.1 Å^{-2} square surroundings) intensity along the electron pocket roughly reproduces minima along M-Γ and maxima along M-X directions. Hence, the symmetrized experimental FS yields the variation of 4f electron related spectral intensity around the M point with minimized matrix element effects. Moreover, Fig. 8.3 a presents a similar variation of spectral intensity around the Γ point. This shows maxima along Γ-M and minima along Γ-X for 4f electron contribution. The spectral intensity at E_F (Fig. 8.3 e) is plotted along the rectangular contour (Fig. 8.3 a) around the Γ point. We did not analyze MDCs and EDCs in this case, as more bands are present around Γ. Here, we propose that such spectral intensity variations observed around M and Γ points are bare V_{cf} hybridization effects.

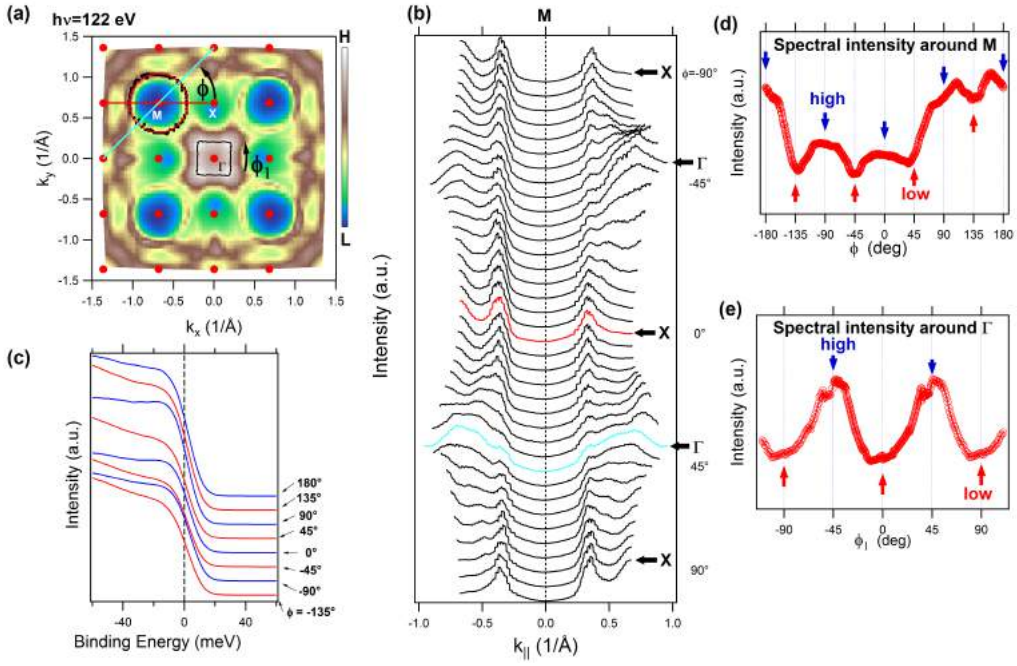

Figure 8.3: (Color on-line) (a) Symmetrized experimental Fermi surface obtained by a superposition of ARPES data rotated 4 times by 90°. Red circle presents the pocket around M subjected to f-electron intensity analysis. (b) Momentum distribution curves extracted from symmetrized data along lines crossing M point in different directions given by ϕ angle as defined in (a). The exemplary red and cyan curves represent paths which are drawn with the same colors in (a). (c) Energy distribution curves from the electron pocket around M for selected ϕ angles. (d) Intensity at the Fermi energy along the electron pocket indicated by the black circle in (a) as a function of ϕ. Red arrows in (d) denote minima in intensity, which appear to be located along Γ-M direction, while blue arrows show M-X direction characterized with higher spectral intensity. (e) Intensity at the Fermi energy along the hole pocket around Γ indicated by the black circle in (a) as a function of ϕ_1. Red arrows denote minima in intensity, which are complementary to these in (d).

The assumption that the effect of V_{cf} hybridization on 4f spectral intensity has been found can be verified by tight-binding model calculations. One should keep in mind that ARPES spectra have a considerable contribution from surface termination, which are Ce-In planes as was proved by a comparison with one-step model calculations (Fig. 8.1). Moreover, the highest contribution to FS from In located in Ce-In planes (5p states) is found at 4 hot spots around the gamma point, where strong hybridization leading to high spectral broadening at low temperature is observed. These arguments support the idea to consider a simple model of Ce-In planes in TBA calculations.

The TBA parameters have been obtained by fitting theoretical dispersions to the experimental binding energies corresponding to M and X points, as well as to experimental Fermi wave vectors in the Γ-X and X-M directions. The obtained theoretical bands are compared with measured ARPES spectra along M-X-M and X-Γ-X directions in Fig. 8.4 a-b . The area of the marker is proportional to the 4f electron contribution to the band. One can see that TBA model describes well the electron pocket around M point. Several bands with dominating f electron contribution are visible above the Fermi level. It is noteworthy, that calculations predict the presence of a hole band around Γ point (Fig. 8.4 b), which becomes flat and gains f electron character close to the Fermi level. This is obvious that not every band visible in measured spectra can be identified in the theory as the TBA minimal theoretical model has to reproduce f-electron intensity variation originating from surface Ce-In layer, which have important contribution to ARPES spectra.

Particular attention should be paid to the distribution of the spectral weight around Γ point, which in accordance with our as well as with previous studies, is related to the heavy quasiparticle band developing at low temperature. The idea of minimal TBA model for $CeCoIn_5$ appeared before (Maehira et al., 2003). However, previously the model has been fitted to the DFT calculations. According to our knowledge, this is the first attempt of fitting such a model to photoemission spectra of $CeCoIn_5$. The distribution of spectral weight at FS predicted by the model is shown in Fig. 8.4 c. The projections on different base states have been shown in Fig. 8.4 d-h. Almost rectangular hole pocket around Γ point shows specific variation of f-electron related spectral intensity. It reaches its maximum at the Γ-M direction, while the minima appears at X-Γ direction. The spectral weight visible in the contour around M point (corresponding to the electron pocket) shows the complementary pattern. On the other hand, the distribution corresponding to In states is much more uniform on the Fermi surface. The observed variation of a spectral weight is consistent with the results of experiments. In fact, one can see that this is exactly the same dependency as shown in Fig. 8.3. Moreover, this is not just an accidental coincidence, because the series of fits for different TBA parameters including those from Maehira et al. (Maehira et al., 2003) have been performed. Therefore, our minimal model can provide some universal description of electronic structure for Ce-In planes in $CeCoIn_5$.

It is noteworthy that maxima and minima of 4f related experimental intensity are reproduced by TBA calculations both around Gamma and M points. It should be stressed that this result is robust against quite considerable variation of TBA parameters (see *Supplementary material*). Hence, such a distribution of 4f electrons is related to original orientation of orbitals building the electronic structure of Ce-In planes and determining anisotropic form of V_{cf} hybridization. Thus, this is the first interpretation of ARPES spectral function indicating the variation of Ce 4f electron intensity, which is related to V_{cf} hybridization after having geometrical factor of matrix element effects eliminated. Although, one might question, if symmetrized experimental data really confirm this variation, as the matrix element effects have not been eliminated completely, the comparison with TBA results with a variety of parameters assures the validity of the conclusions. Finally, TBA calculations with parameters adjusted to ARPES spectra can yield the effective form of V_{cf} hybridization, which may be used to further modeling the system.

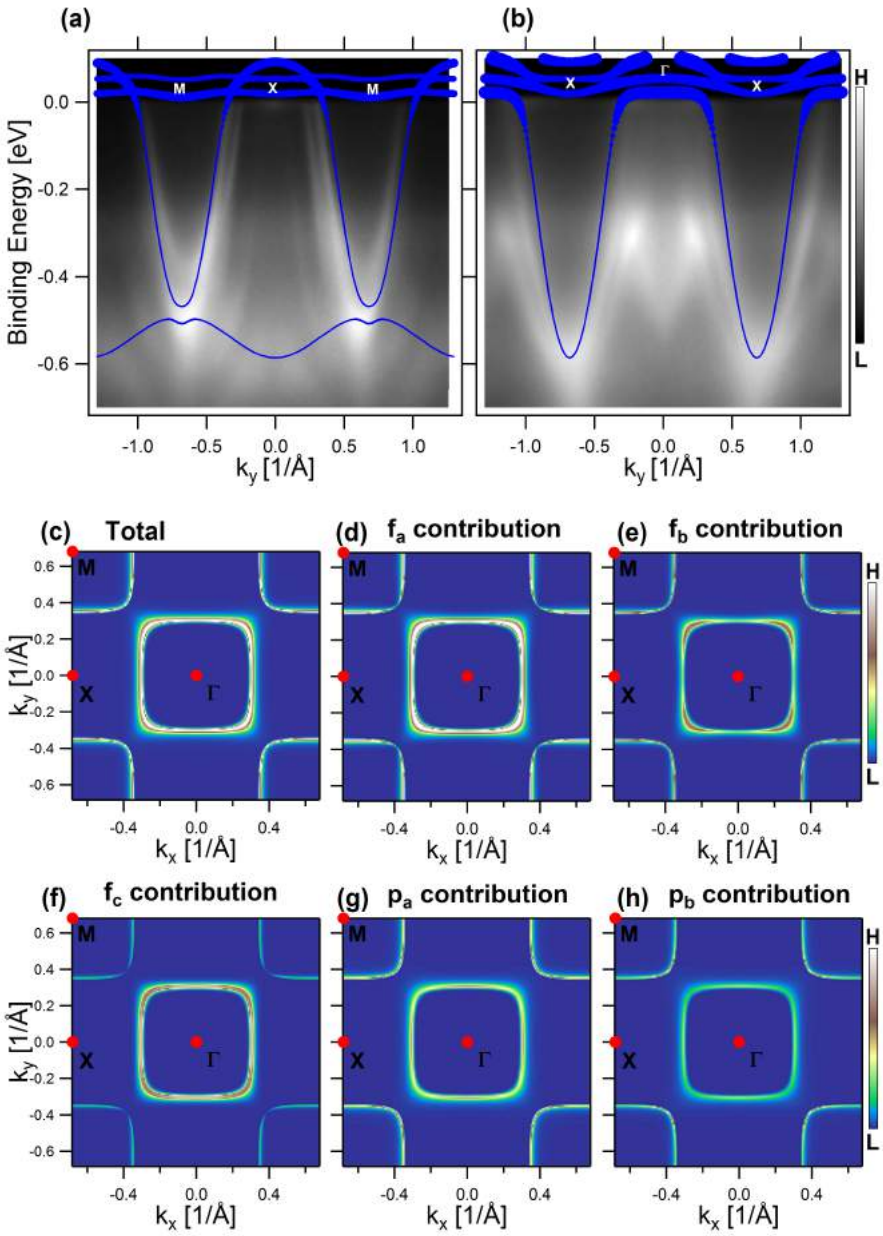

Figure 8.4: (Color on-line) Theoretical band structure for Ce-In planes (solid lines) obtained by tight-binding (TB) calculations with. TB parameters have been adjusted by fitting theoretical bands to ARPES data. The comparison of fitted model with the spectra collected along M-X-M (a) and X-Γ-X direction is shown. The marker size is proportional to the contribution of f orbital to the band. Panel (c) shows the distribution of the spectral weight on the Fermi surface. The projections on different base states are shown in (d)-(h). The lorentzian broadening of 15 meV and cuttof by the Fermi function with temperature equal to 20 K were applied in order to plot such maps.

8.4 Conclusions

The electronic structure of $CeCoIn_5$ system has been studied with resonant ARPES at low temperature using Ce 4d-4f transition. The determined topography of band structure is in general agreement with that reported in previous studies. The thorough comparison between measured Fermi surface and the results of one-step model calculations assuming different surfaces shows that the Ce-In termination prevails in our experiment. In this work, we have focused on the hybridization effects V_{cf} between f-electrons and other valence band electrons. These effects include a presence of weakly dispersive

states near the Fermi energy and strong broadening of bands close to the Γ point. The spectra reveal important band dependency of the hybridization. A comparison with theoretical calculations shows that the most significant hybridization effects present in the spectra, are related to Ce-In planes. We observe a significant variation of f-electron spectral intensity in momentum space, originating from both, matrix element effects and momentum dependent V_{cf} hybridization. A symmetrization of FS obtained experimentally in wide angular range allows to separate these effects and extract the momentum dependence of f-electron intensity related to a form of V_{cf}. The same dependence of f-electron density is reproduced by tight-binding model calculations for a variety of parameters, what confirms that real variation of f-electron density has been found. This gives an experimental insight in the structure of V_{cf}.

Bibliography

Chen, Q. Y., Xu, D. F., Niu, X. H., Jiang, J., Peng, R., Xu, H. C., Wen, C. H. P., Ding, Z. F., Huang, K., Shu, L., Zhang, Y. J., Lee, H., Strocov, V. N., Shi, M., Bisti, F., Schmitt, T., Huang, Y. B., Dudin, P., Lai, X. C., Kirchner, S., Yuan, H. Q., and Feng, D. L. (2017). *Phys. Rev. B*, 96:045107.

Danzenbächer, S., Kucherenko, Y., Heber, M., Vyalikh, D. V., Molodtsov, S. L., Servedio, V. D. P., and Laubschat, C. (2005). *Phys. Rev. B*, 72:033104.

Dudy, L., Denlinger, J. D., Shu, L., Janoschek, M., Allen, J. W., and Maple, M. B. (2013). *Phys. Rev. B*, 88:165118.

Ebert, H., Ködderitzsch, D., and Minár, J. (2011). *Rep. Prog. Phys.*, 74(9):096501.

Garnier, M., Purdie, D., Breuer, K., Hengsberger, M., and Baer, Y. (1997). *Phys. Rev. B*, 56:R11399–R11402.

Ghaemi, P., Senthil, T., and Coleman, P. (2008). *Phys. Rev. B*, 77:245108.

Jang, S., Denlinger, J. D., Allen, J. W., Zapf, V. S., Maple, M. B., Nyeong Kim, J., Jang, B. G., and Shim, J. H. (2017). . *arXiv e-prints*, page arXiv:1704.08247.

Jia, X.-W., Liu, Y., Yu, L., He, J.-F., Zhao, L., Zhang, W.-T., Liu, H.-Y., Liu, G.-D., He, S.-L., Zhang, J., Lu, W., Wu, Y., Dong, X.-L., Sun, L.-L., Wang, G.-L., Zhu, Y., Wang, X.-Y., Peng, Q.-J., Wang, Z.-M., Zhang, S.-J., Yang, F., Xu, Z.-Y., Chen, C.-T., and Zhou, X.-J. (2011). *Chin. Phys. Lett.*, 28(5):057401.

Klein, M., Nuber, A., Schwab, H., Albers, C., Tobita, N., Higashiguchi, M., Jiang, J., Fukuda, S., Tanaka, K., Shimada, K., Mulazzi, M., Assaad, F. F., and Reinert, F. (2011). *Phys. Rev. Lett.*, 106:186407.

Koitzsch, A., Kim, T. K., Treske, U., Knupfer, M., Büchner, B., Richter, M., Opahle, I., Follath, R., Bauer, E. D., and Sarrao, J. L. (2013). *Phys. Rev. B*, 88:035124.

Kumagai, K., Saitoh, M., Oyaizu, T., Furukawa, Y., Takashima, S., Nohara, M., Takagi, H., and Matsuda, Y. (2006). *Phys. Rev. Lett.*, 97:227002.

Maehira, T., Hotta, T., Ueda, K., and Hasegawa, A. (2003). *J. Phys. Soc. Jpn.*, 72(4):854–864.

Paglione, J., Tanatar, M. A., Hawthorn, D. G., Boaknin, E., Hill, R. W., Ronning, F., Sutherland, M., Taillefer, L., Petrovic, C., and Canfield, P. C. (2003). *Phys. Rev. Lett.*, 91:246405.

Petrovic, C., Pagliuso, P. G., Hundley, M. F., Movshovich, R., Sarrao, J. L., Thompson, J. D., Fisk, Z., and Monthoux, P. (2001). *J. Phys. Condens. Matter*, 13(17):L337–L342.

Sekiyama, A., Iwasaki, T., Matsuda, K., Saitoh, Y., Onuki, Y., and Suga, S. (2000). *Nature*, 403(6768):396–398.

Shimozawa, M., Goh, S. K., Shibauchi, T., and Matsuda, Y. (2016). *Rep. Prog. Phys.*, 79(7):074503.

Slater, J. C. and Koster, G. F. (1954). *Phys. Rev.*, 94:1498–1524.

Starowicz, P., Kurleto, R., Goraus, J., Schwab, H., Szlawska, M., Forster, F., Szytuła, A., Vobornik, I., Kaczorowski, D., and Reinert, F. (2014). *Phys. Rev. B*, 89:115122.

Steglich, F. and Wirth, S. (2016). *Rep. Prog. Phys.*, 79(8):084502.

Stewart, G. R. (1984). *Rev. Mod. Phys.*, 56:755–787.

Tahvildar-Zadeh, A. N., Jarrell, M., and Freericks, J. K. (1998). *Phys. Rev. Lett.*, 80:5168–5171.

Thompson, J., Nicklas, M., Bianchi, A., Movshovich, R., Llobet, A., Bao, W., Malinowski, A., Hundley, M., Moreno, N., Pagliuso, P., Sarrao, J., Nakatsuji, S., Fisk, Z., Borth, R., Lengyel, E., Oeschler, N., Sparn, G., and Steglich, F. (2003). *Physica B Condens. Matter*, 329-333:446 – 449. Proceedings of the 23rd International Conference on Low Temperature Physics.

W. Allen, J. (2005). *J. Phys. Soc. Jpn.*, 74(1):34–48.

Supplementary material

Band structure of $CeCoIn_5$ calculated along high symmetry directions using DFT method

Calculated Bloch spectral function for $CeCoIn_5$ along high symmetry directions is shown in (Fig. 8.5 c-l). Projection on different atoms in unit cell were calculated. Two types of calculations have been performed: with 4f electrons in valence band ("4f in VB") and with 4f electrons excluded from the valence band ("4f in core"). The results obtained with the second approach can be interpreted as the electronic structure in absence of hybridization effects. Therefore, the differences between results obtained in these two ways are directly related to the V_{cf} hybridization effects.

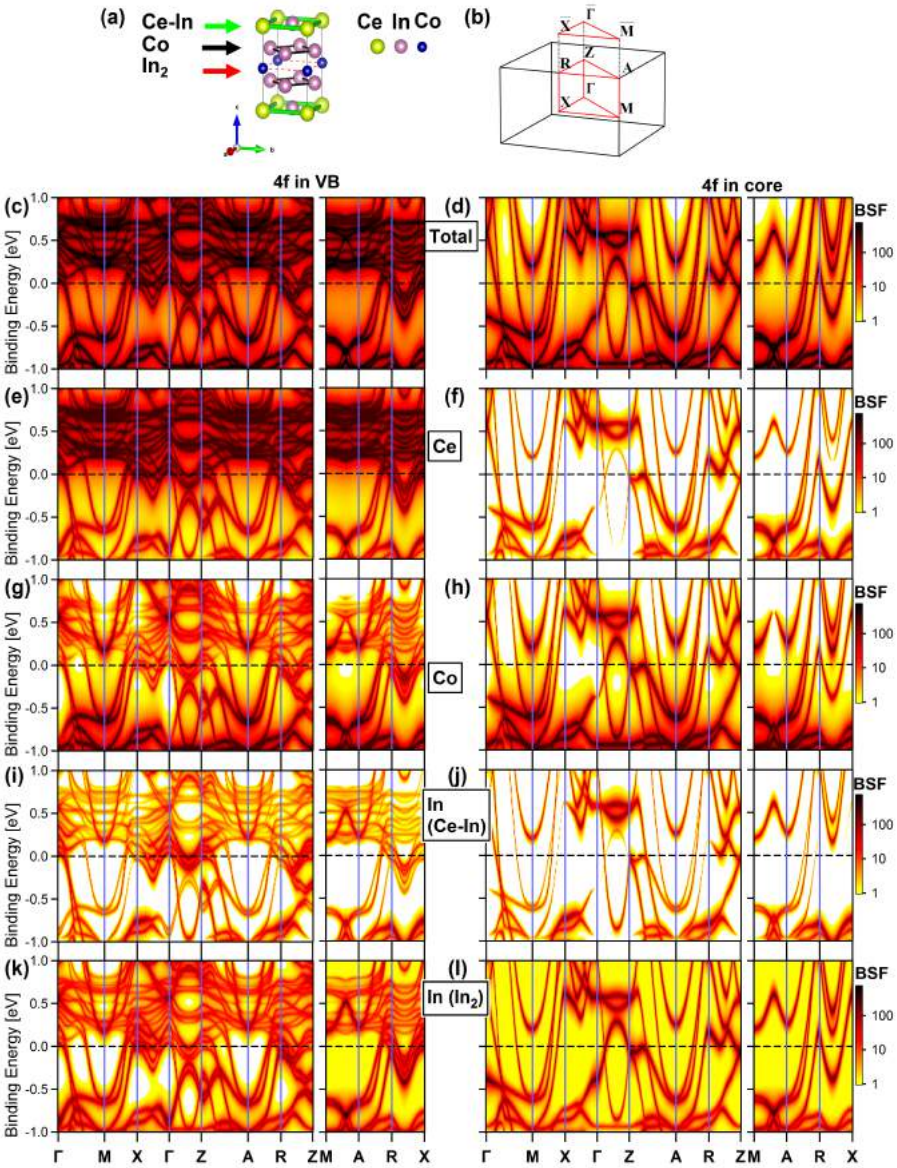

Figure 8.5: (Color on-line) Bloch spectral function calculated along high symmetry directions in the BZ. (a) The crystal structure of $CeCoIn_5$ with characteristic structural features. (b) The first Brillouin zone with marked high symmetry points. Two types of calculations are provided: with included hybridization between 4f states and rest of orbitals (c), as well as the results without the hybridization (4f in core) (d). The projection on Ce (e,f), Co (g,h), In from Ce-In planes (i,j) and In form In planes (k,l) are also provided.

Description of TBA model fitted to ARPES data

In this paper we use previously proposed idea (Maehira et al., 2003) of description of essential features of electronic structure of $CeCoIn_5$ by a tight binding model (within generalized Slater Koster approach) for Ce-In layer. In and Ce atoms in such layers are arranged into NaCl-type lattice in 2D. In such an approach the missing Co and In atoms can be regarded as a charge reservoir, which possible leads to renormalization of band structure.

Spin orbit interaction, which is rather strong in case of heavy elements, reduces the degeneracy of 4f orbitals in Ce. In consequence two manifolds characterized by total momentum j equal to $5/2$ and $7/2$ appear. According to Hund's rules the ground state in case of Ce with one f electron is a manifold with $j = 5/2$. In case of In atoms electrons from partially filled 5p shell are important. It turns out that in case of Ce-In layer p orbitals $j_z = 0$ do not contribute to dispersive bands near the Fermi level. Therefore, we take into account only two doublets with $j_z = \pm 1$. Finally, our basis states consists of Ce $4f_{5/2}$ sextet and two doublets from In $5p_1$ manifold:

$$|p_a \uparrow> = -|m = 1, s = \uparrow> \qquad |p_a \downarrow> = |m = -1, s = \downarrow>$$

$$|p_b \uparrow> = -|m = -1, s = \uparrow> \qquad |p_b \downarrow> = |m = 1, s = \downarrow>$$

$$|f_a \uparrow> = -|j = 5/2, j_z = -5/2> \qquad |f_a \downarrow> = |j = 5/2, j_z = 5/2>$$

$$|f_b \uparrow> = -|j = 5/2, j_z = -1/2> \qquad |f_b \downarrow> = |j = 5/2, j_z = 1/2>$$

$$|f_c \uparrow> = -|j = 5/2, j_z = 3/2> \qquad |f_c \downarrow> = |j = 5/2, j_z = -3/2>$$

The interactions between orbitals at neighboring lattice sites can be described in terms of electron hopping through the respective bond. The final form of the Hamiltonian is following:

$$\begin{aligned}\mathscr{H} = &\left(\sum_{\substack{\xi=\sigma,\pi \\ \mathbf{i},\delta\mathbf{i},\sigma}} (pp\xi) \cdot \hat{p}^{\dagger}_{\mathbf{i}+\delta\mathbf{i},\sigma} \hat{T}^{(pp\xi)}_{\delta\mathbf{i}} \hat{p}_{\mathbf{i},\sigma} + \text{H.c.} \right) + \\ &\left(\sum_{\substack{\xi=\sigma,\pi,\delta,\phi \\ \mathbf{i},\delta\mathbf{i},\sigma}} (ff\xi) \cdot \hat{f}^{\dagger}_{\mathbf{i}+\delta\mathbf{i},\sigma} \hat{T}^{(ff\xi)}_{\delta\mathbf{i}} \hat{f}_{\mathbf{i},\sigma} + \text{H.c.} \right) + \\ &\left(\sum_{\substack{\xi=\sigma,\pi \\ \mathbf{i},\delta\mathbf{i},\sigma}} (pf\xi) \cdot \hat{p}^{\dagger}_{\mathbf{i}+\delta\mathbf{i},\sigma} \hat{V}^{(pf\xi)}_{\delta\mathbf{i},\sigma} \hat{f}_{\mathbf{i},\sigma} + \text{H.c.} \right) + \\ &\sum_{\mathbf{i},\sigma} \Delta_p \cdot \hat{p}^{\dagger}_{\mathbf{i},\sigma} \hat{p}_{\mathbf{i},\sigma},\end{aligned} \tag{8.1}$$

where ξ denotes the bond type ($\xi = \sigma, \pi, \delta, \phi$), $T^{pp\xi}_{\delta i}$ and $T^{ff\xi}_{\delta i}$ are hopping matrices (δi is a hopping range, in our case only nearest neighbor hopping was taken into account). $V^{pf\xi}_{\delta i,\sigma}$ is a p-f hybridization matrix (hopping between p and f orbitals). The explicit form of $T^{pp\xi}_{\delta i}$, $T^{ff\xi}_{\delta i}$ and $V^{pf\xi}_{\delta i,\sigma}$ can be written down using Clebsch-Gordan coefficients. Δ_p defines the location of an atomic p level with respect to f level. The symbols: $(pp\xi)$, $(ff\xi)$, $(pf\xi)$ are the Slater Koster integrals, which describe the strength

Table 8.1: Fit parameters and orbital occupancies for a model with non-zero $(pp\pi)$ integral.

Parameter	Value [eV]
$(pp\sigma)$	0.327
$(pp\pi)$	-0.038
$(ff\sigma)$	0.048
$(pf\sigma)$	0.114
μ	-0.035
Orbital	**Occupancy**
p_a	0.891
p_b	0.834
f_a	0.492
f_b	0.243
f_c	0.264

of the hopping between orbitals through ξ bond. In our analysis we perform fits taking into account exclusively σ bonds or σ bonds together with some p-p hopping through π bond. While the second approach results in better agreement between theoretical bands and experimental ARPES spectra near the Fermi level (Fig. 8.6), both give essentially similar distribution of spectral weight on the Fermi surface, which mimics well the experimental one.

Following assumptions have been made for a fitting procedure:

- quantity Δ_p has been fixed as 0.1 eV
- Slater Koster integrals: $(pp\sigma)$, $(pp\pi)$, $(ff\sigma)$, $(pf\sigma)$, together with chemical potential μ have been treated as free fit parameters
- the binding energy at X point determined has been taken from experiment: $E_B(\mathrm{X}) = -0.586$ eV
- the binding energy at M point determined has been taken from experiment: $E_B(\mathrm{M}) = -0.469$ eV
- the Fermi wave vector along Γ-X directions has been determined from experiment: $k_F(\Gamma\text{-X}) = 0.235$ Å^{-1}
- the Fermi wave vector along M-X directions has been determined from experiment: $k_F(\text{M-X}) = 0.32$ Å^{-1}
- mean occupancy of f orbital has been set as $n_f = 1$

Additionally, in case of a model with $(pp\pi) = 0$ it was possible to use a quantity Δ_p as a free fit parameter. The obtained fit parameters together with orbital occupancies are shown in Table 1. and Table 2. The results of TBA calculations corresponding to a model with $(pp\pi) = 0$ are shown in Fig. 8.6.

Table 8.2: Fit parameters and orbital occupancies for a model with $(pp\pi)$ integral set to 0.

Parameter	Value [eV]
$(pp\sigma)$	0.3255
$(ff\sigma)$	0.102
$(pf\sigma)$	0.262
μ	-0.112
Δ_p	0.239
Orbital	**Occupancy**
p_a	0.744
p_b	0.658
f_a	0.574
f_b	0.231
f_c	0.195

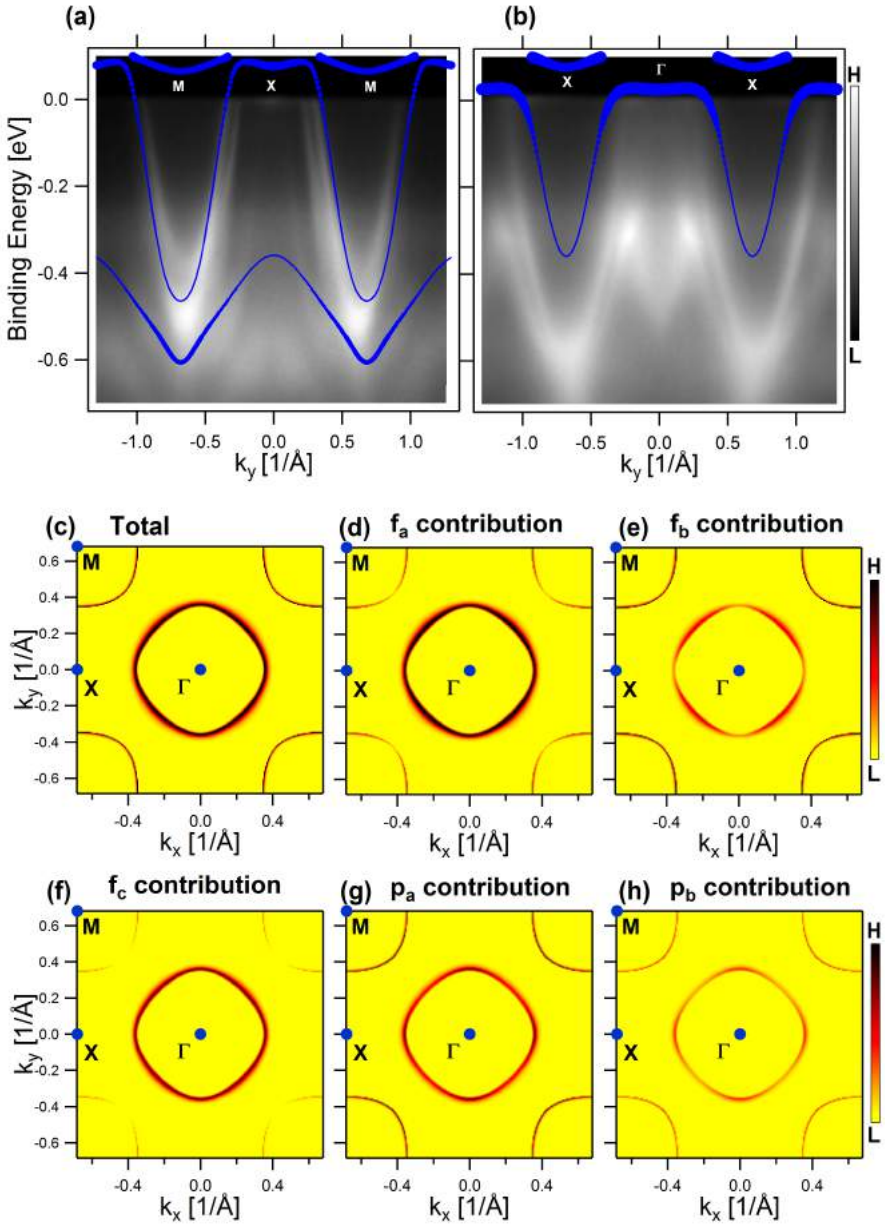

Figure 8.6: (Color on-line) Theoretical band structure for Ce-In planes (solid lines) obtained by tight-binding (TB) calculations. TB parameters have been adjusted by fitting theoretical bands to ARPES data with assumption $(pp\pi) = 0$. This is the alternative version of TBA fit model presented in Fig. 8.4. The comparison of fitted model with the spectra collected along M-X-M (a) and X-Γ-X direction is shown. The marker size is proportional to the contribution of f orbital to the band. Panel (c) shows the distribution of the spectral weight on the Fermi surface. The projections on different base states are shown in (d)-(h). The lorentzian broadening of 15 meV and cuttof by the Fermi function with temperature equal to 20 K were applied in order to plot such maps.

Chapter 9

Electronic Structure of the Ce_3PdIn_{11} Heavy Fermion Compound Studied by Means of Angle-resolved Photoelectron Spectroscopy

Highlights

- the band structure of the Ce_3PdIn_{11} heavy fermion superconductor is studied by means of ARPES for the first time
- the flat band close to the Fermi level has been observed in measurements performed at Ce 4d-4f resonant transition and temperature equal to 6 K
- ab initio calculations allow to distinguish contributions related to Ce 2g and Ce 1a atoms in the measured spectra
- it turns out that hybridization effects related to Ce 2g atoms are stronger that these related to Ce 1a atoms

Abstract

The electronic structure of heavy fermion compound Ce_3PdIn_{11}, which has got two inequivalent Ce atoms in the unit cell (Wyckoff positions: Ce 1a and Ce 2g, P4/mmm space group) has been studied by means of angle-resolved photoelectron spectroscopy. The flat band near the Fermi level has been observed in data collected at 6 K using incident radiation with energy corresponding to Ce 4d-4f resonant transition ($h\nu$ =122 eV). This band emerges as a result of mixing between 4f electrons and conduction carriers. The comparison with ab initio calculations suggests that the hybridization related to 4f orbitals at Ce 2g site is more effective than that related to orbitals at Ce 1a site.

9.1 Introduction

Intermetallic compounds of cerium are a testing ground for the studies of many intriguing physical phenomena due to the presence of weakly localized 4f electrons (Stewart, 1984). The strong Coulomb repulsion between electrons on the f orbital together with mixing between f orbitals and conduction band states lead to complex behavior of physical properties as a function of temperature. It is commonly believed that well above the coherence temperature the physics of such systems is dominated by local interactions (i.a. Kondo screening), which are described by single-impurity Anderson model (SIAM). On the other hand, below the coherence temperature the local description is not sufficient, because heavy quasiparticles emerge, and one has to use periodic Anderson model (PAM).

The photoelectron spectroscopy provides a direct insight into the spectral function of a system with strongly correlated f electrons (Klein et al., 2011; Sekiyama et al., 2000; W. Allen, 2005). It can be also used in order to track a crossover from the coherent regime to a local (Kondo) regime (Klein et al., 2011). The hallmark of the Kondo coherent state is a flat quasiparticle band, which is visible in the spectral function in the vicinity of the Fermi energy (ε_F) and can be identified with the aid of dynamical mean-field theory (DMFT) and Anderson model.

Ce_3PdIn_{11} crystallizes in tetragonal structure (space group P4/mmm) (Latturner, 2018; Tursina et al., 2013). It belongs to $Ce_mT_nIn_{3m+2n}$ family (T-transition metal), which displays a rich variety of ground states and allows for studies close to the quantum critical point (Matusiak et al., 2011; Paglione et al., 2016; Tokiwa et al., 2013; Urbano et al., 2007). Unit cell of each representative of this family is built of m layers of $CeIn_3$ and n layers of TIn_2 stacked along c-axis. Ce atoms occupy two inequivalent positions in the unit cell of Ce_3PdIn_{11}: Ce 1a and Ce 2g (cf. Fig. 9.1 a). Ce atoms at 1a positions have got the same chemical surrounding and symmetry (C_{4v} point symmetry) as Ce atoms in antiferromagnetic $CeIn_3$. On the other hand, Ce at 2g site shares the same chemical ordering (D_{4h} point symmetry) with Ce in the Ce_2PdIn_8 heavy fermion superconductor. Consequently, they are characterized by different sets of crystal field parameters and different Kondo couplings with conduction band. The presence of more than one inequivalent Ce atom per unit cell places Ce_3PdIn_{11} among heavy fermion compounds such as: Ce_5CuSb_3 (Tran, 2004b), Ce_5CuSn_3 (Tran, 2004a), Ce_7Ni_3 (Sereni et al., 1994), $Ce_5Ni_6In_{11}$ (Tang et al., 1995) and $Ce_3Pd_{20}Si_6$ (Custers et al., 2012; Strydom et al., 2006).

The complex magnetic phase diagram of Ce_3PdIn_{11} was a subject of thorough studies. It hosts heavy fermion superconductivity and antiferromagnetism (Das et al., 2019; Kratochvilova et al., 2015). The coherent heavy fermion state is observed below 20 K. There are two antiferromagnetic phase transitions at 1.68 K and 1.56 K. The superconducting state appears below 0.58 K. Interestingly, the realization of the field induced Lifshitz transition in Ce_3PdIn_{11} has been proposed (Das et al., 2019). It is supported by the behavior of specific heat as a function of magnetic field and temperature.

According to previous studies, anomalous properties of Ce_3PdIn_{11} at low temperature are directly related to the presence of two inequivalent Ce atoms in the unit cell (Kratochvilova et al., 2015). Such sublattices of Ce can be characterized by different Kondo scales. Consequently, different type of ordering can be realized in each sublattice at the same time. Such a proposition is in line with theoretical results (Benlagra et al., 2011) obtained for a system with two inequivalent Kondo sublattices. The non-trivial interplay between the Kondo effects in two sublattices together with complex phase diagram is predicted by this model. The standard Doniach diagram (Doniach, 1977), which describes the competition between RKKY interaction and the Kondo screening, is complemented i.a. by the partial screening phase. Such a phase is characterized by the presence of antiferromagnetic type ordering together with the heavy quasiparticles. On the another hand, one must have in mind, that the coexistence of antiferromagnetism and Kondo effect is not an exclusive feature of systems with inequivalent Ce sites. Such a situation is also realized in uranium compounds (e.g. USb_2) as a consequence of orbital selective Kondo effect (Giannakis et al., 2019).

In this paper we discuss the electronic structure of Ce_3PdIn_{11} measured with angle-resolved photoelectron spectroscopy (ARPES) method. The experimental results are compared with ab initio calculations. Some attempts on quantification of the influence of the hybridization between 4f electrons and conduction band are made. We also outline possible consequences of presence of two independent sublattices of Ce. We would like to provide some step in better understanding the relations between the crystal structure and the physical properties of Ce_3PdIn_{11} by means of an electronic structure measured with ARPES method. In this article we check: I) to what extent both independent Ce atoms in unit cell give rise to heavy fermion properties; II) if it is possible to quantify hybridization effects using a band structure measured with ARPES.

9.2 Material and methods

Single crystals of Ce_3PdIn_{11} have been grown using flux method. Their synthesis and characterization were described elsewhere (Das et al., 2019; Kratochvilova et al., 2014). ARPES measurements have been performed at the Cassiopee beamline of Soleil synchrotron. Samples were oriented by means of x-ray diffraction (Laue method). They were cleaved in ultra-high vacuum conditions (base pressure: $5{\cdot}10^{-11}$ mbar) prior to the measurements, exposing (001) crystallographic plane. The data have been collected at temperature equal to 6 K, using Scienta R4000 photoelectron energy analyzer. The incident radiation with linear polarization and energy corresponding to Ce 4d-4f resonant transition ($h\nu$=122 eV) has been applied. Overall resolution was equal to 15 meV. The electronic structure of Ce_3PdIn_{11} has been calculated using Korringa-Kohn-Rostoker (KKR) method in single particle Green function approach (Ebert et al., 2011) with application of multiple scattering theory. The spin polarized relativistic Korringa-Kohn-Rostoker (SPR-KKR) code for Calculating Solid State Properties has been used.

9.3 Results and Discussion

We have measured electronic structure of Ce_3PdIn_{11} using resonant ARPES near Ce 4d-4f absorption threshold, in order to study the relation of 4f orbitals to enigmatic properties of this system. The sample was oriented in such a way that the analyzer slit direction was parallel to the *a*-axis. The experimental geometry is shown in Fig. 9.1 b. The Fermi surface map in Γ-X-Z plane (see Brillouin zone in Fig. 9.1 c) has been obtained by performing measurements using incident radiation with different energies (Fig. 9.1 d). Several weakly dispersive features are visible. The intensities of these features are noncontinuous as a function of photon energy, probably due to significant variation of the cross section for the photoionization close to the absorption threshold. This fact together with almost two-dimensional character of observed bands makes that the reliable determination of the inner potential was impossible with the obtained data. On the other hand, one can expect that the three-dimensional bands, related to interlayer coupling, are also present in the electronic structure of Ce_3PdIn_{11}, what is supported by the results of theoretical calculations (Azam et al., 2014). However, they have not been observed in our particular experimental geometry. The spectra measured at different photon energies were compared with calculated bands along Γ-X and Z-R directions. They suggest that the photon energy equal to 98 eV corresponds to measurement in Γ-X-M plane. The Fermi surface map measured at Ce 4d-4f resonance is presented in (Fig. 9.1 e). The bands visible in the photon energy dependent scan are also identified. The measured Fermi surface is affected by the matrix elements, but not as much as that of $CeCoIn_5$ previously measured by us in the same geometry (more details about matrix elements effects are provided in *Supplementary information*).

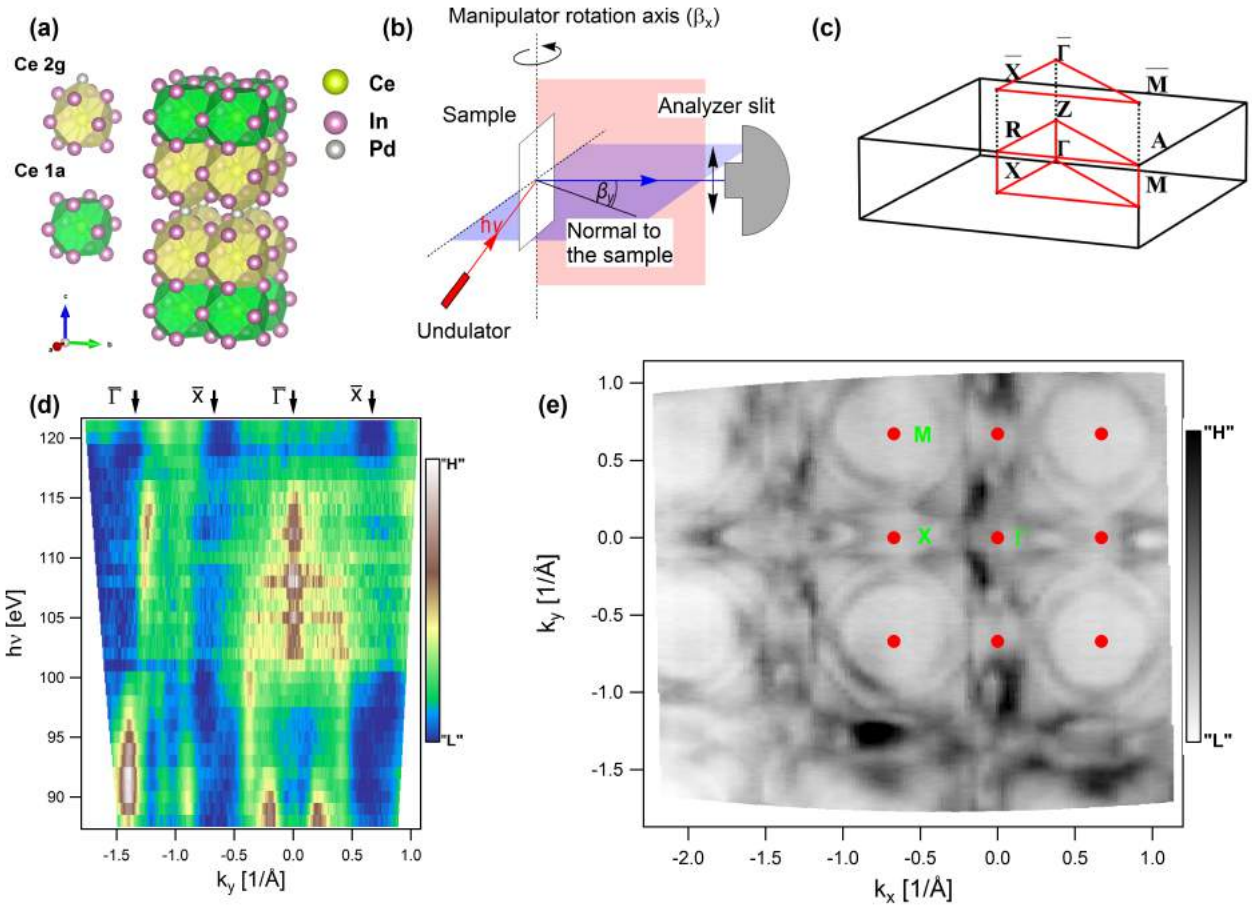

Figure 9.1: (Color on-line) (a) Crystal structure of Ce_3PdIn_{11}. The Ce 1a and Ce 2g coordination polyhedra are shown. (b) Schematic plot showing the experimental geometry for ARPES measurements. (c) The first Brillouin zone of Ce_3PdIn_{11}. (d) The map showing the measurement of the electronic structure of Ce_3PdIn_{11} as a function of photon energy. Values of k_y corresponding to high symmetry points are marked by black arrows. (e) The Fermi surface of Ce_3PdIn_{11} collected at wide region in k-space at temperature equal to 6 K using photon energy of 122 eV (Ce 4d-4f resonance).

The description of the electronic structure of Ce_3PdIn_{11} using measured ARPES spectra is a demanding task. The significant number of electron and hole bands is crossing a Fermi level. Measured FS map is similar with the Fermi surface topography obtained for other $Ce_mT_nIn_{3m+2n}$ compounds. In particular, the structure resembling the flower with four petals centered in Γ point has been observed in the cross section of FS (in Z-R-A plane) calculated for Ce_2PdIn_8. Additionally, the FS of Ce_2PdIn_8 consists of many disjoint parts (Werwiński et al., 2015). The crystal structure of Ce_3PdIn_{11} shares some similarities with that of Ce_2PdIn_8, so one can expect some similarities between their electronic structures. Further analogies with the electronic structures of compounds from the same family are also possible. The attention should be paid to the structures centered in the M corner of BZ ($k_x = \pm\frac{\pi}{a}$, $k_y = \pm\frac{\pi}{a}$). In our case, two sheets of FS are clearly visible close to the M point. Previously, such structures were observed e.g. for: $CeCoIn_5$, Ce_2PtIn_8 and Ce_2RhIn_8 and were assigned to the cylindrical, quasi two-dimensional parts of FS. On the other hand, highly corrugated, three dimensional parts of FS are present around Γ point. Interestingly, some studies suggests that heavy fermion properties are essentially related to 3D bands, while the quasi 2D bands almost do not hybridize with f states (Koitzsch et al., 2013). Our measurements show also significant enhancement of the signal around X point. Indeed, one can see some oval-like structure in this region. Similar shapes around X point were observed in the case of Ce_2IrIn_8 heavy fermion compound (Liu et al., 2019).

The electronic structure of Ce_3PdIn_{11} can be understood with the aid of the ab initio theoretical calculations. The calculated bands are in good agreement with the experimental ones as well as with those previously calculated (Azam et al., 2014) (see *Supplementary information* for more details).

The total Bloch spectral function as well as projections on Pd and both inequivalent Ce atoms have been calculated (Fig. 9.2 a-e) along high symmetry directions in the first Brillouin zone. A rough look at the band structures gives the impression that both Ce atoms give completely different contributions to spectral function.

In order to better visualize the difference between Ce 1a and Ce 2g contributions, we classified (Fig. 9.2 f) the electronic structure according to prevailing contribution of Ce 1a, Ce 2g and Pd states to the spectral function. (The In states were not taken into account to make an analysis simpler, however they can have important contribution in the region of interest - corresponding to the charts in Fig. 9.2 a-e. On the other hand one can expect large but rather uniform contribution of In atoms in this energy region.) One can see clearly that in principle the Pd states are important only below -1.5 eV. Above -0.5 eV the Ce contribution is significant. The close region of the Fermi level is dominated by the contribution from the Ce 2g states, what points to their anticipated role in heavy fermion properties of Ce_3PdIn_{11}. However, there are some features crossing the Fermi level, with dominating Ce 1a character. The differences in contribution from both Ce sublattices are well visible in the distributions of BSF at the Fermi level (Fig. 9.2 g-k). Despite the complicated topography of the Fermi surface, one can see that there are some regions in the BZ where the contributions to BSF from both, Ce 1a and Ce 2g, can be clearly separated. Such an observation opens a way to describe a Ce_3PdIn_{11} in terms of non-trivial interplay between two Kondo sublattices (Benlagra et al., 2011). The performed classification of the FS according to Ce 2g, Ce 1a and Pd (with In contribution excluded from the analysis) states is shown in Fig. 9.2 l. One can see the oval like structure around X point, which is elongated along X-Γ direction. It originates mainly from Ce 1a states. Such a structure is related to the shallow electron pocket. On the other hand, when one looks at the X-M direction in the FS some petals are visible around aforementioned oval. These are characterized by the dominating contribution coming from Ce 2g. Interestingly, around M point one can observe nearly circular shape. In fact there are two electron pockets with bottoms roughly located at binding energy of about -0.7 eV. The outer one is dominated by contribution from Ce 1a sublattice, while the inner pocket is built mainly from Ce 2g states. It is also noteworthy, that that according to Fig. 9.2 f the significant contribution to spectral function from Ce 1a states is visible in Γ-Z direction. These states are giving a rise to flat, non-dipersive feature which is located directly at the Fermi energy.

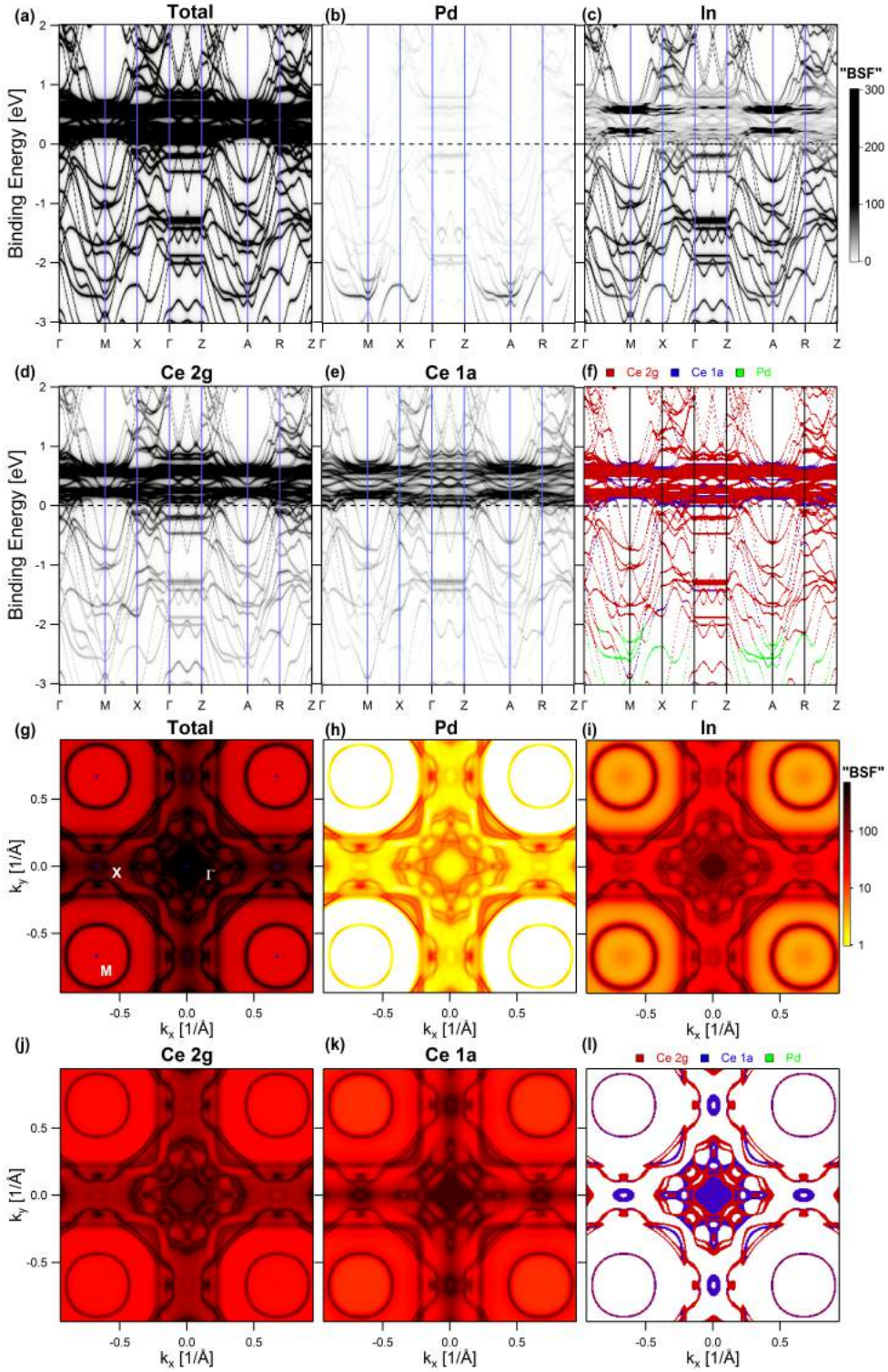

Figure 9.2: (Color on-line) The electronic structure of Ce_3PdIn_{11} calculated using KKR method. Bloch spectral function (a) was projected on different atoms (b)-(e) along high symmetry directions. (f) Band structure classified according to the contribution from Ce 1a, Ce 2g and Pd atoms. Red color corresponds to states characterized by contribution to BSF from Ce 1a greater than that from Ce 2g and Pd. Similarly, blue and green colors are related to Ce 2g and Pd states, respectively. (g)-(k) the distribution of BSF at the Fermi surface. (l) Fermi surface classified using the same method as for picture (f).

In figure Fig. 9.3 a we show the experimental band structure of Ce_3PdIn_{11}. The FS map measured

with high resolution in a small purview of k-space is shown Fig. 9.3 b. The weakly visible sheets around M point have been marked by lines (red and blue dashed lines).We have thoroughly inspected the spectra corresponding to X-M and Γ-X directions (Fig. 9.3 c and d). Two hole pockets (α, β) centered at X are clearly visible. The outer (α) one follows parabolic relation dispersion for ε_B between -0.25 eV and -0.01 eV. Close to ε_F, it seems to bend more rapidly toward the X point (i.e. it is more flat), but it is rather clear that it crosses the Fermi level according to our analysis of momentum distribution curves. On the other hand, it is difficult to describe the inner pocket (β) by the simple quadratic dispersion. Below ε_F the dispersion β band seems to be almost linear, while very close to the Fermi level it rapidly changes its shape and becomes almost flat. Such a behavior is a result of a hybridization with f states and has been observed for many Ce systems and interpreted successfully using Anderson model (Im et al., 2008). It is difficult to asses if this band crosses the Fermi level using our data. It is most probably that the top of β pocket touches the Fermi level or locates several milielectronovolts above, still giving a hot spot on FS map. Such a configuration of β and α bands recalls the idea of renormalization of point-like Fermi surface proposed for some uranium compound (Durakiewicz et al., 2008). However, we reckon that our data are not sufficient to push forward full analogy with this scenario, which also incorporates the presence of the kink in the dispersion of the outer band. In Fig. 9.3 c and d we marked the points in the k-space at which the band should cross the Fermi level (the red and blue dots stand for Ce 1a and Ce 2g, respectively; the area of the dot means the contribution to the total BSF, the offset of -0.2 eV and -0.18 eV is used for clarity). It turns out that β band close to ε_F is dominated by Ce 1a contribution, while the Ce 2g contribution plays a crucial role in the case of α pocket.

In order to visualize better the dispersion of the hole bands around X point we have calculated the curvature in MDC direction (Zhang et al., 2011) (Fig. 9.1 d and f). Such an approach indeed makes the α and β band clearly visible. However, one has to have in mind that the disadvantage of this procedure is that it removes any non-dispersive feature (i.e. k-independent) from the spectra. We have also tried to calculate full two-dimensional curvature of ARPES spectra, but we did not obtain results with sufficient quality for further analysis. The calculated curvature in the X-M direction was used to determine the band dispersion for α and β bands. Subsequently we have fitted the band using quadratic function in the widest range of energy still providing reasonable good quality of fits. The fits are marked by solid black lines in Fig. 9.3 c. The black dashed lines indicates the extrapolation of fitted function. The fits yield the effective masses equal to $0.8m_e$ and $0.23m_e$ (m_e - free electron mass) for α and β band, respectively. However, these values are valid well below ε_F (ε_B<-35 meV), because the experimental dispersion strongly deviates from that predicted by parabolic fits. Indeed, the fitted functions suggest that both β and α band crosses the Fermi level, while actually one cannot make such a statement about β band because it becomes very flat close to ε_F. However, one may notice, that the higher effective mass has been determined for the band which is related mainly to Ce 2g sublattice. Therefore, we may expect that the states from this sublattice are crucial to fermion properties (i.e. the enhanced value of Sommerfeld coefficient) and participates in a formation of a flat band near the Fermi level at low temperature. The deviation from parabolic dispersion relation and the mass enhancement due to c-f hybridization is further analyzed in *Supplementary information* using recently proposed method (Rosmus et al., 2019).

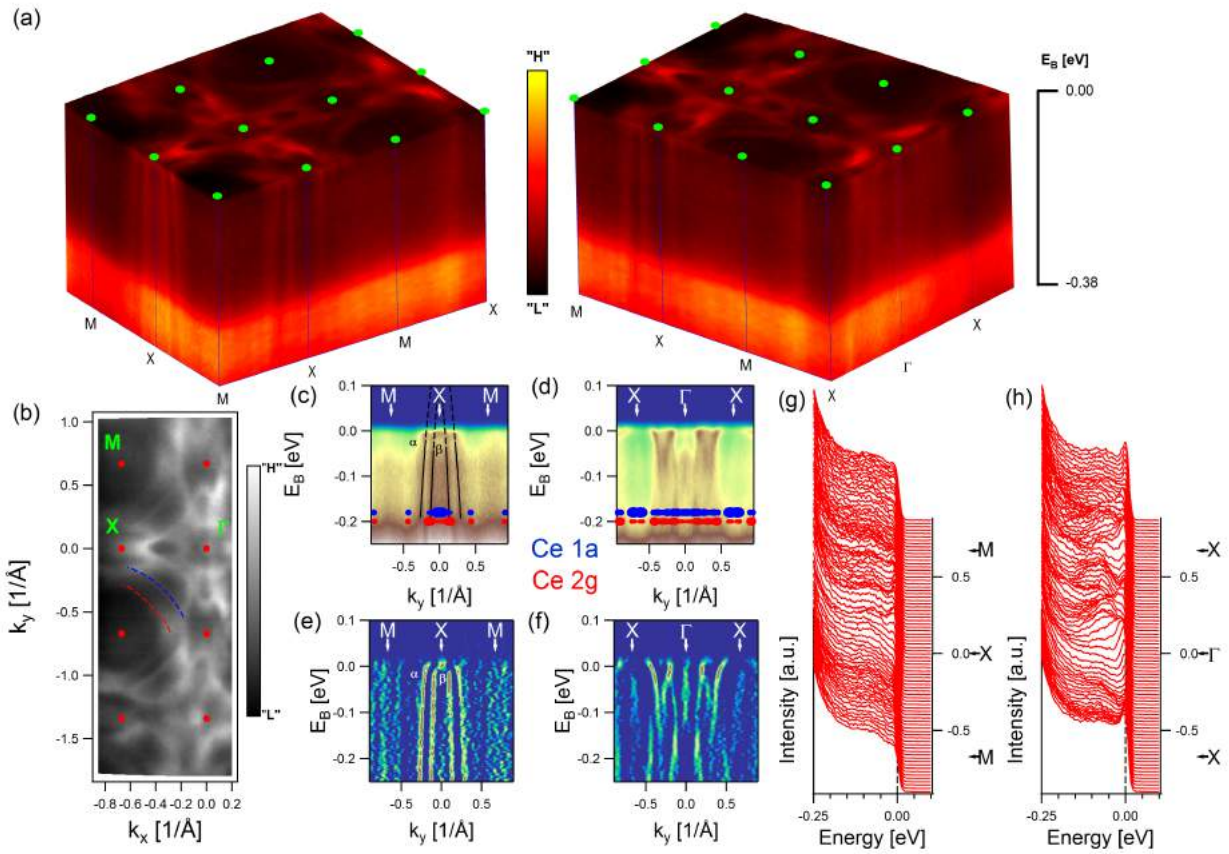

Figure 9.3: (Color on-line) The electronic structure of Ce_3PdIn_{11} obtained by ARPES at 6 K using photon energy of 122 eV. (a) 3D plot showing the band structure of Ce_3PdIn_{11} from different points of view in a wide region in k-space. (b) The Fermi surface of Ce_3PdIn_{11} measured with high resolution in a narrow region of the k-space. The weakly visible sheets of FS around M point are marked by red and blue dashed lines in order to guide the eyes. (c)-(d) The band structure near the Fermi level is shown along high symmetry directions (X-M and Γ-X). The contributions of different Ce sublattices to spectral function have been marked by dots (Ce 1a - red dots, Ce 2g - blue dots, the radius of the dot is proportional to the contribution to spectral function, the offset of -0.2 eV and -0.18 eV is used for better clarity) (e)-(f) MDC curvature calculated for spectra from (c) and (d). (g)-(h) Energy distribution curves showing the spectra collected along X-M and Γ-X directions.

9.4 Conclusions

We have provided the electronic structure of Ce_3PdIn_{11} in the paramagnetic state by means of ARPES. This is the first study of an electronic of Ce intermetallic with two inequivalent Ce sublattices employing photoelectron spectroscopy, according to our knowledge. Our results show that Ce_3PdIn_{11} can be to some extent regarded as a quasi two-dimensional system. Electronic structure calculations (KKR method) reproduced well observed bands of Ce_3PdIn_{11} and allow to distinguish the contributions from Ce 1a and Ce 2g inequivalent atoms in the unit cell. We have assessed that the enhancement of Sommerfeld coefficient of this system is mainly an effect of band hybridization with f states from Ce 2g site. On the other hand, we reckon that further studies concerning Ce_3PdIn_{11} are still necessary. The systematic ARPES measurements performed as a function of temperature complemented by some technique probing local electronic structure would allow to better understand the interplay of the two Kondo scales in this system.

Bibliography

Azam, S., Khan, S. A., Shah, F. A., Muhammad, S., Din, H. U., and Khenata, R. (2014). *Intermetallics*, 55:184 – 194.

Benlagra, A., Fritz, L., and Vojta, M. (2011). *Phys. Rev. B*, 84:075126.

Custers, J., Lorenzer, K.-A., Mueller, M., Prokofiev, A., Sidorenko, A., Winkler, H., Strydom, A. M., Shimura, Y., Sakakibara, T., Yu, R., Si, Q., and Paschen, S. (2012). *Nat. Mater.*, 11(3):189–194.

Das, D., Gnida, D., and Kaczorowski, D. (2019). *Phys. Rev. B*, 99:054425.

Doniach, S. (1977). *Physica B & C*, 91:231–234.

Durakiewicz, T., Riseborough, P. S., Olson, C. G., Joyce, J. J., Oppeneer, P. M., Elgazzar, S., Bauer, E. D., Sarrao, J. L., Guziewicz, E., Moore, D. P., Butterfield, M. T., and Graham, K. S. (2008). *EPL*, 84(3):37003.

Ebert, H., Ködderitzsch, D., and Minár, J. (2011). *Rep. Prog. Phys.*, 74(9):096501.

Giannakis, I., Leshen, J., Kavai, M., Ran, S., Kang, C.-J., Saha, S. R., Zhao, Y., Xu, Z., Lynn, J. W., Miao, L., Wray, L. A., Kotliar, G., Butch, N. P., and Aynajian, P. (2019). *Sci. Adv.*, 5(10).

Im, H. J., Ito, T., Kim, H.-D., Kimura, S., Lee, K. E., Hong, J. B., Kwon, Y. S., Yasui, A., and Yamagami, H. (2008). *Phys. Rev. Lett.*, 100:176402.

Klein, M., Nuber, A., Schwab, H., Albers, C., Tobita, N., Higashiguchi, M., Jiang, J., Fukuda, S., Tanaka, K., Shimada, K., Mulazzi, M., Assaad, F. F., and Reinert, F. (2011). *Phys. Rev. Lett.*, 106:186407.

Koitzsch, A., Kim, T. K., Treske, U., Knupfer, M., Büchner, B., Richter, M., Opahle, I., Follath, R., Bauer, E. D., and Sarrao, J. L. (2013). *Phys. Rev. B*, 88:035124.

Kratochvilova, M., Dusek, M., Uhlirova, K., Rudajevova, A., Prokleska, J., Vondrackova, B., Custers, J., and Sechovsky, V. (2014). *J. Cryst. Growth*, 397:47 – 52.

Kratochvilova, M., Prokleska, J., Uhlirova, K., Tkac, V., Dusek, M., Sechovsky, V., and Custers, J. (2015). *Sci. Rep.*, 5.

Latturner, S. E. (2018). *Acc. Chem. Res.*, 51(1):40–48.

Liu, H., Xu, Y., Zhong, Y., Guan, J., Kong, L., Ma, J., Huang, Y., Chen, Q., Chen, G., Shi, M., Yang, Y.-F., and Ding, H. (2019). *Chin. Phys. Lett.*, 36(9):097101.

Matusiak, M., Gnida, D., and Kaczorowski, D. (2011). *Phys. Rev. B*, 84:115110.

Paglione, J., Tanatar, M. A., Reid, J.-P., Shakeripour, H., Petrovic, C., and Taillefer, L. (2016). *Phys. Rev. Lett.*, 117:016601.

Rosmus, M., Kurleto, R., Gawryluk, D. J., Goraus, J., Cieplak, M. Z., and Starowicz, P. (2019). *Supercond. Sci. and Tech.*, 32(10):105009.

Sekiyama, A., Iwasaki, T., Matsuda, K., Saitoh, Y., Onuki, Y., and Suga, S. (2000). *Nature*, 403(6768):396–398.

Sereni, J., Trovarelli, O., Kappler, J., Paschke, C., Trappmann, T., and Löhneysen, H. (1994). *Physica B Condens. Matter*, 199-200:567 – 569.

Stewart, G. R. (1984). *Rev. Mod. Phys.*, 56:755–787.

Strydom, A. M., Pikul, A., Steglich, F., and Paschen, S. (2006). *J. Phys. Conf. Ser.*, 51:239–242.

Tang, J., Gschneidner, K. A., White, S. J., Roser, M. R., Goodwin, T. J., and Corruccini, L. R. (1995). *Phys. Rev. B*, 52:7328–7333.

Tokiwa, Y., Bauer, E. D., and Gegenwart, P. (2013). *Phys. Rev. Lett.*, 111:107003.

Tran, V. (2004a). *J. Alloys Compd.*, 383(1):281 – 285.

Tran, V. H. (2004b). *Phys. Rev. B*, 70:094424.

Tursina, A., Nesterenko, S., Seropegin, Y., Noël, H., and Kaczorowski, D. (2013). *J. Solid State Chem.*, 200:7 – 12.

Urbano, R. R., Young, B.-L., Curro, N. J., Thompson, J. D., Pham, L. D., and Fisk, Z. (2007). *Phys. Rev. Lett.*, 99:146402.

W. Allen, J. (2005). *J. Phys. Soc. Jpn.*, 74(1):34–48.

Werwiński, M., Szajek, A., Ślebarski, A., and Kaczorowski, D. (2015). *J. Alloys Compd.*, 647:605 – 611.

Zhang, P., Richard, P., Qian, T., Xu, Y.-M., Dai, X., and Ding, H. (2011). *Rev. Sci. Instrum.*, 82(4).

Supplementary information

Comparison of different theoretical calculations and experimental results.

In Fig. 9.4 we show the comparison between our theoretical calculations and these published previously (Azam et al., 2014). The previous calculations were obtained using the full potential linearized augmented plane wave (FP-LAPW) method based on density functional theory (DFT) implemented in WIEN2K code. In case of Γ-M and X-M directions the agreement is very good. For Z-R direction some significant differences between both versions of calculations are visible. In Fig. 9.4 d, we superimposed previous calculations on the measured band structure with ARPES along X-M direction. One can see that the outer hole pocket (α band) around X point is quite well reproduced. On the other hand, it is quite difficult to describe the inner pocket (β band) using these calculations. Maybe after some rescaling in k-vector and shift in energy scale one can achieve the agreement between theory and experiment.

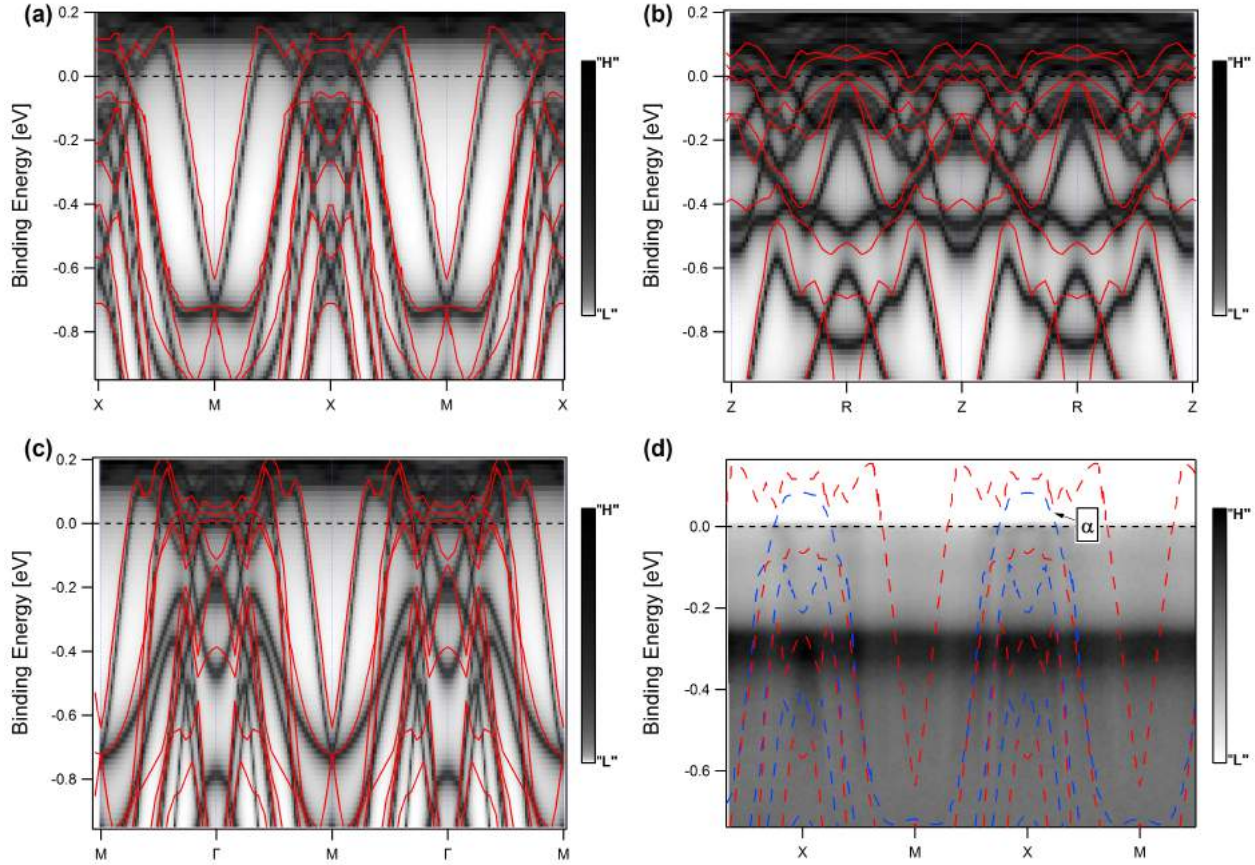

Figure 9.4: (Color on-line) (a)-(c) Comparison of theoretical band structures of Ce_3PdIn_{11} obtained with different methods. The previous results (Azam et al., 2014) were digitalized (red lines) and superimposed on the Bloch spectral function (gray scale, color maps) calculated using KKR approach for several directions in the first Brillouin zone. (d) Comparison between measured band structure (gray scale, color map) of Ce_3PdIn_{11} along M-X direction and theoretical calculations (red and blue dashed lines) available in the literature (Azam et al., 2014) (the curves are shown in different colors only for better readability). The α symbol denotes the outer hole band, which is discussed in the text. The experimental data have been collected at 6 K using photon energy of 122 eV (Ce 4d-4f resonance).

Mass enhancement in bands around X point

In Fig. 9.3 c we have presented the spectrum along X-M together with fitted relation dispersion to both α and β bands in some energy region below ε_B. One can notice that close to the Fermi level the band dispersion deviates from that predicted by extrapolation of fits (dashed lines in Fig. 9.3 c). In order to quantify this deviation we have analyzed the shape of the experimental dispersion thoroughly. Namely, we have defined the quantity μ in a following manner:

$$\mu = \hbar^2 k \frac{dk}{dE}. \tag{9.1}$$

Such a quantity can be interpreted as an effective mass in case of parabolic relation dispersion. In other cases it can be used to quantify the wave vector depended mass enhancement effects. Moreover such definition of μ is particularly useful when the dispersion is obtained from MDC profiles, because it allows to get rid of problems with singularities during calculation of derivative. We have calculated μ for both α and β band using the branch of dispersion corresponding to negative values of wave vector. We also made some attempts on calculation μ using the second branch of dispersion or both of them, but significant noise in data make results in poor quality of final output. Fig. 9.5 shows μ obtained in such a way in the units of free electron mass. Blue and red dots denote the values obtained for β and α bands, respectively. We have also marked the values of effective masses (m_α, m_β) obtained from parabolic fits by blue (β band) and red (α band) dashed lines.

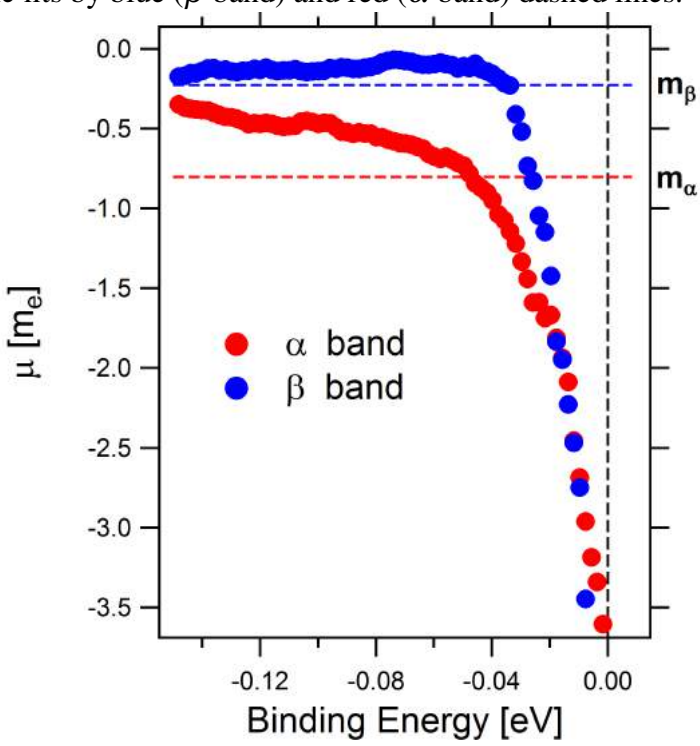

Figure 9.5: (Color on-line) The quantity μ defined by eq. 9.1 calculated for hole pockets around X point (the free electron mass m_e units are used). The red and blue dots correspond to α and β bands, respectively. The dashed lines denote the values obtained from fitting parabolic relation dispersion to ARPES data for higher binding energies. (cf. Fig. 9.3 c)

One can see that determined values of μ for β band are close to the m_β value below -30 meV. Above such a value of binding energy one can see the rapid change in a shape of μ as a function of k. The absolute value of μ rapidly rises with wave vector approaching zero, becoming about three and half times greater than the mass of free electron in vacuum. Such a behavior is directly related to the mass enhancement close to the Fermi level, which has a source in strong hybridization between s, p, d states and 4f orbitals. Similar behavior is also visible in the case of α band. However, the values

of μ corresponding to this band seem to deviate significantly from m_α. Probably taking into account both branches of dispersion relation would improve the agreement. On the other hand, similarly as for β band the rapid enhancement of effective mass close the Fermi energy (above -40 meV) can be deduced from obtained μ values. It is noteworthy that for both, α and β band, μ is lower than the mass of free electron well below the ε_F, while close to the Fermi energy it is several times greater. This fact is reflected in a very rapid change of the slope of the dispersion relation.

Matrix element effects

The obtained ARPES spectra of Ce_3PdIn_{11} are slightly affected by matrix elements effects. In order to visualize this effect we analyze some cuts of the band structure corresponding to high symmetry directions in the k-space. After a glance at Fig. 9.6 b, one can notice that the hole bands at X point corresponding to k_y=0 are clearly visible, while they are almost difficult to resolve around second X point, at $k_y = \frac{\pi}{a}$. The opposite effect is visible in Fig. 9.6 d and f, which show the cut along X-M directions corresponding to different values of k_x. Similar effects are visible along Γ-X direction (Fig. 9.6 c and e). We have checked that this effect is independent of applied normalization procedure, therefore it is not an artifact produced during data analysis.

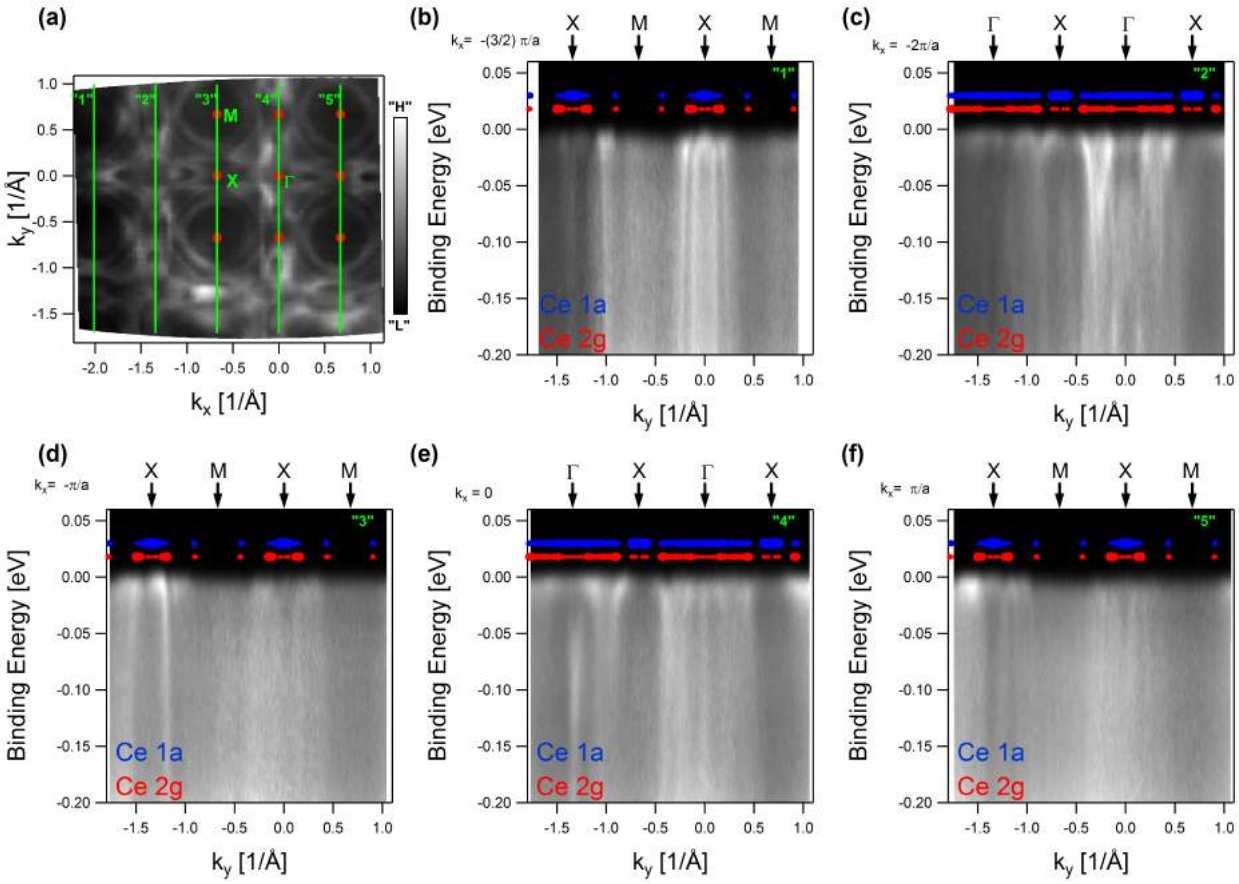

Figure 9.6: (Color on-line) The electronic structure of Ce_3PdIn_{11} measured by ARPES at 6 K. (a) The Fermi surface measured in a wide k-space region. Some high symmetry directions have been marked. (b)-(f) Band structure of Ce_3PdIn_{11} along directions marked by green lines on FS. The Ce 1a and Ce 2g contributions to the spectral function at ε_F have been marked by the marker size. Offsets of 0.03 eV and 0.018 eV have been used for better readiness.

In Fig. 9.2 f and l we have shown the result of classification of the band structure according to dominating contribution of Ce 1a, Ce 2g or Pd states to the full spectral function. Such an approach is useful if one wants to separate the regions of k-space where the contribution from particular atom is dominating. However, such a procedure has got some drawbacks. Namely, it cannot give conclusive

answer in the regions of BZ where the contributions of Ce 1a and Ce 2g are similar. In order to be sure, that we did not make wrong interpretation of calculated BSF, here we define a different measure allowing to separate Ce 1a and Ce 2g contributions. Namely, we have calculated a simple difference Δ between BSF projected on both sublattices:

$$\Delta = \mathrm{BSF}(\mathrm{Ce\ 2g}) - \mathrm{BSF}(\mathrm{Ce\ 1a}).$$

The result is shown in Fig. 9.7. After the analysis of this figure one can come to the conclusions, which are essentially the same as these obtained using classified band structure. However, the simple difference gives result which allows for more detailed analysis of some subtle differences in Ce 1a and Ce 2g contributions, which are present near the Γ point.

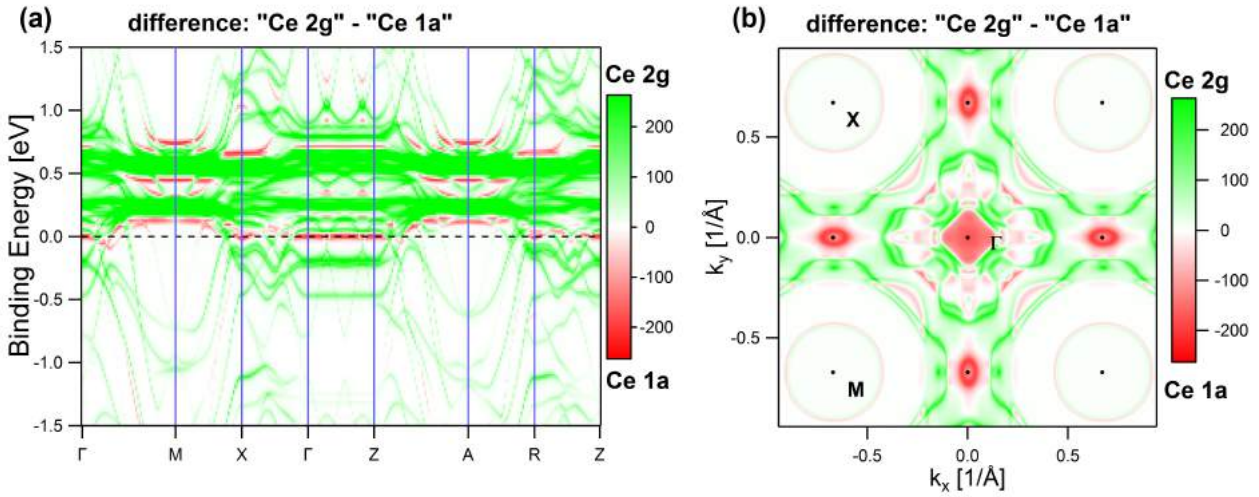

Figure 9.7: (Color on-line) The difference of the BSF coming from Ce 2g and Ce 1g spectral function obtained form KKR calculations visualized along high symmetry direction in k-space (a) and on the Fermi surface (b).

Appendix

List of published articles coauthored by the author of the thesis

1. ***Evidence of momentum-dependent hybridization in $Ce_2Co_{0.8}Si_{3.2}$***

   P. Starowicz, R. Kurleto, J. Goraus, H. Schwab, M. Szlawska, F. Forster, A. Szytuła, I. Vobornik, D. Kaczorowski, and F. Reinert, Physical Review B **89**, 115122 (2015). doi: 10.1103/PhysRevB.89.115122

2. ***Valence Band of $Ce_2Co_{0.8}Si_{3.2}$ and Ce_2RhSi_3 Studied by Resonant Photoemission Spectroscopy and FPLO Calculations***

   P. Starowicz, R. Kurleto, J. Goraus, Ł. Walczak, B. Penc, J. Adell, M. Szlawska, D. Kaczorowski, and A. Szytuła, Acta Physica Polonica A **126**, A144-A147 (2014).

3. ***Electronic structure and transport properties of $CeNi_9In_2$***

   R. Kurleto, P. Starowicz, J. Goraus, S. Baran, Yu. Tyvanchuk, Ya. M. Kalychak, and A. Szytuła, Solid State Communications **206**, 46-50 (2015). doi: 10.1016/j.ssc.2015.01.014

4. ***Electronic Structure of TmPdIn***

   B. Penc, R. Kurleto, J. Goraus, P. Starowicz, and A. Szytuła, Acta Physica Polonica A **129**, 1184-1186 (2016). doi: 10.12693/APhysPolA.129.1184

5. ***Kondo lattice behavior observed in the $CeCu_9In_2$ compound***

   R. Kurleto, A. Szytuła, J. Goraus, S. Baran, Yu. Tyvanchuk, Ya. M. Kalychak, and P. Starowicz, Journal of Alloys and Compounds **803**, 576-584 (2019). doi: 10.1016/j.jallcom.2019.06.140

6. ***Studies of Electronic Structure across a Quantum Phase Transition in $CeRhSb_{1-x}Sn_x$***

   R. Kurleto, J. Goraus, M. Rosmus, A. Ślebarski, and P. Starowicz, The European Physical Jour-

nal B **92**, 192 (2019). doi: 10.1140/epjb/e2019-100157-3

7. ***Effect of electron doping in $FeTe_{1-y}Se_y$ realized by Co and Ni substitution***

   M. Rosmus, R. Kurleto, D. J. Gawryluk, J. Goraus, M. Z. Cieplak, and P. Starowicz, Superconductor Science and Technology **32**, 105009 (2019). doi: 10.1088/1361-6668/ab324f

Contents

I Introduction **9**

1 Ce 4f electrons **11**

2 Kondo effect and heavy fermion physics **15**

3 Cerium intermetallics **21**
3.1 Metallic Ce - phase diagram 21
3.2 RT_9In_2 compounds 22
3.3 CeTX compounds 23
3.4 $Ce_nT_mIn_{3n+2m}$ family 24

4 Ab initio band structure calculations **29**

II Experimental methods **31**

5 Photoemission Spectroscopy **33**
5.1 Basics of Photoemission Spectroscopy 33
5.2 Analysis of spectral function in photoemission 36
5.3 Resonant photoemission 38
5.4 Photoemission spectroscopy on Ce intermetallics 39
5.5 Matrix elements in ARPES 42
5.6 Experimental setups 44
5.6.1 ARPES setup available in Department of Solid State Physics, Institute of Physics, Jagiellonian University 44
5.6.2 Cassiopee beamline, synchrotron Soleil 45

III Results **49**

6 Kondo Lattice Behavior Observed in $CeCu_9In_2$ Compound **51**

7 Studies of Electronic Structure across a Quantum Phase Transition in $CeRhSb_{1-x}Sn_x$ **63**

8 Direct observation on f-electron hybridization effects in $CeCoIn_5$ **79**
8.1 Introduction 83
8.2 Material and methods 83
8.3 Results and Discussion 84
8.4 Conclusions 91

9 Electronic Structure of the Ce_3PdIn_{11} Heavy Fermion Compound Studied by Means of Angle-resolved Photoelectron Spectroscopy 99
9.1 Introduction 103
9.2 Material and methods 104
9.3 Results and Discussion 104
9.4 Conclusions 109